MASTER OF SCIENCE BY RESEARCH

Experimental study of the flow through a scale model of a particulate filter channel

Djedi, Bassem

Award date:
2018

Awarding institution:
Coventry University

Faculty of Engineering, Environment and Computing

School of Mechanical, Aerospace and Automotive Engineering

MScR Thesis

Experimental study of the flow through a scale model of a particulate filter channel

FLUID MECHANICS

Author(s)

Bassem Djedi

Supervisory Team

Dr. Humberto Medina

Dr. Svetlana Aleksandrova

Prof. Stephen Benjamin

March 5, 2018

Certificate of Ethical Approval

Applicant:

Bassam Djedi

Project Title:

Experimental investigation of the flow through catalyst converters: Internal automotive single channel monolith flow \& the effect of porosities on the flow field

This is to certify that the above named applicant has completed the Coventry University Ethical Approval process and their project has been confirmed and approved as Low Risk

Date of approval:

31 March 2017

Project Reference Number:

P52845

Experimental study of the flow through a scale model of a particulate filter channel

Bassem Djedi

This thesis becomes a reality with the kind support and help of many individuals. I would like to extend my sincere thanks to all of them.

Foremost, I want to offer this endeavour to God Almighty for the strength he bestowed on me, the patience, peace of my mind and good health in order to finish this research.

I would like to express my gratitude towards my family for the encouragement which helped me in completion of this work.

I am highly indebted to the supervisory team. I would like to express my special gratitude and thanks to my supervisors, Dr. Humberto Medina, Dr. Svetlana Aleksandrova and Prof. Stephen Benjamin for imparting their knowledge and expertise in this study.

My thanks and appreciations also go to my colleagues, Mr. Jonathan Saul, Mr. Ijhar Rusli and Mr. Abhinivesh Beechook who have willingly helped me out with their abilities.

Faculty of Engineering, Environment & Computing
School of Mechanical, Aerospace & Automotive Engineering
Centre for Mobility and Transport
Coventry University
Priory Street
Coventry CV1 5FB

United Kingdom

This document was typeset using LaTeX

Coventry University
United Kingdom, 2018

Abstract

English version

The aim of this research project model, is to gain a better understanding of the flow characteristics within automotive particulate filters, as the behaviour of the flow within the automotive particulate filter is not well understood. There is no sufficient experimental data regarding the characteristics of the flow within an individual channel of the particulate filter, therefore as a part of this project an experimental program is developed to scale up a typical filter channel to gain a better understanding of the internal flow. The experimental results will help lay a solid foundation for the development of improved macroscopic models. The pressure behaviour changes from one porous wall to another (15%, 20%, and 37%), this was expected. Also, it was noticed that the relation between porosity and pressure drop is inversely proportional, the higher the porosity (37%), the lower the pressure drop, and the flow closely approaching a system with no wall. However, when the porosity is low (15%, and 20%), the dynamic pressure has smaller influence on the wall flow, as it is a smaller fraction of the total pressure drop, and hence the flow is less biased towards the end of the channel. It was found that with porous wall of (15%), the pressure drop increased by almost 20% of that with the porous wall of 20%, and approximately, 40% of that with the porous wall of 37%. Furthermore, multiple jets were recorded close to the porous wall, and the velocity profiles across the porous plate, develops from $20D_p$-$30D_p$, which was expected from a free jet flow. The average Reynolds number throughout the porous plate of 15% was approximately 1.5 greater than the average Reynolds number with 20% porous plate at maximum flow rate used. Also, the average Reynolds number throughout the porous plate of 20% was approximately 1.05 greater than the average Reynolds number with 37% porous plate at maximum flow rate used. It was also noted down, that with the lowest mass flow rate, the average Reynolds number throughout the porous plate of 15%, was approximately 1.3 greater than the average Reynolds number with porous plate of 20%. At last, the average Reynolds number throughout the porous wall of 20%, was 1.2 greater than the average Reynolds number with 37% porous wall.

Version française

L'objectif de cette recherche est de mieux comprendre les caractéristiques flux d'air dans un filtre á particules automobile, car le comportement du flux dans le filtre á particules automobile n'est pas bien compris. Il n'y a pas de données expérimentales suffisantes concernant les caractéristiques du flux dans un canal individuel du filtre á particules, donc, dans le cadre de ce projet, un programme expérimental est développé pour étendre une géométrie typique des canaux de filtrage afin de mieux comprendre le flux interne . Il a déjá été démontré qu'il est possible de simuler le flux dans le filtre á particules. L'approche expérimentale aidera á établir une base solide pour le développement de modéles macroscopiques. Le comportement de la pression change d'un mur poreux á l'autre (15%, 20%, and 37%), ce qui était attendu. En outre, il a été remarqué que la relation entre la porosité et la chute de pression est inversement proportionnelle, plus la porosité est élevée (37%), plus la chute de pression est faible et le flux approchant un systéme sans paroi. On a constaté qu'avec une paroi poreuse de (15 %), la perte de charge augmentait de prés de 20% de celle de la paroi poreuse de 20% et environ 40% de celle de la paroi poreuse. de 37 %. De plus, plusieurs jets ont été enregistrés á proximité de la paroi poreuse, et les profils de vitesse á travers la plaque poreuse, se développent á partir de $20D_p$-$30D_p$, ce qui était attendu d'un jet libre. Le nombre moyen de Reynolds dans toute la plaque poreuse de 15% était supérieur d'environ 1.5 au nombre moyen de Reynolds avec une plaque poreuse de 20% au débit maximum utilisé. De plus, le nombre moyen de Reynolds dans toute la plaque poreuse de 20% était supérieur d'environ 1.05 au nombre moyen de Reynolds avec une plaque poreuse de 37% au débit maximal utilisé. Il a également été noté qu'avec le débit massique le plus bas, le nombre moyen de Reynolds dans toute la plaque poreuse de 15% était supérieur d'environ 1.3 au nombre moyen de Reynolds avec une plaque poreuse de 20%. Enfin, le nombre moyen de Reynolds dans toute la paroi poreuse de 20 % était supérieur de 1.2 au nombre moyen de Reynolds avec un mur poreux de 37%

Contents

List of Figures

List of Tables

Nomenclature

Roman Symbols

ΔP	Pressure Drop	(Pa)
c	Contraction ratio	
H/D	Height to nozzle diameter ratio	
H_{in}	Contraction inlet	(m)
H_{out}	Contraction outlet	(m)
L_c	Channel length	(m)
L_p	Porous plate length	(m)
$m_{f\ out}$	Mass flow rate exiting the nozzle	(kg/s)
m_f	Mass flow rate entering the nozzle	(kg/s)
Q	Volume flow rate	(m^3/s)
Re	Reynolds Number	
Re_b	Bulk or mean Reynolds Number	
Tu	Turbulent intensity	(%)
U_b	Bulk or mean Velocity	(m/s)
U_p	Porous wall velocity	(m/s)
U_w	Slip velocity	(m/s)
U_c	Centre line velocity	(m/s)
U_{rms}	Root mean squared velocity velocity	(m/s)
U_t	Time averaged velocity	(m/s)

V_{pores}	Pores volume	(m^3)
V_{tot}	Total volume	(m^3)

Greek Symbols

α	Factor of vicous drag portion of pressure drop	
β	Factor for the form of the drag portion	
ϵ_p	Porosity level	(%)
ϵ_w	wall roughness	(m)
τ_w	wall shear stress	(kg/ms^2)

Subscripts

e	Enterance
h	Hydraulic
p	Porosity
w	Wall

Acronyms

CFD	Computational Fluid Dynamics
DNS	Direct Numerical Simulation
DPF	Diesel Particulate Filter
HWA	Hot Wire Anemometer
LDA	Laser Doppler Anemometer
PIV	Paticle Image Velocimetry

Chapter 1

Introduction

There is a large number of cars on the roads and each one is a source of air pollution. Therefore, improving the efficiency of car engines is important to help reducing their harmful emissions, caused by their incomplete combustion. One of the devices utilized by car manufactures in order to reduce the harmful emissions of pollutants is the particulate filter.

Diesel particulate filters, appear to be the most reliable devices to reduce particulate emissions in Diesel engines. An automotive particulate filter system (shown in Figure 1.1) is characterized by series of parallel channels (Figure 1.2) of typically $1mm\,x\,1mm$ size, [26, 27]. The channels are alternatively plugged, this way the flow is forced to flow through the porous walls, where the particles are trapped. The filters usually remove 85% [28] or more of the pollutants. Some filters are single-use, they are intended to be replaced once the filters are clogged. Other designs can be used over time, by means of regeneration process, meaning that at certain temperature the accumulated soot can be burnt off through the use of a catalyst or by active means such as fuel burner. The device became popular up to just ten years ago [29], and is fairly a new technology. The reasons behind its delayed introduction in the field is due to several interdisciplinary aspects. For many years the pollutants have been reduced by improving the injection and the combustion processes [30, 31], flexible turbocharging systems [32], or exhaust gas recirculation control [33]. Such solutions have delayed the introduction of the DPF. However, increasingly restrictive regulations [34], have caused both manufacturers and researchers to resort to DPF systems. Such systems guarantee good filtration of pollutants, which leads to improvements in particulate filtration [35, 36]. The development of DPFs systems, initiated the investigation of different materials and flow path-lines, for example: ceramic fibres, ceramic honeycomb wall-flow monoliths, metal fibre filters or sintered metals. Among these systems, the honeycomb wall-flow monoliths

are used most frequently in the industry. Such filters are characterised by small axial parallel channels, of square cross-section, with adjacent channels alternatively plugged at each end, to force the gas exhaust to flow through the porous medium, as explained earlier, and this will be the focus of the present work.

Figure 1.1: DPF system

Figure 1.2: Filter channels

1.1 Motivation

In order to improve the efficiency of the particulate filter it is important to gain an understanding of the internal flow characteristics, as the flow behaviour within the filter channel is not well understood. There is not sufficient experimental data regarding the characteristics of the flow within an individual channel of a particulate filter, therefore as a part of this research project, an experimental program was performed to scale up a typical filter channel configuration to gain a better understanding of the internal flow. It has already been shown that it is possible to simulate the flow within a typical filter channels structure [25, 37]. The experimental approach will help lay a strong solid foundation for the development of improved macroscopic models, and flow characteristics inside the filter channels. Furthermore, it also provides further assessment of the subsequent effect of low porosity (15%, 20% and 37%) side walls on the flow field, as in the literature such low porosities have not been studied in details unlike the higher porosity percentages (refer to Chapter 2 section 2.4 for more information).

1.2 Aims and objectives

1.2.1 Aim

The aim of the research project is to experimentally investigate the air flow through an individual particulate filter channel and the effect of low porosity side walls on the flow distribution. Individual objectives include:

1.2.2 Objectives

1. To carry out a thorough literature study of relevant fundamental flow structures (pipe/duct, free jet, and porous medium flow).
2. To develop a test facility to investigate the flow field within a scaled up particulate filter channel and to devise a suitable experimental programme (experimental instrumentation include Hot-Wire Anemometry and pressure scanners (Scanivalves)). The test rig being a scaled-up representation of the flow through a general particulate filter channel.
3. To carry out a series of initial tests, to characterise and validate the test rig and to ensure flow uniformity at the entrance of the test section.
4. To characterise the porous walls by carrying out pressure measurements along the channel length, overall local pressure drop and velocity profiles at the porous wall exit.
5. Analyse and evaluate results and draw conclusions on the effect of porosities on the pres-

sure distribution along the channel and exiting velocity profiles.

Chapter 2

Literature review and background

2.1 Introduction

In order to understand what is really happening in the particulate filter, it is imperative to investigate the types of flow occurring in such system, as it is a quite complex system. This chapter will help in clarifying the types of flow existing in a particulate filter. A simple schematic shown below (Figure 2.1), illustrates the flow occurring pattern in a filter.

Figure 2.1: Schematic of the particulate filter operational system (red lines are the plugged channels)

2.2 Flow in an automotive particulate filter

In some ways, the flow entering the particulate filter resembles a free jet flow impinging a surface (refer to Figure 2.1). As the upstream exhaust gases impinge on the automotive particulate filter, the flow through the particulate filter exhibits a pressure drop (ΔP). Impinging jets display different types of flow features such as, free jet/potential flow, turbulence, vortices, shear and wall-bounded shear layers, and stagnation regions [38, 39]. As a result, impinging jet characteristics have attracted huge interest for fundamental research into fluid mechanics. Impinging jets are very important in many applications, such as cooling of inner surface of turbine blades and electronics, annealing of metal sheets, and drying textile, etc. The flow emerging from the nozzle develops into a parabolic velocity profile (either laminar or turbulent depending on the Reynolds number). Now depending on how far the impinging surface (which is in this case the particulate filter) is located, the flow behaves as a free jet to a certain limit, this limit depends on the H/D ratio (H is the distance of the particulate filter from the nozzle, and D is the nozzle diameter). The velocity gradients of the jet flow create a shearing at the edges of the jet flow stream, therefore the momentum is transferred laterally outward, collecting extra fluid along with the jet flow, and thereby increasing the net mass flow. Once the exhaust gases reach the particulate filter, the flow stagnates resulting in the increase of the local pressure, therefore forcing the flow radially outwards along the surface, which results in boundary layer development. Furthermore, after the exhaust gases have impinged on the surface (inlet of the particulate filter), it continues on throughout the axial parallel channels, where the flow resembles that of a duct flow (refer to Figure 2.1 in function of filter element). Lastly, when the flow impinges on at the end of the inlet channel, it is forced through the porous walls, and hence the flow behaviour here resembles a porous medium flow. In a general DPF system, there are large losses caused by the contraction and expansion of the system (can be seen in Figure 2.1). It should be noted that since the simplified approach will only consider a single channel with porous side walls, the contraction and expansion losses are not considered here (refer to Appendix B in 6.6 for more information).

2.3 Duct/pipe flow

As already discussed in section 2.1 the flow into a particulate filter, resembles the type of flow in a pipe and duct, as the flow is constrained by walls. Therefore it is a better approach to build up knowledge around pipe and duct flow characteristics and fundamentals. Pipe and duct flows are strictly a type of an internal flow, i.e., "bounded by walls". Frank et al. [9] highlights that an internal flow is constrained by walls, and the viscous effects start to grow and diffuse throughout the entire flow (An illustration of a duct flow propagation, is shown in Figure 6.23, in Appendix E section 6.5).

Many turbulent flows in practice happen in ducts of non-circular cross-section; for example, heat exchangers, air-conditioning systems, and rotary machinery. Melling et al. [40] provided a detailed experimental study using the Laser Doppler Anemometer, on developing turbulent flow in a non-circular cross-section duct (rectangular duct), at Re = 42000. The purpose of the work was to provide a data for other scholars to use in developing and testing of turbulence models, and to asses the functionality of the Laser-Doppler Anemometer compared to other measurement tools such as the Hot wire Anemometer. The duct was a $9mm$ thick perspex, and the working fluid was water. Results show that the axial growth of the mean-velocity was more gradual initially compared to previous study by Ahmed et al. [41]. However, Ahmed et al. [41] results were less reliable because of the degree of symmetry in their flow was poor compared to Melling et al. [40], which was due to the inlet conditions as it was not a plug flow.

Furthermore, it has been shown that the Laser Doppler Anemometer has the potential advantage over the Hot wire Anemometer in measuring the secondary velocity components, as there is no probe interference in the flow. However, due to the sensitivity of the measurements to the angle of interference fringes, and the large magnitude of the axial velocity relative to the secondary velocity, the secondary flow results did not satisfy the continuity law.

It is rather important to also consider cases with lower Reynolds number to gain further insight into the flow behaviour in a duct/pipe. Eggels et al. [2] carried out experimental and numerical study (Direct numerical simulation (DNS)) on the fully developed pipe flow (See Appendix E 6.5, for motion equations and geometrical differences between different cross-sections) at a R eynolds number $Re \approx 7000$. The flow results were obtained from two different numerical codes and three separate measurement techniques; namely the Hot Wire Anemometer(HWA), Laser Doppler Anemometer (LDA), Particle Image Velocimetry (PIV). Both the numerical and experimental results are compared together resulting in a good agreement. Then the results are compared against the numerical results obtained by Kim et al. [1] (referred by the author as KMM).

As outlined by the author the numerical and experimental results shown in Figure 2.2 have a reasonable agreement. Furthermore, the values of C_f computed from both DNS(E) and DNS(U) data ($9.22x10^{-}3$ and $9.21x10^{-}3$ respectively) are in excellent agreement with the Blasius' value of $9.26x10^{-}3$ at Re = 5300. It is interesting to note that the parameters above agree well with the DNS results of the flow through a square duct, obtained from another scholar, Gavrilakis [42] ($\frac{U_c}{U_b}$ = 1.32, $\frac{U_b}{u_\tau}$=14.7, C_f = $9.26x10^{-}3$, where U_c is the centreline velocity, U_b is the mean or bulk velocity, u_r is the wall shear stress velocity, and C_f is the friction coefficient). However, since it is a square duct, then the flow is homogeneous in the streamwise direction only, and that is due to the presence of the secondary flow regime (as discussed in details by Melling et al. [40]). In addition , the presence of the side walls on the square duct ([42]) and the pipe ([2]) results in different mean flow properties from the plane channel flow ([1]), due to the additional wall friction.

	DNS(E)	DNS(U)	PIV	LDA	HWA	KMM
$Re_c = U_c D/\nu$	6950	6950	7100	7200	7350	6600
$Re_b = U_b D/\nu$	5300	5300	5450	5450	5600	5600
$Re_\tau = u_\tau D/\nu$	360	360	366	371	379	360
U_c/u_τ	19.31	19.29	19.38	19.39	19.40	18.20
U_b/u_τ	14.73	14.74	14.88	14.68	14.76	15.63
U_c/U_b	1.31	1.31	1.30	1.32	1.31	1.16
$C_f = \tau_w/\frac{1}{2}\rho U_b^2$	9.22×10^{-3}	9.21×10^{-3}	9.03×10^{-3}	9.28×10^{-3}	9.18×10^{-3}	8.18×10^{-3}
δ^*/R	0.127	0.126	0.124	0.130	0.128	0.141
θ^*/R	0.068	0.068	0.068	0.071	0.070	0.087
$H = \delta^*/\theta^*$	1.86	1.85	1.83	1.83	1.82	1.62
G	8.91	8.85	8.78	8.79	8.73	6.97

Figure 2.2: Flow properties obtained from numerical simulations and experiments. The results obtained from Kim et al. [1] are referred to as (KMM). The compared parameters given by Eggels et al. [2] are: U_c is the centreline velocity, U_b is the mean or bulk velocity, u_r is the wall shear stress velocity, D is the pipe diameter or full channel width, ν is the kinematic viscosity, τ_w is the wall shear stress, C_f is the friction coefficient, H is the shape factor, δ^* and θ^* are the displacement and momentum thickness respectively, and R the channel half width or pipe radius. [2]

(a) Experimental and numerical results of the Axial mean velocity profile. [2]

(b) Mean velocity variations.

Figure 2.3: Axial mean velocity profiles experimental and numerical data. **a**; Axial mean velocity profiles. **b**; magnified into Figure **a**, where the residuals are plotted with respect to DNS(E) data. The error bars indicate the 95% reliability. Legend is similar to Figure (**a**).

Further remarkable findings are that the mean velocity profile results from the numerical studies (DNS(E) and DNS(U)) are in an excellent agreement with the experimental results obtained by

LDA, HWA, and PIV measurments (Shown in Figure 2.3a). The profiles coincide for all $\frac{r}{D}$. It is noted by the Eggels et al. [2] that the DNS(U) profile in Figure 2.3a is not visible because it collapses onto the DNS(E) profile. Eggels et al. [2] magnify Figure 2.3a to show the difference between the numerical and experimental solutions. Eggels et al. [2] further sheds important remarks: one is that the deviations in the mean velocity profiles between the experimental and numerical pipe flow data are much smaller than $0.5u_\tau$ (u_r is the wall shear stress velocity), which confirms the difference between the pipe and plane channel flow. In addition, the ratio of $\frac{U_b}{u_\tau}$ in the plane channel geometry is about 6% larger than the pipe flow case, however the ratio $\frac{U_c}{U_b}$ is 12% smaller(These changes as already mentioned are due to the presence of the additional wall friction). Whereas in the case of square duct compared with the pipe configuration, the ratios mentioned above are much smaller (the deviations are $\approx$ 0.5% and $\approx$ 1.5% respectively), which will be expected in this work as the channel is a square section. Also, it can be concluded that the PIV, LDA and HWA measurements of the velocities are within the range from each other (PIV ($\frac{U_c}{U_b}$=1.30), LDA ($\frac{U_c}{U_b}$=1.32), HWA ($\frac{U_c}{U_b}$=1.31), refer to Figure 2.2 for more information), therefore the HWA is a suitable technique of the flow investigation, which will be used for the velocity measurements in this work.

2.4 Porous medium/capillary flow

Air flow through porous media is universal in a broad range of industrial equipment, e.g., filters, heat exchanges, catalytic reactors and pneumatic silencers. A number of studies [43–46], have characterized the physics of the flow through porous medium under two main assumptions: that the internal structure of the porous medium is isotropic and homogeneous. The results show that the linear Darcy regime [43] can properly predict the flow behaviour when the fluid velocity is sufficiently small, or when the case is subjugated by viscous effects. On the other hand, when inertial effects become dominant, the pressure gradient against flow velocity exhibit a non-linear relation. On this occasion, the two most well known equations that include the effects of viscosity and inertia are the Ergun equation (Equation 2.1) and Forchheimer equation (Equation 2.2) [47, 48].

$$\rho\frac{\Delta P}{L} = \frac{\alpha(1-\epsilon_p)^2\mu}{\epsilon_p^3 A\varphi^2 D_{cell}^2}G + \frac{\beta(1-\epsilon_p)}{\epsilon_p^3\varphi D_{cell}A^2}G^2 \tag{2.1}$$

$$\Delta P_p = \frac{\mu}{k}V_p w_p + \beta_F \rho V_p^2 w_p \tag{2.2}$$

The nomenclature of equations 2.1 and 2.2 can be found in Appendix F 6.6.

Many scholars have endeavoured to correlate experimental data to assess the flow characteristics of porous media using the two fundamental equations. Contributions of early experimental tests done by Beavers et al. [49, 50] point out that the flow characteristics of fibrous porous media can be described by Forchheimer equation with suitable permeability and inertial coefficient. Antohe et al. [51] presented a study on which they used Forchheimer extended flow model to compute the permeability and inertial coefficient in the compressed aluminium matrices. Furthermore, Dukhan et al. [52] proposed to use two permeabilities, one for the Darcy regime and another for the Forchheimer regime, to interpret pressure drop properties. Also, Dukhan and Patel [53, 54], Dukhan and Ali [55] have investigated wall, size, entrance and exit effects on the form drag coefficient and permeability. Dukhan [56] further experimentally investigated the use of Forchheimer equation, and verified the validity of Ergun-type relationship, to characterize pressure drop with respect to flow field velocity and confirmed that the inertial coefficient and permeability both correlate well with porosity. Du Plessis [57] theoretically derived a momentum transport equation based on Ergun equation for the fully developed flow through porous medium. According to literature examination, it seems that porous medium of high porosity percentages ($>$ 80%) have been frequently used in earlier applications. Also present references for which they use either the Forchheimer ([11–16]) or Ergun ([58,59]) equation commonly neglect the effect of velocity gradient in the flow direction. Most of these studies assume that, when the unidirectional airflow passes through the porous media, air compressibility is negligible, due to slight pressure drop, and therefore the velocity direction is in general, considered constant [60–62]. Zhong *et al.* [63], experimentally investigated a modified Ergun equation that includes compressibility effects and to describe friction characteristics, however this won't be discussed more, as the flow in the present work will be considered incompressible.

Suga et al. [3] performed an experimental study on the effects of wall permeability on turbulence close to a porous wall. The flow properties were measured using particle image velocimetry (PIV) system. The porous media utilized were three kinds of foamed ceramic (non-homogeneous pore structure), of the same porosity (80%), but different permeabilities. The Reynolds number range covered the laminar and turbulent flow regimes (Re = 1000 $-$ 10, 000). The working fluid was chosen to be water. Figures 2.5 and 2.4, shows the three foamed ceramic mediums used (Cases 20 (**a**), 13 (**b**), 06 (**c**)) and test rig configuration, respectively.

Figure 2.4: Suga et al. [3] test rig configuration

Figure 2.5: Porous media of different permeabilities. (**(a)**, **(b)**, and **(c)** ceramic foams structures with permeabilities of $0.020 mm^2$, $0.033 mm^2$, and $0.087 mm^2$ respectively) [3]

The experimental results obtained by Suga et al. [3] clearly coincide with the direct numerical simulation (DNS) performed by Breugem et al. [4]. Breugem et al. [4] reported that the weakening of the wall-blocking effect (due to wall permeability) tends to increase the wall normal fluctuations. Furthermore, Breugem et al. [4] points out that even in a fully turbulent mean flow regime, the flow inside the porous wall is principally laminar, due to the porous medium resisting the flow and hence bringing down the velocity, which will be expected in the present work. Also, the porous wall structure affects the laminar to turbulent flow transition and similarly affects the friction coefficient. Results show that the friction coefficient is higher than that of the solid wall with 95% porosity, by a

factor of up to 3, effects can be seen in Figures 2.6 and 2.7. A few studies ([3–5,11,13,14,23,24]) have used low percentages of porosities, as ranges of 35%-90% have been frequently used in many investigations and applications.

Case	ϵ_c	Re_τ^p	Re_K	Re_d	δ_w/H	Re_δ^p	Re_δ^t	$C_f^t(\times 10^{-3})$	$C_f^p(\times 10^{-3})$
E95	0.95	678	9.35	6.78	0.74	498	108	10.9	30.4
E80	0.8	398	1.06	3.98	0.56	222	156	8.3	10.5
E60	0.6	353	0.31	3.53	0.50	176	175	8.1	8.2
E0	0	352	0	0	0.50	176	175	8.1	8.2

Figure 2.6: Coefficient of frictions, subscripts "t" and "p" are the top and permeable wall region [4]

Figure 2.7: Mean velocity profiles for different porosity cases; "$- - -$" case $E95$ (95%), "$-.-$" case $E80$ (80%),"$***$" case $E60$ (60%), "—" case$E0$ (0%). [4]

2.5 Summary

Following the background research, the following points have been identified:

1. Pressure losses due to contraction and expansion are considered in many investigations in a particulate filter system, which is due to the configuration of having two channels (can be seen in Figure 3.1). [5, 11–16]. However in the present work, the configuration is simplified by having a single channel blocked at its end, therefore these losses (contraction and expansion) are not considered.

2. How Wire Anemometer (HWA) technique will be used in the present work, for velocity measurements. The study by Eggels et al. [2] comparing different techniques LDA and PIV with the HWA, validates using HWA for the present flow measurements (the comparison can be seen in Figure2.2).

3. Many scholars have investigated high porosities, ranging from 35% to 90% ([3–5, 11, 13, 14, 23, 24]). To complement these studies, lower porosities of 15%,20% and 37% will be the focus of this work.

4. To the authors knowledge, no studies have been carried out to study the pressure distribution along the channel, with different porous side walls installed. Therefore, this study will provide experimental data to fill this gap.

5. Even if the flow is turbulent in the channel, the flow regime inside the porous wall is laminar, due to resistive property of the porous medium [4]. However, to the authors knowledge, there was no encounter regarding a study of the velocity profiles exiting the porous walls of a particulate filter. Therefore, this experimental program will also focus on the exiting profiles.

Chapter 3

Experimental methodology

3.1 Introduction

The motivation of this work (as discussed in section 1.1), is to gain an understanding of the flow characteristics within a particulate filter channel, as the behaviour of the flow inside the channel filter is not well understood. So far after searching through the literature available (see Chapter 2), to the authors knowledge there was no encounter of an attempt to scale up a single filter channel and investigate what is really happening inside that single channel.

The flow through an automotive particulate filter is very dependent on the structure of the filter, such structural characteristics are the porosity, wall thicknesses, filter lengths, and cell sizes. The operating conditions in the filter differs as well, from the typical flow rates, Reynolds numbers in the channels and pores. Based on the literature, these values are outlined as ranges in Table 3.1. In addition, it seems that porous media (filters) of high porosity percentages (35%-90%) have been frequently used in earlier applications, therefore this project will concentrate on lower range of percentages (15%,20% and 37%). In this chapter, the rigs design requirements and manufacturing procedure will be explained.

Porosity range (%)	35-90
Cell size range (mm)	1.2x1.2-3.5x3.5
Wall thickness range (mm)	0.36-1.5
Pore size range (μm)	10-40
Filter length range (mm)	58-200
Flow rate range (g/s)	20-600
Reynolds numbers range in channel	120-80, 000
Reynolds numbers range in pores	0.4-2

Table 3.1: Typical structural characteristics of a Particulate filter, and working conditions [13,16–25]

The figure below shows a typical particulate filter configuration;

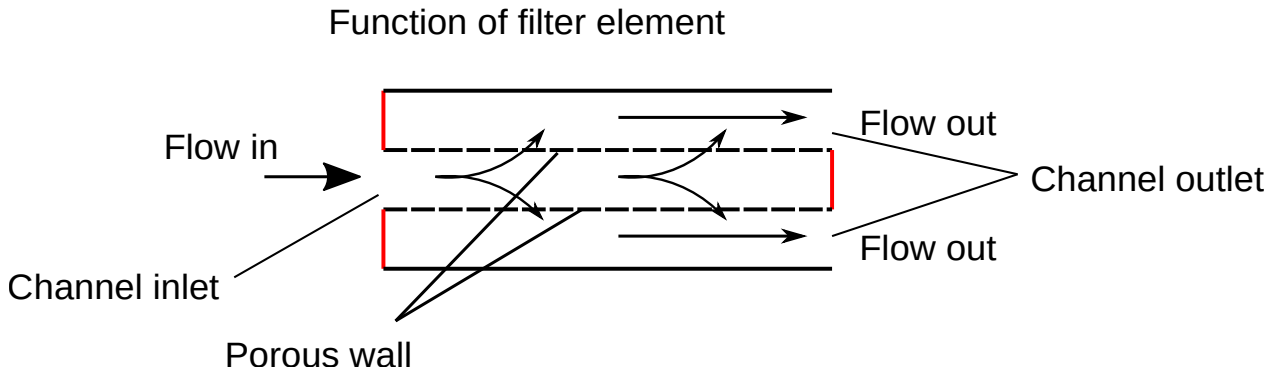

Figure 3.1: Schematic of a typical wall filter flow system (red lines are the plugged channels)[5]

Characteristics	Typical particulate filter	Present scaled up filter set up
Porosity	35-90 (%)	15, 20, 37 (%)
Filter length	58-200 (mm)	270 (mm)
Pore size	10-40 (μm)	2 mm
Wall thickness	0.36-1.5 (mm)	5 (mm)
Channel size	1.49x1.49-3.5x3.5 (mm)	62 (mm)
Pore Reynolds numbers	0.4-2	132-556
Channel Reynolds numbers	120-80, 000	9, 404-50, 000

Table 3.2: Comparison between the present scaled up filter with typical particulate filter

It can be seen from the table 3.2 , that the present experimental set up moved away from similarity of a typical particulate filter. Major differences correspond to the porosity values and pore sizes. The reason, for the values of the porosity chosen, was to gain an understanding of how low porosities affect the flow field in a filter channel. Also, another porosity (37%) was chosen, which is close to a typical particulate filter porosity for future comparison with another experimental program. Furthermore, the pore sizes were different from the typical pore size filter, due to the available manufacturing capabilities and time constraints. The 3-D printer capabilities could not manufacture size lower than 1.5 *mm*. Table 3.2 also shows that the Reynolds numbers in the

pores are larger than the typical values, however the Reynolds numbers in the channel are within the typical range.

The test matrix of the experimental program is shown below, in Table 3.3:

Velocity Measurements	Pressure Measurements
Nozzle exit profile to check velocity linearity. Velocity exit profiles along the porous medium.	Pressure drops across the three porous walls. Local pressure drops along the test section.

Table 3.3: Test Matrix

3.2 Rig design and requirements

The following section will discus the design requirements of the test rig. The upstream section of the channel filter was manufactured using the Ultimaker 3 extended 3-D printer. The test section is comprised of two aluminium plates and the porous walls. The instrumentations used were the How Wire Anemometer (HWA) and pressure scanners (Scanivalve), to measure velocity and pressure values respectively. The measurements processes are explained in details. The rig will be validated by checking its physical features, which is explained more in section 3.5.1.2. The test rigs schematic is shown in Figure 3.2.

3.2.1 Scale up approach

As a first step to design the rig, it is imperative to use a typical particulate filter channel to scale up and have an overview of what dimensions the rig should have. An important physical range while scaling up would be the Reynolds number ($Re = \frac{VH}{\nu}$), as it takes into consideration the fluid velocity(V), length scale or the channel height (H), and the kinematic viscosity (ν).

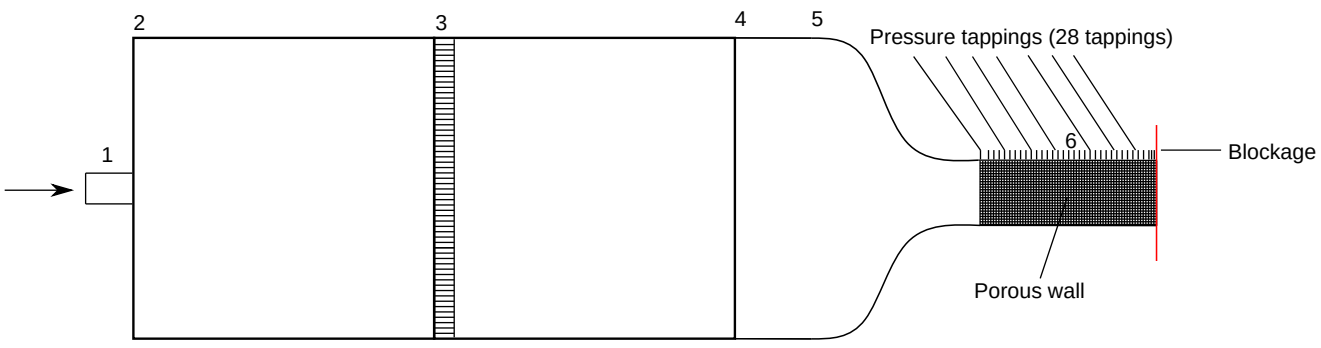

Figure 3.2: Experimental rig schematic

The experimental program will simplify the set up shown in Figure 3.1, by having a single axisymmetric channel, with porous walls on both sides, can be seen in Figure 3.2 .

The operational Reynolds numbers in previous experiment and numerical studies are shown in Table 3.4. So having a channel of 62 *mm* height (considering space limitations) as the largest possible size to cover the Reynolds numbers operated in the previous experimental and numerical studies would be suitable. The Reynolds number is ranging from $9,404$ to $50,000$, and can be more. The ranges of Reynolds numbers are advantageous for other scholars to compare their data, and would be able to provide further understanding of the flow physics.

Early studies	**Reynolds numbers**
Haralampous et al. [24]	$10,000 - 40,0006$
Skaperdas et al. [16]	$35,000$
Payri et al. [23]	$30,000 - 150,000$
Benjamin et al. [25]	$57,609$

Table 3.4: Some early studies relating to particulate filter investigation

3.2.2 Contraction nozzle

As discussed in Chapter 1, the flow in a particulate filter, resembles a free jet flow. The contraction nozzle (5, shown in the schematic, Figure 3.2) provides such type of flow and also with the right design will reduce the risk of any flow separation (will be discussed more in this chapter).

The contraction nozzle is an integral part of the rig. During the late 1970*s*, Mehta et al. [6] performed experiments on flow through individual components of the wind tunnel, which lead to an increase understanding of the design philosophy. The design of the contraction nozzle in this work will follow the philosophy implemented by Mehta et al. [6].

It is rather critical when designing such component, for two main reasons. Firstly, a contraction increases the flow mean velocity and this allows the honeycomb to be placed in a lower speed region, to reduce any pressure loss and clean the flow by reducing turbulence. Secondly, since the total pressure is constant through the contraction, thereby the mean and fluctuating velocity variations are reduced. The most important single parameter which can effect the physical performance of such component would be the contraction ratio, *c*. The ratios between 6 and 10 are found to be suitable for most small, low-speed contraction nozzles.

Apart from contraction ratio, another parameter is also considered critical, which is the cross-sectional shape. The corner flow in the contraction, generally tends to separate due to very low velocities. Therefore a circular cross-section is ideal. Early investigation have shown that even for square or rectangular cross-sections, in the absence of separation, the corner flow physical

features are localized, as in that they do not affect the test wall flow significantly. In the present case, the filter channel is rectangular, therefore as a compromise a contraction nozzle with an octagonal cross-section was considered the best approach for this research.

Another desirable flow quality is to have a minimum boundary layer thickness at the contraction exit, here the contraction nozzle length plays a roll in reducing the boundary thickness. Of course shorter contractions are desirable as space and cost can be minimal, however this would risk the boundary separation. Boundary layer separation results in an exit flow that is non-uniform and unsteady.

Mehta et al. [6, 7] method uses an iterative design procedure to develop 2-D and 3-D contraction nozzles. They have performed an analytical and experimental procedures in determining which design is suitable for small, low speed wind tunnels. The computational and experimental results were found to lie within 10%, with the predicted values generally lower. In their investigation, the 5^{th} order polynomial wall shape was found to be performing optimally, in terms of avoiding flow separation and non-uniformity. The contraction ratio of the four wall shapes (3^{rd}, 5^{th}, 7^{th} order polynomials and matched cubics) was 7.7 and all of the same cross-section. The control parameter here would be the contraction length on the boundary layer thickness. Wall Contour shapes (shown in Figure 3.3) are described by the following expressions:

- Third order polynomial:

$$Y(X) = H_{in} - (H_{in} - H_{out})\Big[-2\big(x^{'}\big)^3 + 3\big(x^{'}\big)^2\Big] \tag{3.1}$$

- Fifth order polynomial:

$$Y(X) = H_{in} - (H_{in} - H_{out})\Big[6\big(x^{'}\big)^5 - 15\big(x^{'}\big)^4 + 10\big(x^{'}\big)^3\Big] \tag{3.2}$$

- Seventh order polynomial:

$$Y(X) = H_{in} - (H_{in} - H_{out})\Big[-20\big(x^{'}\big)^7 + 70\big(x^{'}\big)^6 - 84\big(x^{'}\big)^5 + 35\big(x^{'}\big)^4\Big] \tag{3.3}$$

- Matched Cubics:

$$\begin{bmatrix} For\ 0 \leq x^{'} \leq x \\ Y(X) = H_{out} + (H_{in} - H_{out})\Big[1 - \frac{\big(x^{'}\big)^3}{x^2 L_c^3}\Big] \\ For\ x \leq x^{'} \leq 1 \\ Y(X) = H_{out} + (H_{in} - H_{out})\Big[1 - \frac{\big(x^{'}\big)^3}{(1-x)^2}\Big] \end{bmatrix} \tag{3.4}$$

Where $Y(X)$ is the line shape, H_{in} is the nozzle's inlet height, H_{out} is the nozzle's outlet height, $x^{'}$ refers to the discrete points, and L_c is the contraction length.

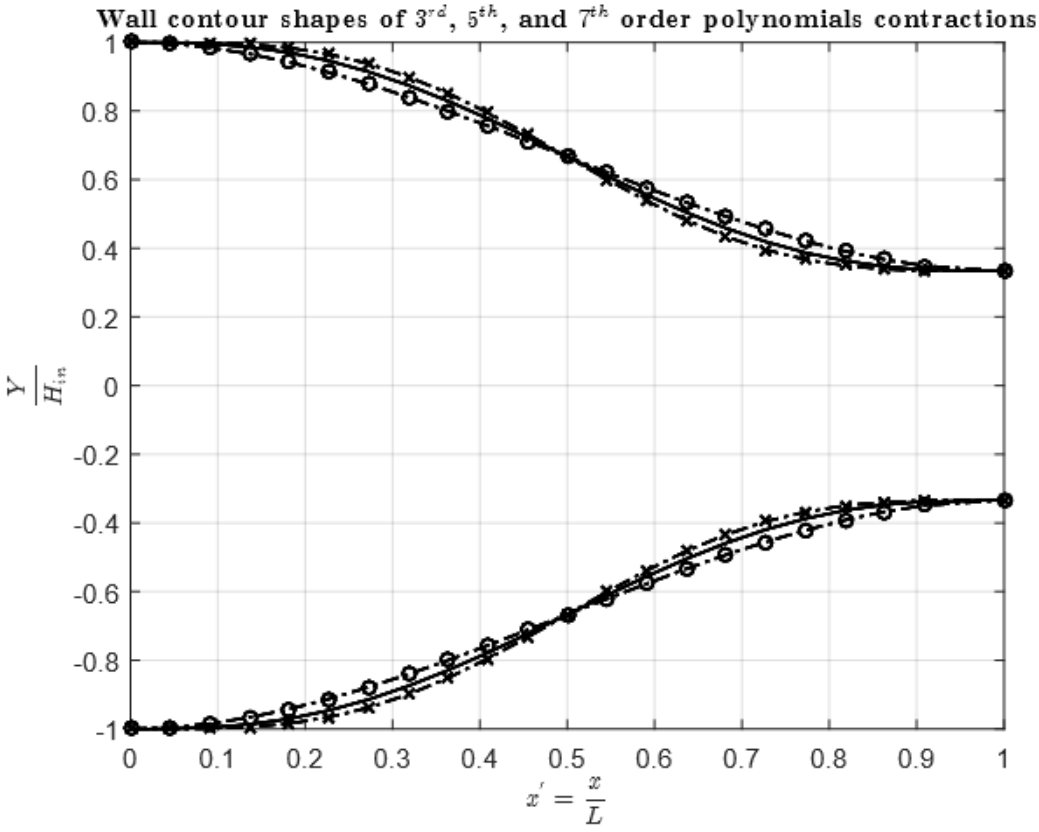

Figure 3.3: Wall contour shapes of the contractions specified by Mehta et al. [6,7]. ("$-.o$"; 3^{rd} Order polynomial. "$-$"; 5^{th} Order polynomial. "$-.x$"; 7^{th} Order polynomial

Results by Mehta et al. [6,7] have shown that the flow uniformity at the contraction exit improves with the increase in the contraction length, but to a certain point. In 5^{th} order contraction, the flow separated near the inlet and exit when $L_{contraction}/H_{in}$ was 0.7 and 1.79 (shown in Figure 3.4), respectively. This is due to the region of adverse pressure gradient near the contraction exit. The higher the contraction length, the thicker the boundary layer is, which makes it more likely to separate near the exit. On the other hand, if the contraction length is very short, the boundary layer separation would tend to be near the inlet. Furthermore, the 7^{th} order and matched cubics shapes had flow separation near the inlet. The flow through the 3^{rd} order design however, showed no flow separation, but more of flow non-uniformity and further no optimization was attempted on this shape. It is clear that the 5^{th} order polynomial shape is a satisfying contraction nozzle, as it was free of flow separation on both the centre line of the nozzle and its corners. Also the flow uniformity had less than 1% variation. The contraction length to inlet height ratio ($L_{contraction}/H_{in}$) was chosen based on Mehta et al. [6,7] results, shown in figure 3.4. As a conclusion, it is agreed that the 5^{th} order polynomial contraction is much suitable compared to other wall contours.

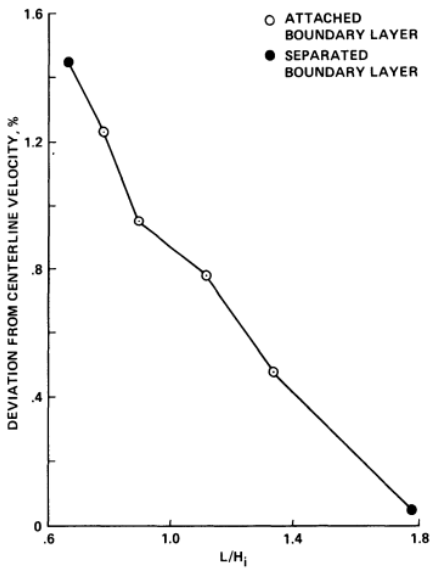

Figure 3.4: Effect of L_c/H_{in} ratio on the flow uniformity [6, 7]

As a part of the design validation, a simulation was performed using SOLIDWORKS simulation package, to investigate which contraction length ratio to choose. The designed nozzle is shown in Appendix A, 6.1 Two different contraction length ratios ($\frac{L_{contraction}}{H_{in}}$) were chosen, 1.45 and 1.75. The flow was pressure driven (nozzle exit boundary condition is set to atmospheric pressure). The inlet velocity was 1 m/s.

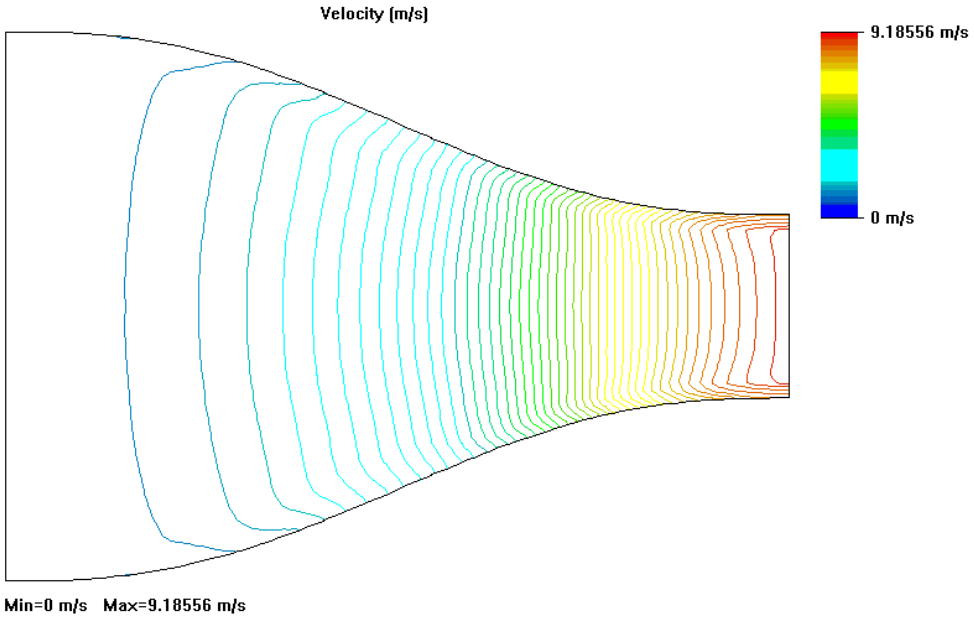

Figure 3.5: $\frac{L_{contraction}}{H_{in}}$=1.45, Side view showing the velocity isolines

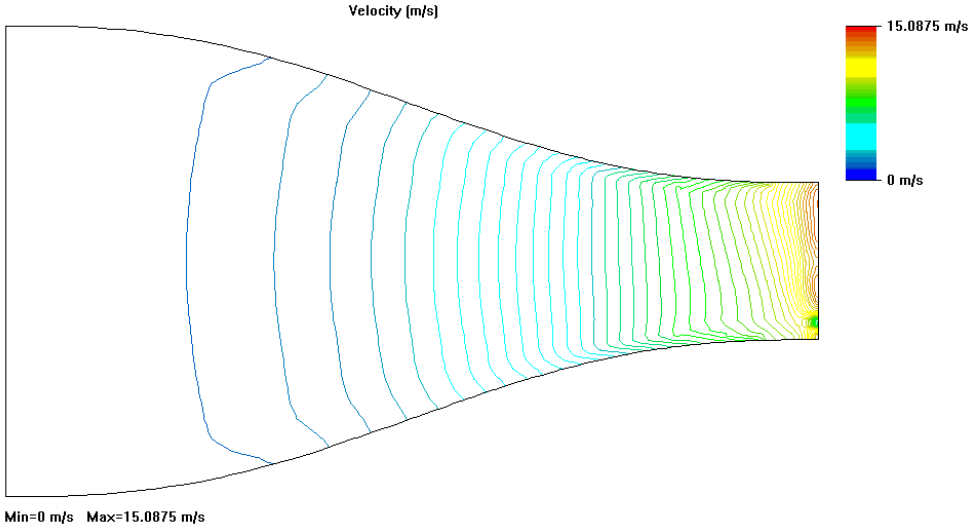

Figure 3.6: $\frac{L_{contraction}}{H_{in}}$=1.75, Side view showing the velocity isolines

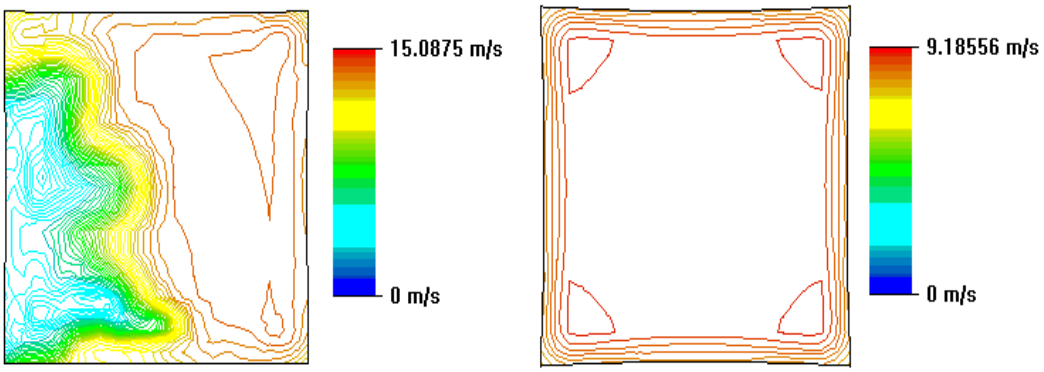

Figure 3.7: View from the nozzle exit, showing the velocity isolines. $\frac{L_{contraction}}{H_{in}}$= 1.45 on the right and 1.75 on the left

From the quick investigation it can be seen that $\frac{L_{contraction}}{H_{in}}$ of 1.45 is suitable for the contraction nozzle in terms of velocity uniformity (Figures 3.5 and 3.7). The velocity uniformity is distorted when $\frac{L_{contraction}}{H_{in}}$ is 1.75 (Figures 3.6 and 3.7), as it is close to the boundary separation value shown in Figure 3.4.

The final specifications of the contraction nozzle are shown in the Table 3.5 below:

Properties	Specifications
Contraction ratio, *c* (*mm*)	8.6
Inlet Height, H_{in} (*mm*)	182
Outlet Height, H_{out} (*mm*)	62
Contraction Length, $L_{contraction}$ (*mm*)	264
Contraction length to inlet height ratio, $L_{contraction}/H_{in}$	1.45
Contraction shape type	3-D 5^{th} Order polynomial
Material	PLA

Table 3.5: Contraction nozzle dimensions and properties

3.2.3 Settling chamber

The main purpose of the settling chamber ($2-4$, shown in the schematic, Figure 3.2) is to increase the uniformity of the flow, in other words, clean the excessive turbulence. The honeycomb is an important component of the settling chamber, as it aids in reducing the turbulence level of the airflow.

According to Mehta et al. [6,7], there should be at least 150 cells per the settling chamber height. Furthermore, the cell length is about $6-8$ times the chambers height. The height of the settling chamber is 182 *mm*, same as the inlet height of the contraction nozzle (H_{in}=$H_{chamber}$). The cell height is 1.5 *mm*. Furthermore, it was suggested in [7] that the spacing between the screen region and honeycomb should be $0.2H_{in}$. Also the spacing between any numbers of screens should be $0.2H_{in}$. Similarly, the spacing between the last screen and the nozzle inlet advised be $0.2H_{in}$. The rig is designed and mapped onto an existing wind tunnel, that is found in Coventry University. The existing design used two screens, and a honeycomb. Therefore the honeycomb here is placed away from the contraction nozzle inlet by $0.6H_{in} = 109mm$. The honeycomb (Figure 3.11) is designed and manufactured using the same 3-D printer (Ultimaker 3 extended). The length of the upstream section is 522 *mm* (which is 10 *x* $D_{BSPpipe}$ to allow proper mixing between the potential core region of the jet and the turbulent region, Figure 3.9). The specifications of the honeycomb are shown below in table 3.6:

Properties	**Specifications**
Length (*mm*)	11
Height (*mm*)	182
Width (*mm*)	182
Number of cells	$\approx$ 160
Material	PLA

Table 3.6: Designed Honeycomb

3.2.4 Test section

The test section (6, shown in the schematic, Figure 3.2), will hold the scaled up channel with porous medium plates attached to its sides. Due to space limitation in the laboratory, the maximum length of the test section is 270 *mm* (considering space limitations). The test section is comprised of two aluminium plates with porous mediums attached to its sides, through slots.

3.2.4.1 Aluminium Plates

The aluminium plates are part of the test section. During scale up, it is important to increase the length of the channel compared to a typical filter channel. However, due to space limitation in the laboratory, the maximum length of the test section is 270 *mm* as specified earlier. The two plates are made of 4 *mm* thick aluminium, with 5 *mm* groves on the sides to slot in the porous medium plates. Due to the limitations of the build environment of the Ultimaker 3 extended 3-D printer, it would be risky to print out that part of the test section separately, as this might cause flow separation, therefore to avoid any risky approach, two aluminium plates were manufactured using CNC (The plate can be seen in Figure 3.12). Design can be seen in Appendix A 6.1, Figure 6.2 .

27 pressure taps were added on one aluminium plate (refer to Figure 4.3). Holes of 1.7 *mm* were drilled throughout the middle of the plates, each separated by a distance of 10 *mm*. The last three taps are separated by a distance of 5 *mm* near the end of the channel. A simple schematic of the tappings is shown in Chapter 4, section 4.2, Figure 4.1.

3.2.4.2 Porous walls

The porous walls are also a part of the test section configuration. In this experiment, a study will be carried out with three porous walls (can be seen in Figure 3.13). The porosities chosen were at low percentages (15%,20% and 37%), since there are a lot of experimental data with high porosities (explained in section 3.1).

The walls are 5 *mm* thick, 270 *mm* in length and 62 *mm* wide. The pores radii are 2 *mm*. The porosity percentages of the walls were calculated using equation 3.5.

$$\epsilon_p = \frac{V_{pores}}{V_{tot}} x100 \tag{3.5}$$

Where ϵ_p is the porosity level, V_{pores} is the pores volume, and V_{tot} is the total volume of the plate.

3.3 Rig manufacture

Most of the rig was manufactured using 3-D printing technology. The contraction nozzle was designed using SOLIDWORKS, which can be seen in Appendix A 6.1 , Figure 6.1 . It was then manufactured using Ultimaker 3 extended 3-D printer, which has the build volume of 215 *mm x* 215 *mm x* 300 *mm*. The printer's build speed is up to 16 mm^3/s. The manufactured contraction nozzle is shown in Figure 3.8.

Some materials have been removed due to 3rd party copyright. The unabridged version can be viewed in Lancester Library - Coventry University.

(a) Side view **(b)** Front view

Figure 3.8: 3-D printed, three dimensional 5^{th} Order Polynomial Contraction Nozzle.

The upstream section of the contraction nozzle (settling chamber) is manufactured using the same printer, this is shown in Figures 3.9 and 3.10 . The honeycomb is a part of the settling chamber, and the component is also manufactured using the same printer, the part is shown in Figure 3.11 .

Some materials have been removed due to 3rd party copyright. The unabridged version can be viewed in Lancester Library - Coventry University.

Figure 3.9: Full assembly of the upstream section with the Contraction nozzle

Some materials have been removed due to 3rd party copyright. The unabridged version can be viewed in Lancester Library - Coventry University.

Figure 3.10: Settling chamber connected to air pipe supply

Some materials have been removed due to 3rd party copyright. The unabridged version can be viewed in Lancester Library - Coventry University.

Figure 3.11: Honeycomb 182 *mm x* 182 *mm x* 11 *mm*

The test section is made out of two parts, as explained in section 3.2.4. The first part are the aluminium plates, that were manufactured using a CNC, which can be seen in Figure 3.12 .

Some materials have been removed due to 3rd party copyright. The unabridged version can be viewed in Lancester Library - Coventry University.

Figure 3.12: Top view of the aluminium plate with pressure taps (taps were flush to the wall)

The second part, are the porous walls. Three porous walls (15%,20% and 37%) were rapidly manufactured using the Ultimaker 3 extended 3-D printer. The porous walls are shown in Figure 3.13. 15% wall design is shown in Appendix A 6.1 , Figure 6.3.

Some materials have been removed due to 3rd party copyright. The unabridged version can be viewed in Lancester Library - Coventry University.

(a) 15% Porosity plate **(b)** 20% Porosity plate

Some materials have been removed due to 3rd party copyright. The unabridged version can be viewed in Lancester Library - Coventry University.

(c) 37% Porosity plate

Figure 3.13: 3-D printed porosity plates, all of dimensions: 270 *mm x* 62 *mm x* 5 *mm*

3.4 Instrumentation

This section will outline the instruments used in the present experimental program. It has been outlined earlier in the test matrix shown in Table 3.3, what measurements were taken. The Hot Wire Anemometer specifications are shown in Table 3.7. Also, the pressure scanners (Scanivalve) specifications are shown in Table 3.8.

Features	**Specifications**
Operating resistance	2 to 80 ohms
Resistance measurement	0.1% $\pm$0.01 ohms
Maximum probe current	800 mA
Cable length	5 m or 30 m
Output	Bridge voltage to 11.5 volts
Frequency response	$>$ 250 kHz (without tuning)
Maximum operating temperature	250^{o}C
Size	17.8 cm x 48 cm x 41 cm
Signal conditioning	Offset; 0 to 10 V in 10 mV steps, 0.15% accuracy. Gain; 1 to 1000 V, 0.15% accuracy. Output; $-$5 to +5 V

Table 3.7: TSI IFA 300

Features	**Specifications**
Accuracy	$\pm$.05%
Pressure range	$0 - 750$ psi
Scan rate	500 Hz/Channel
Resolution	16 bit
Power requirements	28Vdc
Maximum reference pressure	250 psig (1725 kPa)
Operating temperature	0^{o}C to 60^{o}C
Weight	6.4 lbs. (2.9 kg)

Table 3.8: DSA 3217 scanivalve

3.4.1 Hot Wire Anemometer and Scanivalve

The velocity measurements were recorded using the Hot Wire Anemometer (HWA) system which is the TSI IFA 300, that is a constant temperature type (specifications are in Table 3.7). The probes were 5 μm platinum-plated tungsten wire (Dantec 55 P11) and were calibrated using a fully automatic TSI 1129 calibration rig. The probe here is calibrated using two nozzles (Nozzle #2 and #3) installed in the TSI 1129 calibration rig (can be seen in Appendix B, Figure 6.5). Nozzle #2 (can be seen in Appendix B, Figure 6.4) is used for the measurements in section 3.5.1. This nozzle calibrates the probe from 0 m/s to 50 m/s. The calibration error is shown in Figure 3.14. Whereas, nozzle #3 is used to calibrate the probe from 0 m/s to 5 m/s, which will be used in the measurements outlined in Chapter 4 , section 4.4 . The calibration errors of the probe with nozzle #3 is shown in Figure 3.15. The precision of the instrument (HWA), show that the measurements are $\pm$0.07 m/s of the mean centreline velocity (U_c). Calculations are shown below for measurements of velocity centreline at m_f = 30 g/s [64] ;

$$precision = U_{cmax} - U_{cmin} = 6.606 - 6.536 = 0.07\, m/s$$

$$U_c = \frac{6.606 + 6.595 + 6.585 + 6.536}{4} = 6.581 \pm 0.07\, m/s$$

Matter can not be created nor destroyed, this is known as the conservation of mass. Therefore, the mass flow rate entering the contraction nozzle (m_f) should be equal to the mass flow rate exiting it (Experimental value, $m_{f\,out}$). The mass flow rate entering the nozzle (Accepted value, (m_f)) is known from the Volume Flow Meter (VFM) which is 30 g/s. Therefore from the measured or experimental value obtained by the HWA, it is easy to calculate the mass flow rate exiting the nozzle;

$$m_f = m_{f\,out}$$

$$m_f = 30\, g/s$$

$$m_{f\,out} = \rho A U_c$$

$$m_{f\,out} = 1.225\,x\,0.062\,x\,0.062\,x\,6.581 = 0.0309\,kg/s = 30.9\,g/s$$

The error between the accepted value (m_f) from the VFM and experimental value ($m_{f\,out}$) from the HWA is 3%, which it can be concluded that the instrument is accurate, and precise ± 0.069949. The error calculation is shown below;

$$\%Error = \frac{Experimental\ value - Accepted\ value}{Accepted\ value}$$

$$\%Error = \frac{30.9 - 30}{30} = 0.03$$

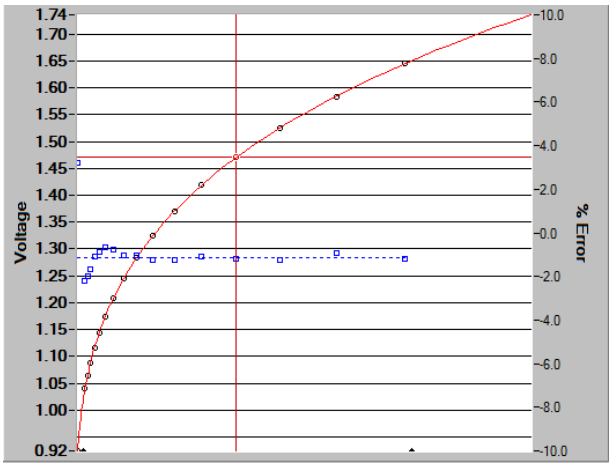

Figure 3.14: Probe calibration errors with nozzle #2. Blue squares; errors in voltages with respect to velocity, "o"; measured voltages with respect to velocity, polynomial curve (-); for observation

Following the test matrix, in table 3.3, the final test was carried out is the velocity profiles downstream of the porous wall.

The hot wire probe is calibrated using nozzle number 3, that is installed in the TSI 1129 calibration system. Nozzle 3 covers velocities from 0.1 to 5 m/s, which is the expected magnitude of the velocities away from the side walls. Figure 3.15, shows the errors covered during the calibration, which are roughly between -1% and 4%.

Two frequency tests were carried out (Figure 3.16) by taking consequent measurements with different sample frequencies. It can be seen that with sample rate of 2kHz, the velocities converge faster than the ones with sample rate of 1kHz. Furthermore, to compromise with the test time consumption, a period of 2s, with sample rate of 2kHz, is sufficient.

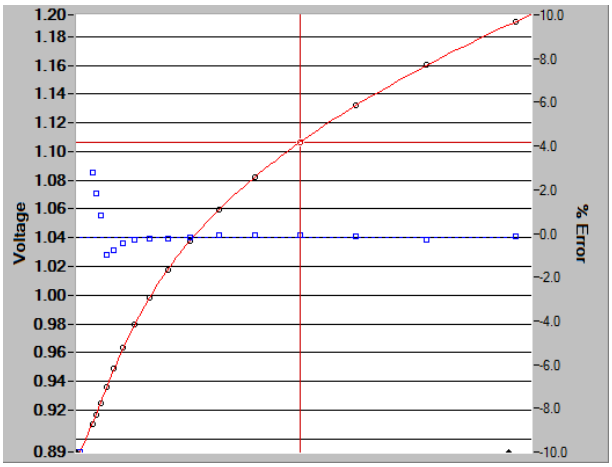

Figure 3.15: Probe calibration errors with nozzle #3. Blue squares; errors with respect to velocity, "o"; measured voltages with respect to velocity, polynomial curve (-); for observation

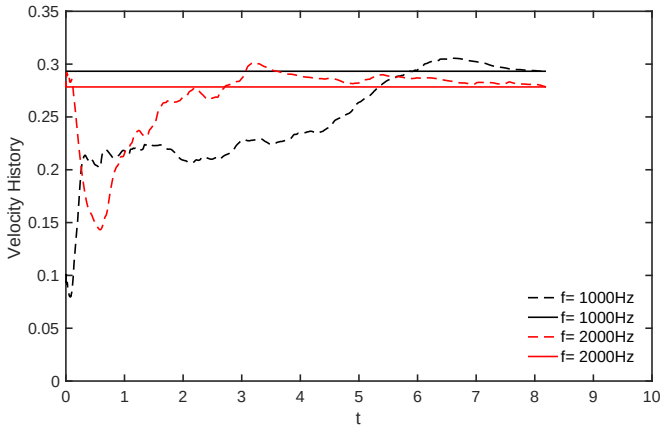

Figure 3.16: Sample rate test, solid lines; Mean velocities, dashed lines; time averaged velocities

The traverse used is precise, 1 $mm \pm 0.0125\,mm$. The VFM readings of the air supply with all mass flow rates used were fluctuating within $\pm 4\,Pa$ of the mean pressure. Lastly, the pressure measurements were recorded using a DSA 3217 scanivalve (specifications are in Table 3.8). This scanivalve incorporates 16 channels. The scan period of each test at different mass flow rate and porous wall was $2000\mu s$, and 240 samples were used to calculate the averaged value.

3.5 Experimental rig characterisation

In this section, an investigation is carried out to check whether a honeycomb would be needed in the experimental program. Initially, it is thought that the contraction nozzle itself would be sufficient to reduce the turbulence levels and increase the flow uniformity. The first step would be to carry out a convergence study (section 3.5.1.1), and check whether the velocity readings would converge. The second step is to analyse the flow uniformity of the velocity profiles and the turbulence levels of the exit flow at the contraction nozzle (section 3.5.1.2).

3.5.1 Contraction nozzle evaluation

This section explains the rig evaluation process. Tests were carried out using four mass flow rates (m_f = $10\,g/s$, $16\,g/s$, $24\,g/s$, $30\,g/s$). The velocities were measured along the horizontal and vertical line at the exit of the nozzle, outlined in Figure 3.20, respectively. The readings were recorded without the filter channel attached. The measurements have been performed twice. Firstly, without using the honeycomb (assuming that the contraction nozzle alone will reduce the turbulence levels). Secondly, using the honeycomb, in case the assumption that the contraction nozzle will reduce the turbulence fails. The test conditions are shown in Table 3.9. A simple schematic of the measurement orientation is shown in Figure 3.20. The convergence criteria is then analysed in section 3.5.1.1, and the profiles are plotted in section 3.5.1.2.

Table 3.9: Contraction nozzle test conditions

Profile	**Test conditions**
Horizontal (H) and vertical (V)	m_f=10 g/s, 16 g/s, 24 g/s, 30 g/s Sample rate= 1000 Hz Sample period= 32s

3.5.1.1 Sampling criteria

The convergence study is an essential part of any experimental testing. The study shows how the measured values depend on the frequency (sample rate) and number of samples. Furthermore, it'll be concluded in the end at which number of samples the tests would converge.

The HWA system used is TSI IFA 300, which is a constant temperature type (As explained in section 3.4). The probes were 5 μm platinum-plated tungsten wires (Dantec 55 P11) and were calibrated using a fully automatic TSI 1129 calibration rig. The probe here is calibrated using Nozzle 2, which covers velocities from 0 to 50 m/s. The calibration errors are shown in Figure 3.14. The errors are between -1% and 3%. The traverse was set up to move horizontally and vertically to cover the necessarily profiles. The convergence study carried out here is at a sample location on the horizontal and vertical axis of the nozzle exit (shown in Figure 3.17).

Sampling rate of 1kHz was used over 32s for each samples. The number of samples of each test were 32000 (refer to Table 3.9). The traverse holding the probe, is set to move with the increment of 1 mm through the testing area (contraction nozzle outlet). Figure 3.20, shows the horizontal (marked as H) and vertical (marked as V) profiles orientation. The outcomes of each profiles are shown in Table 3.10 . The measurement set up is shown in table 3.9 , and they are similar for all the tests. To check the velocity profiles across the corners, follow Appendix C 6.3 .

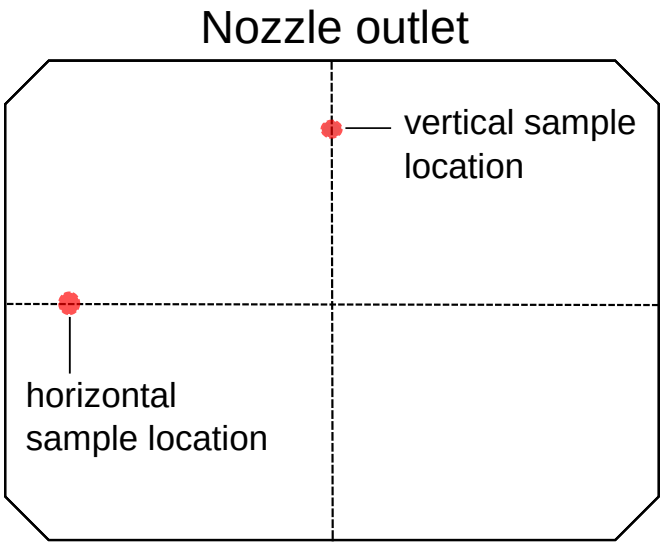

Figure 3.17: Samples locations

The parameters to be tested are shown below in Table 3.10 ;

Sample location	**Parameter**
Horizontal-vertical sample location	Running average velocity, U_r, (Equation 3.6)
	Running average root mean squared velocity, U_{rms}, (Equation
	Running average turbulent intensity, Tu, (Equation 3.8)
	Velocity exit profile
	Turbulent exit profile

Table 3.10: Convergence criteria (with and without the honeycomb)

In practice, the measured velocities from the HWA are a series of discrete points. If the flow is steady and laminar, $u^{'}(t) = 0$ (no turbulent fluctuations ($u^{'}$) or $U_r = U_{mean}$ for all time (t). The convergence study would help confirming that statement. Below are the equations used during the study;

$$U_r = U_{mean} + u^{'}(t) \tag{3.6}$$

$$U_{rms} = \sqrt{\overline{u^{'}(t)}^2} \tag{3.7}$$

$$Tu = \frac{U_{rms}}{U_{mean}} \tag{3.8}$$

Table 3.11: Reynolds numbers at the nozzle's outlet (Re_{outlet}), with the presence and absence of the honeycomb

Mass flow rate (g/s)	Re_{outlet} **with no honeycomb**	Re_{outlet} **with honeycomb**
10	9,440	9,440
16	10,000	14,500
24	17,600	18,400
30	21,100	25,100

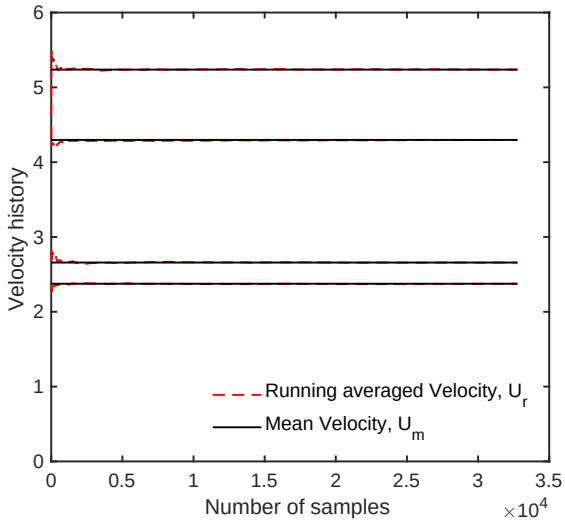

(a) Velocity history with the honeycomb abscent

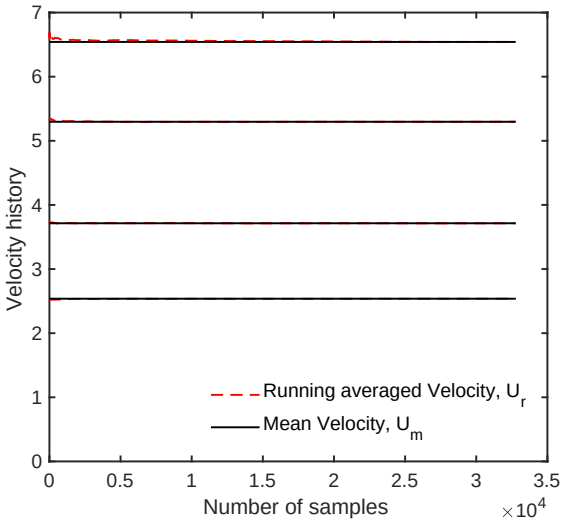

(b) Velocity history with the honeycomb present

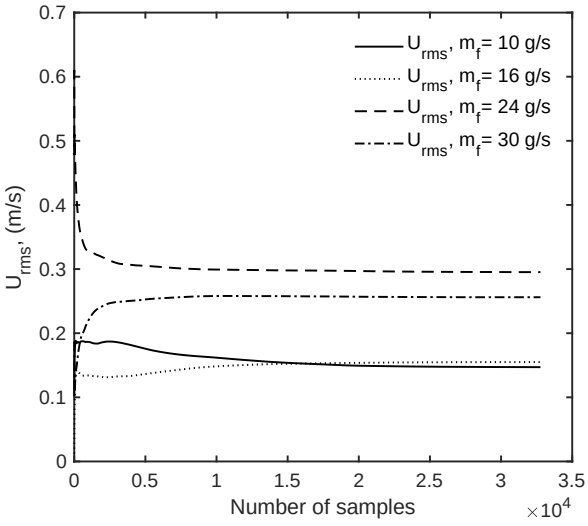

(c) Root mean squared velocity history with the honeycomb abscent

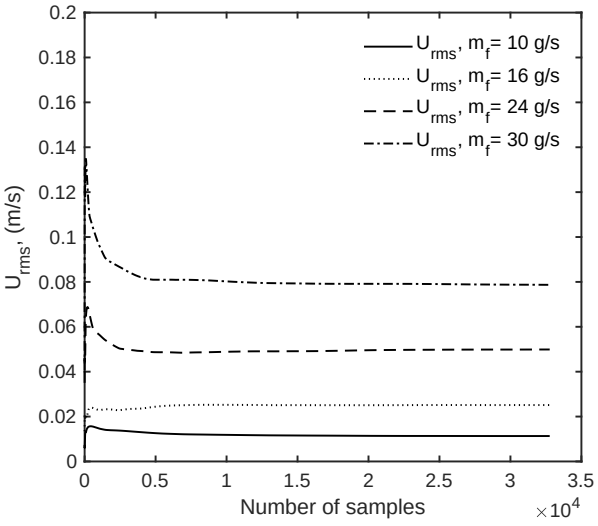

(d) Root mean squared velocity history with the honeycomb present

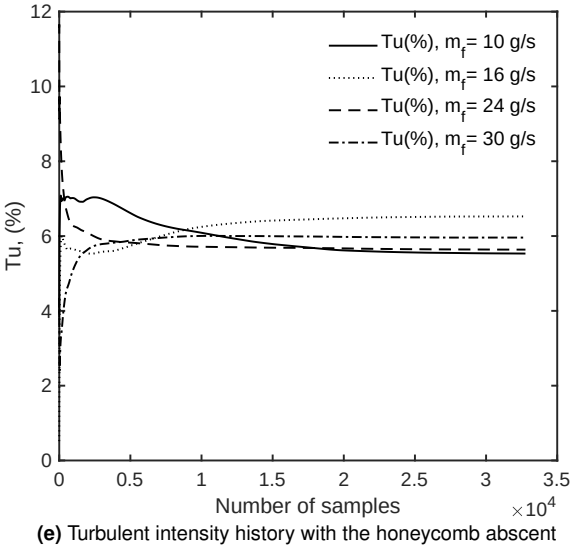

(e) Turbulent intensity history with the honeycomb abscent

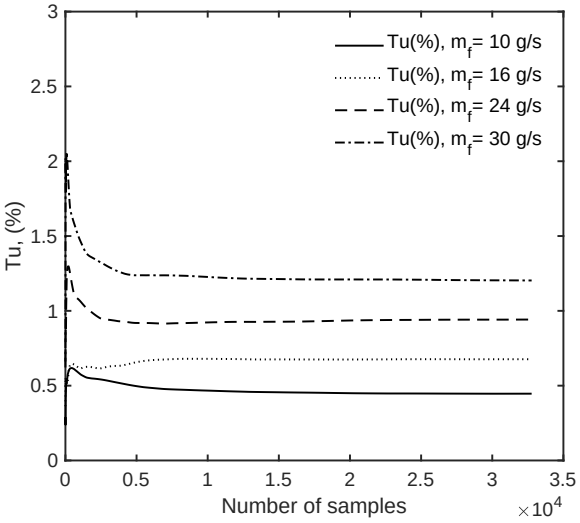

(f) Turbulent intensity history with the honeycomb present

Figure 3.18: Effect of the honeycomb presence on the convergence study at the sample location along the horizontal axis

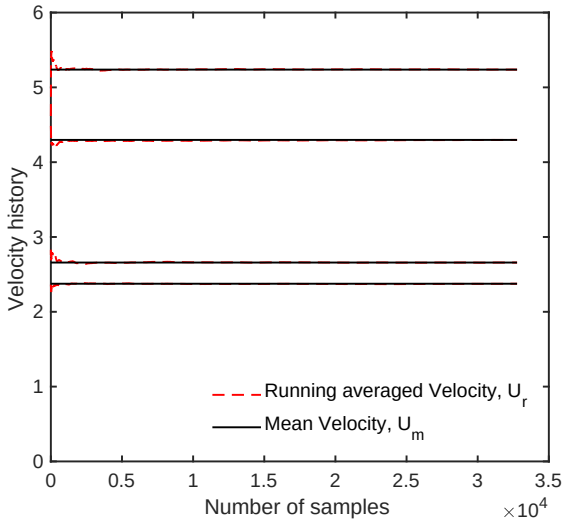

(a) Velocity history with the honeycomb abscent

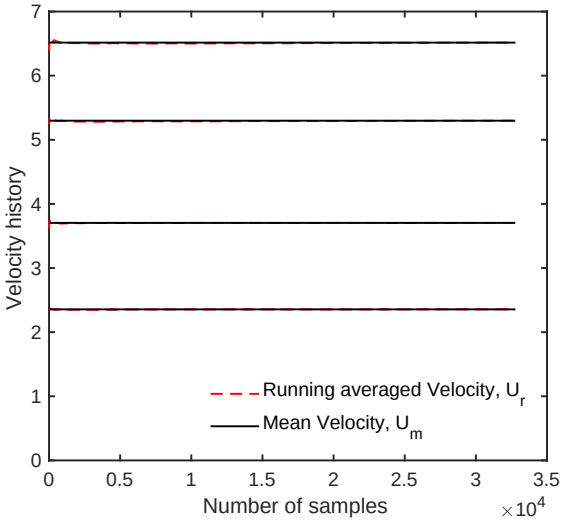

(b) Velocity history with the honeycomb present

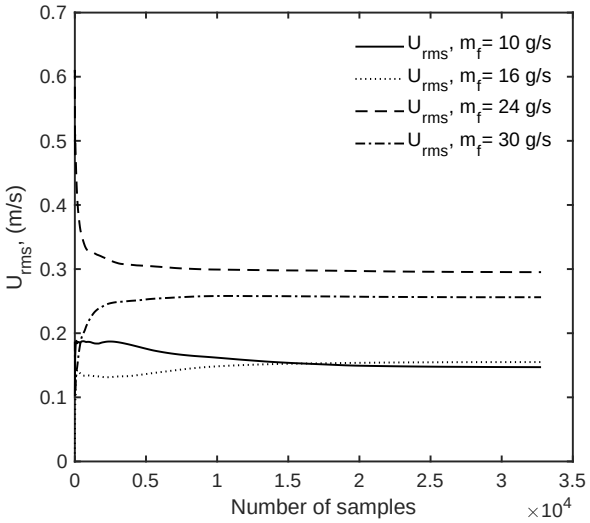

(c) Root mean squared velocity history with the honeycomb abscent

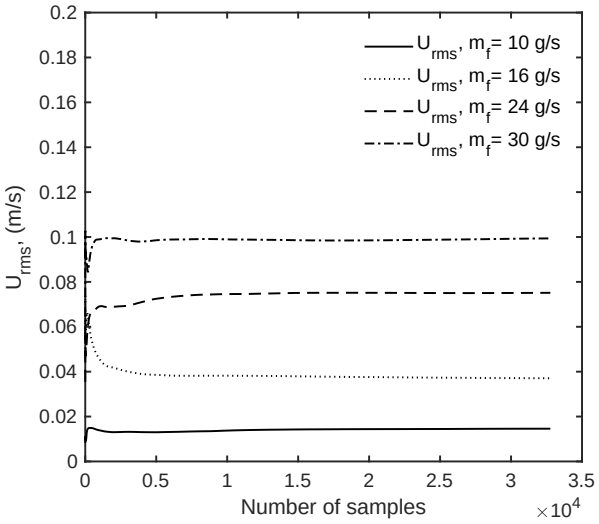

(d) Root mean squared velocity history with the honeycomb present

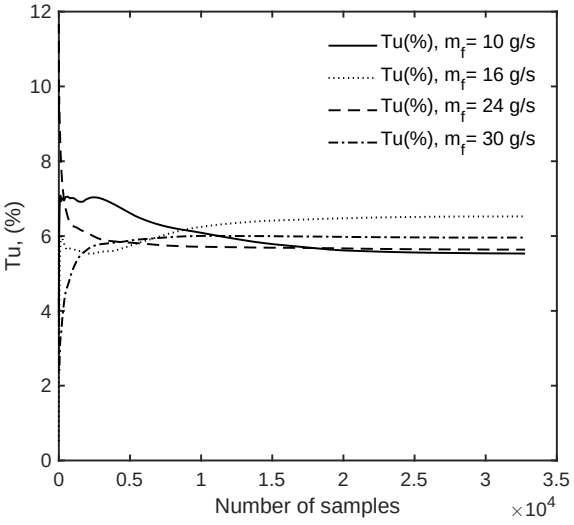

(e) Turbulent intensity history with the honeycomb abscent

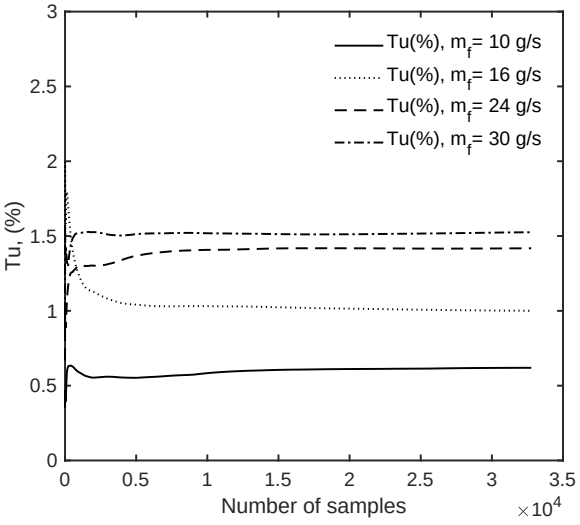

(f) Turbulent intensity history with the honeycomb present

Figure 3.19: Effect of the honeycomb presence on the convergence study at the sample location along the vertical axis

It can be seen that the results take longer time to converge when the honeycomb is absent (Figure 3.18a and 3.19a), however when using the honeycomb, the results converge very much faster, shown in Figures 3.18b and 3.19b for samples at the horizontal and vertical axis respectively. It is safe to say that all the results converge after approximately $2x10^4$ number of samples. Initial tests show that with the honeycomb installed in the rig, the turbulence levels decrease drastically (Figures 3.18f and 3.19f) compared with no honeycomb (Figures 3.18e and 3.19e)in both horizontal and vertical samples respectively. So the next step is to confirm the initial thought, by assessing the physical features of the contraction nozzle (section 3.5.1.2).

3.5.1.2 Exit velocity and turbulence intensity profiles

The important aim of using a low-speed contraction nozzle, is to have a uniform velocity profiles and low turbulence levels (explained in details, in Chapter 3, section 3.2.2). Therefore a study is carried out to view the effect of the honeycomb on the flow uniformity. The data are post-processed by analysing the velocity and turbulence intensity profiles along the horizontal and vertical orientation of the nozzle exit (follow the schematic below in Figure 3.20).

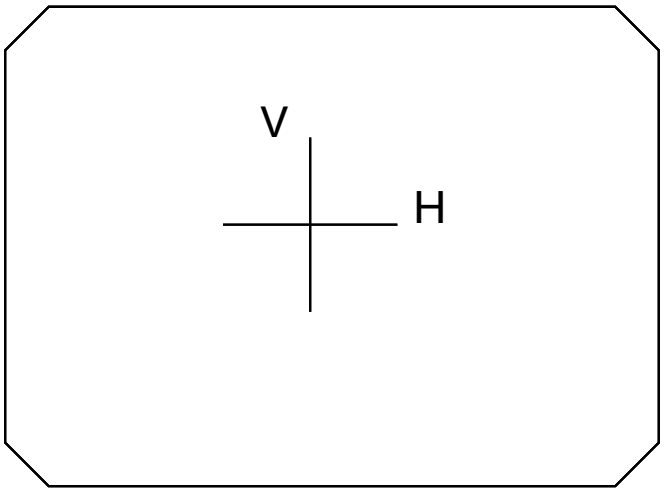

Figure 3.20: Measurement orientation

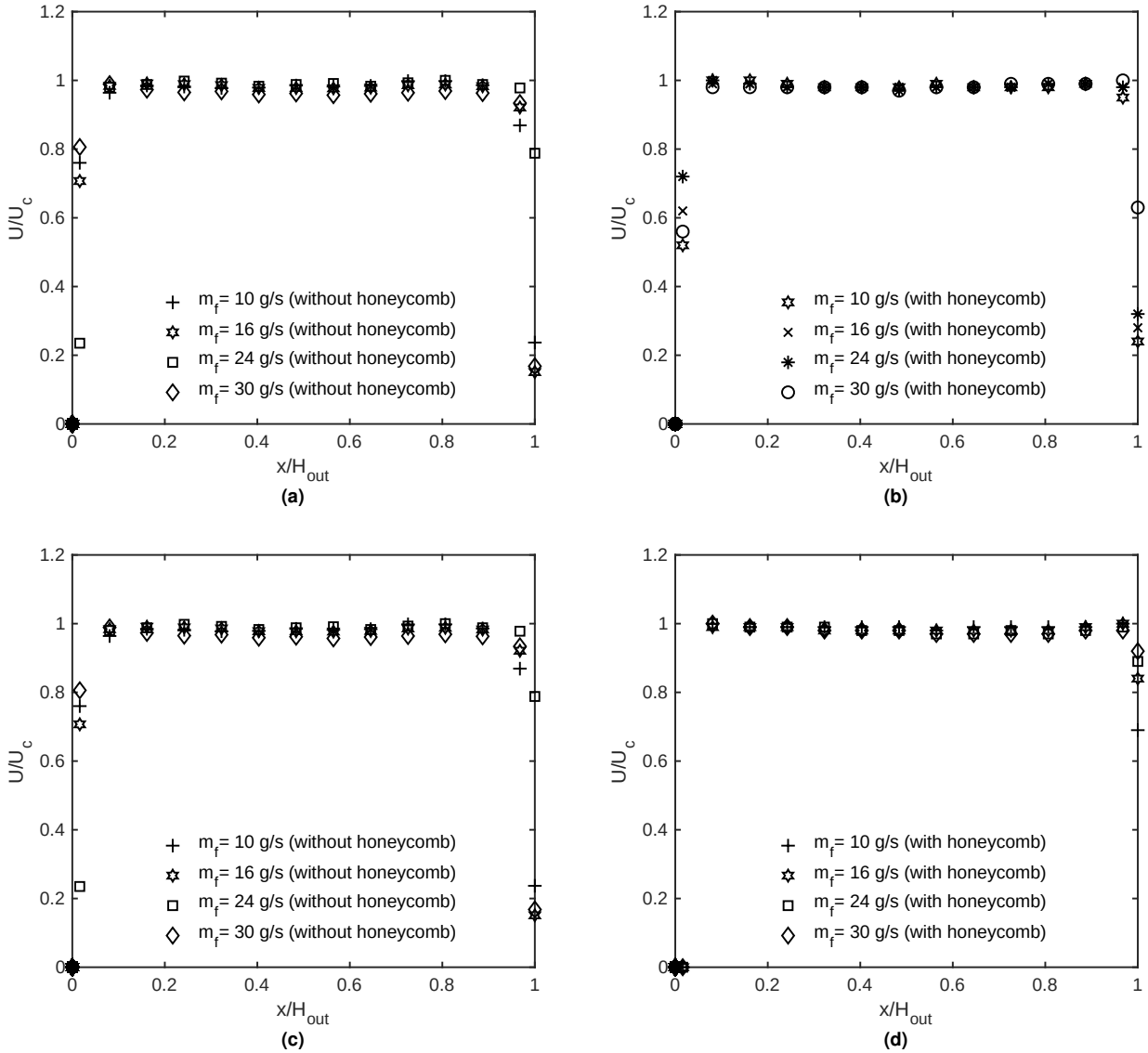

Figure 3.21: Non-dimensional velocity profiles (Horizontal and Vertical) against non-dimensional nozzle outlet height. **(a)**; Horizontal profile without the honeycomb. **(b)**; Horizontal profile with the honeycomb. **(c)**; Vertical profile without the honeycomb. **(d)**; Vertical profile with the honeycomb.

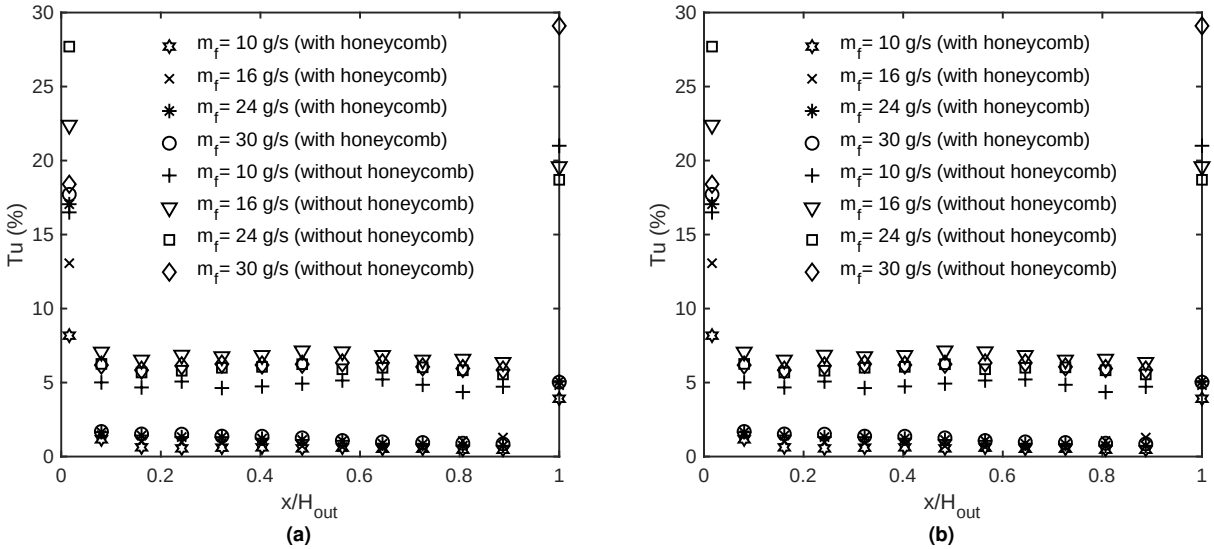

Figure 3.22: Turbulent intensity profiles at the nozzle outlet (Horizontal and profile), with and without the honeycomb. **(a)**; Turbulent intensities of the horizontal profile (with and without the honeycomb), (Tu (%)). **(b)**; Turbulent intensities of the vertical profile (with and without the honeycomb), (Tu (%)).

The velocity profiles are non-dimensionalised using the centre line velocity (U_c), and the nozzle exit length is non-dimensionalised using the nozzle exit height. The turbulent intensities are plotted against the non-dimensional length of the nozzle. Results are noted below:

1. The flow is partially uniform with no honeycomb, with the presence of some fluctuations. These are shown in Figures 3.21c and 3.21a, for vertical and horizontal profiles, respectively.

2. The turbulence levels decrease by almost 95% when the honeycomb is present. This can be seen in Figures 3.22b and 3.22a, for vertical and horizontal profiles, respectively.

3. The flow is more uniform with the honeycomb, compared to the one without it. Results are shown in Figures 3.21d and 3.21b, for vertical and horizontal profiles, respectively.

The assumption that the contraction nozzle will be sufficient to decrease the turbulence levels, and give the flow its perfect uniformity, failed. Therefore, the honeycomb will be used throughout the experimental program. Furthermore, the functionality of the 3-D contraction nozzle is now validated, and ready to be used for the experimental program.

Chapter 4

Results and Discussion

4.1 Introduction

After validating the rig, and its components, it is time to validated the functionality of the porous walls printed (Figure 3.13). In addition to the validation, the next step would be to study the flow in the single channel, and the effect of low porosities on the flow field.

The aim of this section is to investigate the effect of different porosities side walls on the pressure profiles within the channel, and the velocity exit profiles through the side walls. Furthermore, an investigation of how both, pressure and velocity profiles behave at different mass flow rates are carried out. The instrumentations used here are the HWA and DSA 3217 pressure scanners (16 bit scanivalve).

4.2 Porous wall characterisation

The schematic shown below in Figure 4.1, illustrates the procedure, on how to characterise the porous walls (15% , 20% , 37%).

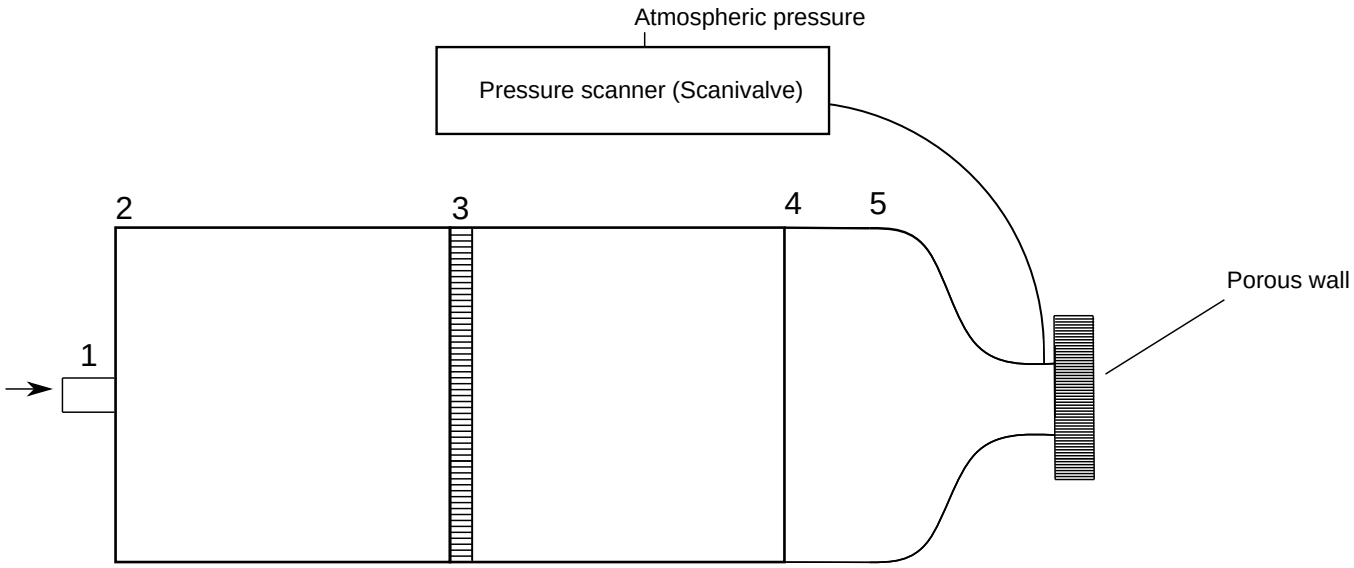

Figure 4.1: Schematic of the porous walls characterisation procedure

A pressure tapping hole of 1.7 *mm* is placed 10 *mm* upstream of the test section(advised by Konstandopoulos et al. [11], when measuring the pressure drop). A DSA 3217 scanivalve was used to measure upstream pressure while the downstream pressure of the porous wall is atmospheric. The results are shown in Figure 4.2a.

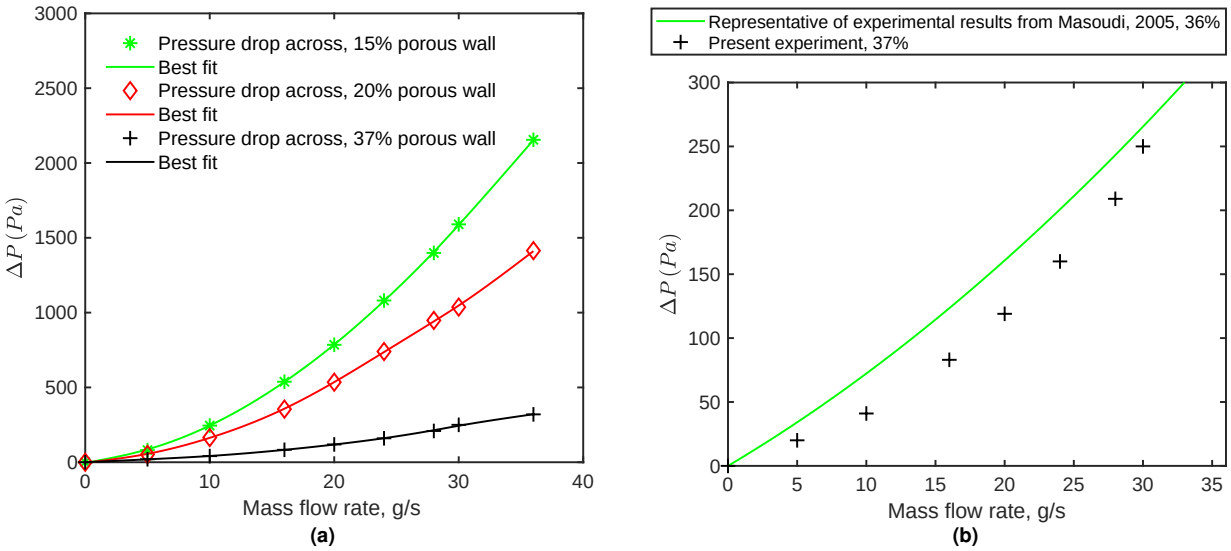

Figure 4.2: Pressure drop across the porous walls, and experimental comparison with previous work. **(a)**; Pressure drop across three porous walls (15% , 20% , 37%), (ΔP). **(b)**; Comparison with previous work done by Masoudi et al. [8].

As expected when the porosities decrease, the pressure drop increases due to the high resistive property of the wall (Figure 4.2a). Furthermore, the results obtained by Masoudi et al. [15], are a good agreement with the results obtained in the present work, with little deviations ($<$ 2%), can be seen in Figure 4.2b.

4.3 Pressure distribution along the channel with porous walls

In this section, the study of the pressure distribution, through a single filter channel with different side walls porosities is carried out. Following, Table 3.3 , the measurements include the local pressure distribution at the channel. The scan period of each test was 2000μs, and 240 samples were used to calculate the averaged value. A simple sketch is provided to illustrate the procedure (shown in Figure 4.3):

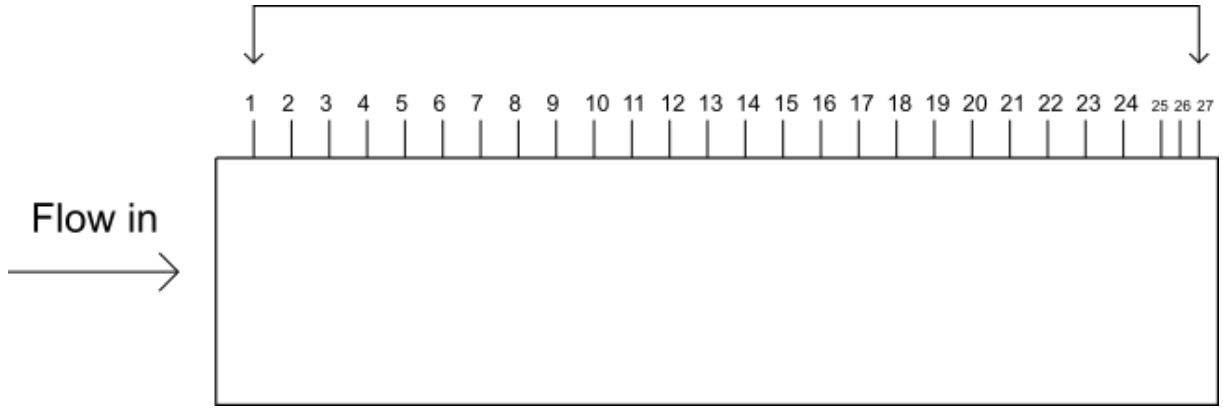

Figure 4.3: Schematic of the pressure taps along the channel

4.3.1 Effect of mass flow rate on the pressure distribution

In this section, the pressure distributions along the channel filter were plotted at different mass flow rates (10 g/s,20 g/s,30 g/s,40 g/s,50 g/s, and 60 g/s) for each porous walls (15%, 20%, and 37%).

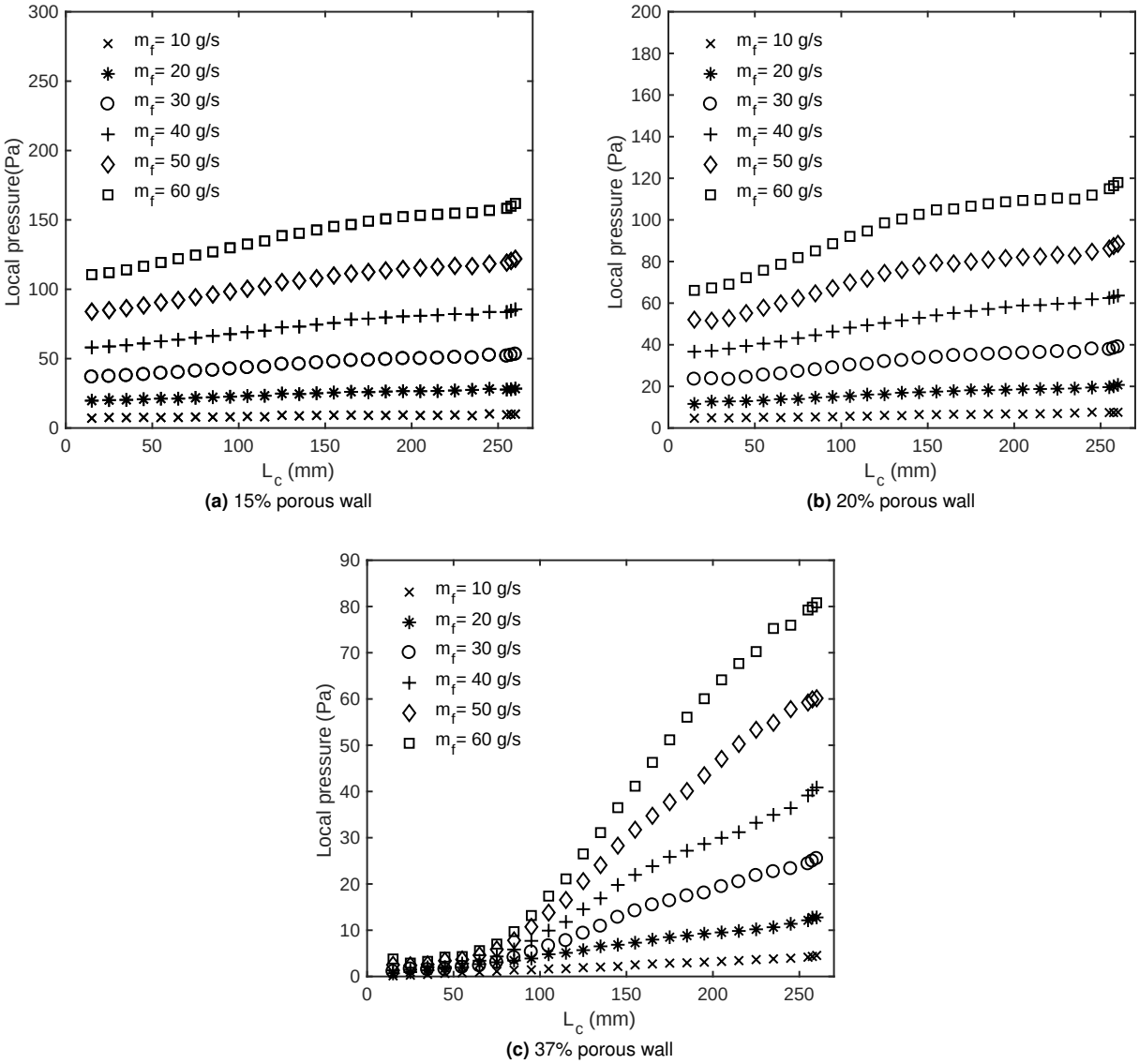

(a) 15% porous wall

(b) 20% porous wall

(c) 37% porous wall

Figure 4.4: Pressure distribution along the channel filter with the three side wall porosities, at different mass flow rates

It seems that for lower porosities, the 15% and 20% (Figures 4.4a , and 4.4b), the dynamic pressure is a smaller fraction of the total pressure drop across the wall and therefore the flow is less biased towards the downstream end of the channel, that is due to the high resistance imposed by the low porosity side walls, so it has to distribute more evenly along the length of the channel filter. However that is different with the 37% porous side wall, the pressure drop across the wall is low and the flow approaches that of a system with no wall (shown in Figure 4.4c).

4.3.2 Effect of porosities on the pressure distribution

The pressure distributions along the channel were plotted separately with each porous wall (15%, 20% and 37%) at the same mass flow rate. This way the effect of porosities can be seen clearly, making it easier to draw conclusions.

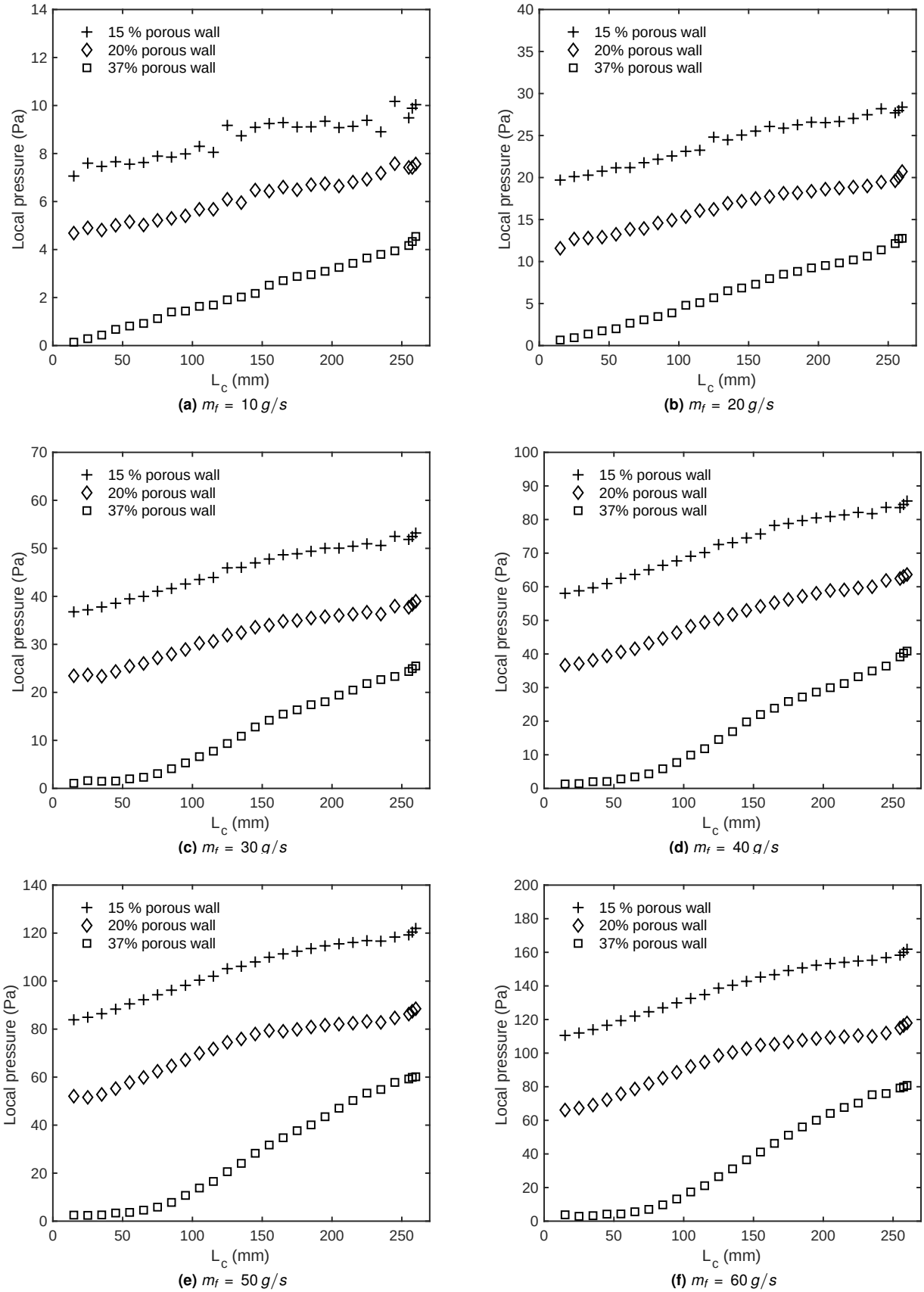

(a) $m_f = 10\,g/s$ **(b)** $m_f = 20\,g/s$

(c) $m_f = 30\,g/s$ **(d)** $m_f = 40\,g/s$

(e) $m_f = 50\,g/s$ **(f)** $m_f = 60\,g/s$

Figure 4.5: Pressure drop distribution along the channel, showing different porosity levels at the same mass flow rate.

Figure 4.5 shows that the pressure increases linearly along the channel for all of the samples, up to mass flow rate of 20 g/s (Figures 4.5a and 4.5b). The pressure distribution increases non-linearly along the channel, with 37% porosity filter at mass flow rates greater than 20 g/s (Figures 4.5c , 4.5d , 4.5e, and 4.5f). The non-linear behaviour is still observable with 37% porosity filter, when the mass flow rate is above 20 g/s (Figure 4.4c). This is consistent with the 1-D model introduced by Konstandopolous et al. [14]. As a summary;

- Pressure drop distribution is linearly increasing along the channel, for both mass flow rates of 10 g/s and 20 g/s, and the behaviour is the same with all side walls porosities. (Figure 4.5a and 4.5b)

- When the flow is higher than 20 g/s, with side walls of 37% porosity, the behaviour of the pressure distribution is different. The pressure is non-linearly increasing along the channel, this can be seen in Figures 4.5c , 4.5d , 4.5e and 4.5f.

- Pressure distribution changes to a non-linear behaviour, with side walls porosity of 20%, at mass flow rates higher than 40 g/s. This can be shown in Figures 4.5e , and 4.5f .

- The flow velocity in the porous wall is dependent on the pressure drop across the porous wall. The pressure in the upstream and downstream channel is a function of the relative stagnation or flow speed of the fluid as some mass is transferred through the porous walls.The relation between the porosity and pressure drop is inversely proportional, when the porosity is high, the pressure drop across the wall is low and therefore flow meets less resistance and hence approaches that of a system with no wall. That means most of the flow escape through the wall at the downstream end of the channel where the dynamic pressure has a more significant influence on the wall flows. On the contrary, when the porosity is low, the dynamic pressure is a smaller fraction of the total pressure drop across the wall and therefore the flow is less biased towards the downstream end of the channel.

4.4 Velocity profiles exiting the porous walls

The schematic in Figure 4.6, illustrates the testing procedure. Velocity readings were taken at different distances away from the wall (marked as Z). Z values were: 5 *mm*, 10 *mm*, 20 *mm*, 40 *mm*, 60 *mm*, and 80 *mm*. The probe calibration procedure is explained in Chapter 3, section 3.4. The test conditions are described in the Table 4.1.

Table 4.1: Porous wall test conditions

Profile	**Test conditions**
Porous wall	m_f=20 g/s, 30 g/s, 40 g/s, 60 g/s Sample rate= 2000 Hz Sample period= 2s Z= 5,10,20,40,60,80 mm with m_f= 20 and 30 g/s Z= 40,60,80 mm with m_f= 40 and 60 g/s

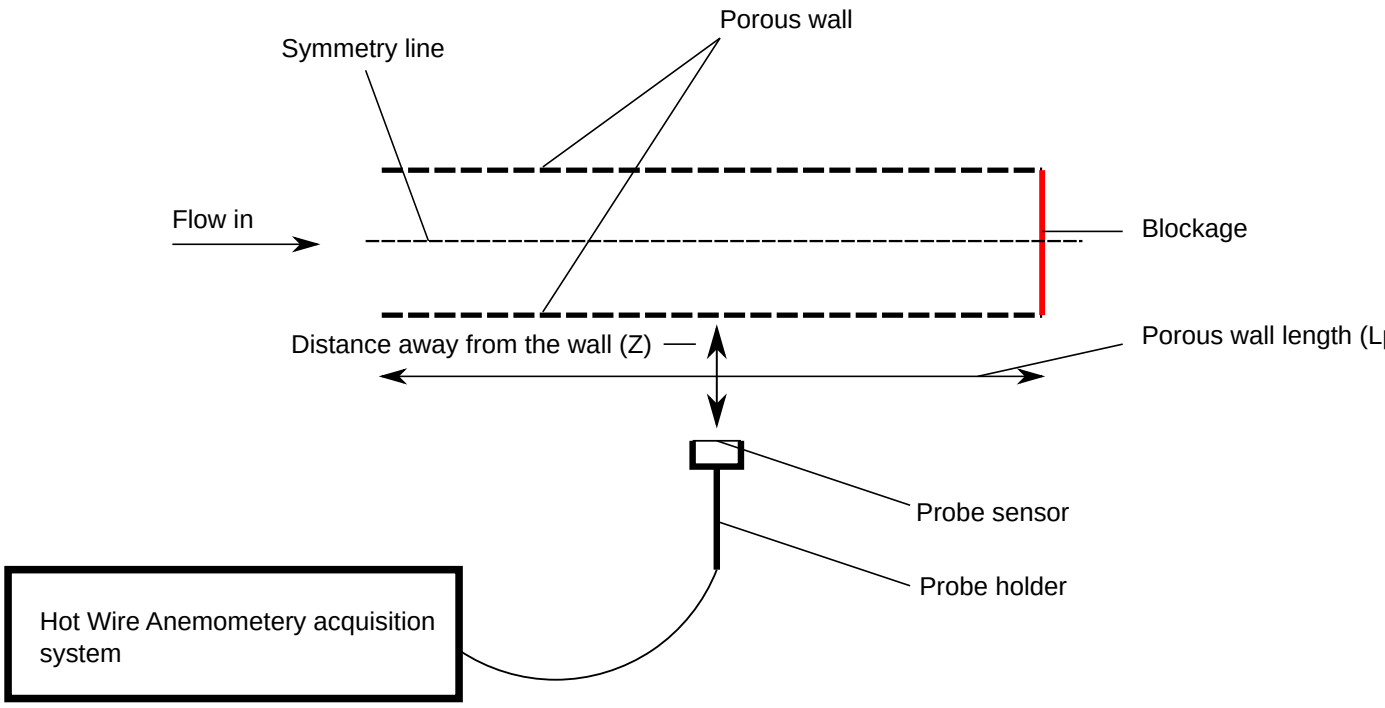

Figure 4.6: Velocity measurement procedure

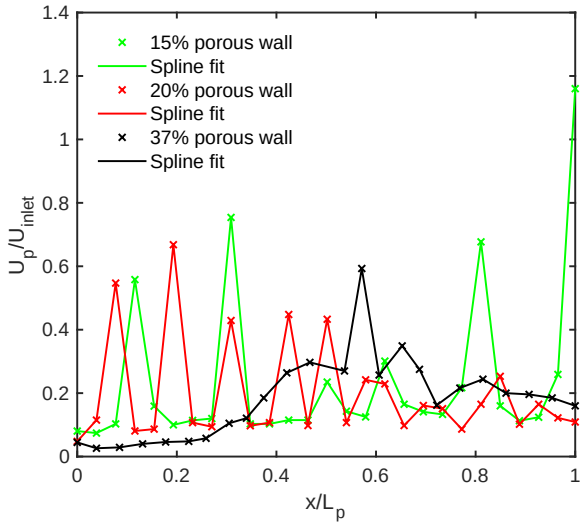

(a) 5 mm, away from filter wall

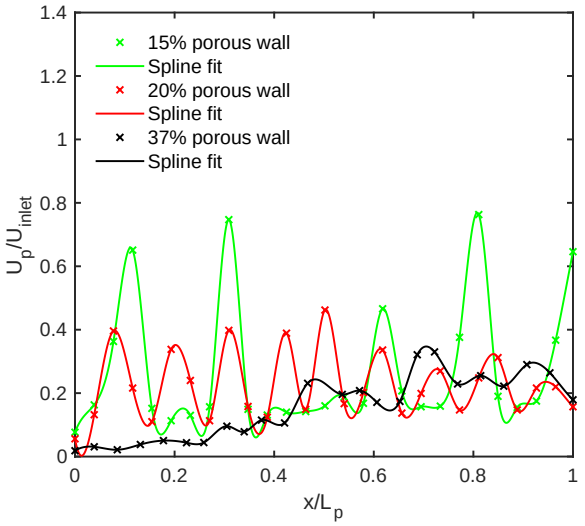

(b) 10 mm, away from filter wall

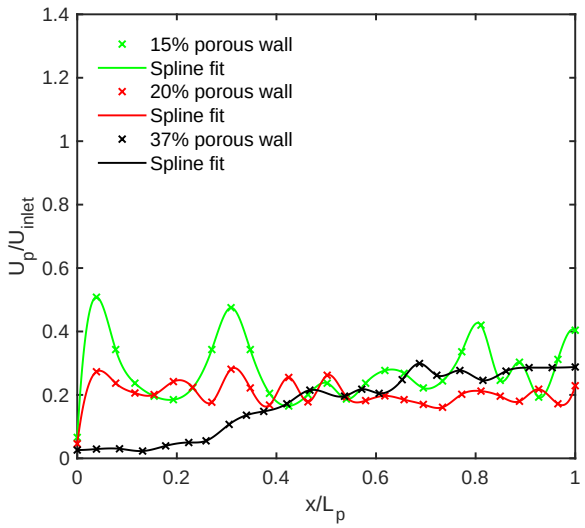

(c) 20 mm, away from filter wall

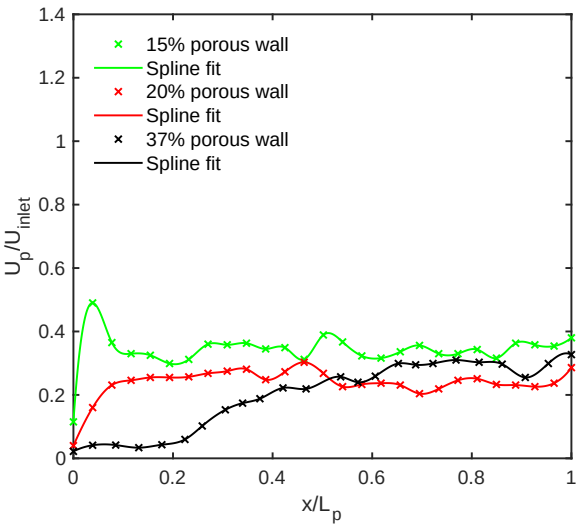

(d) 40 mm, away from filter wall

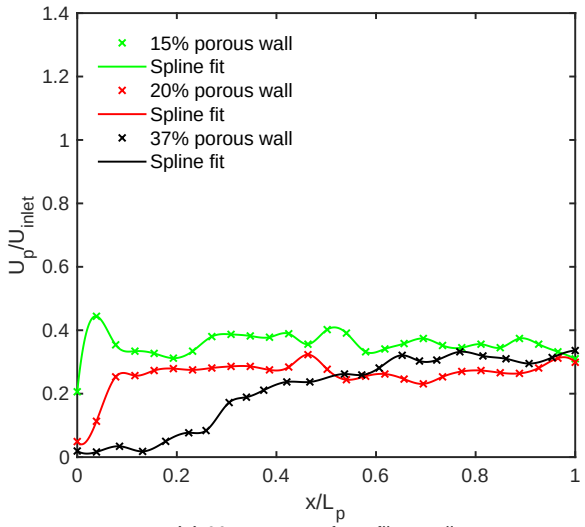

(e) 60 mm, away from filter wall

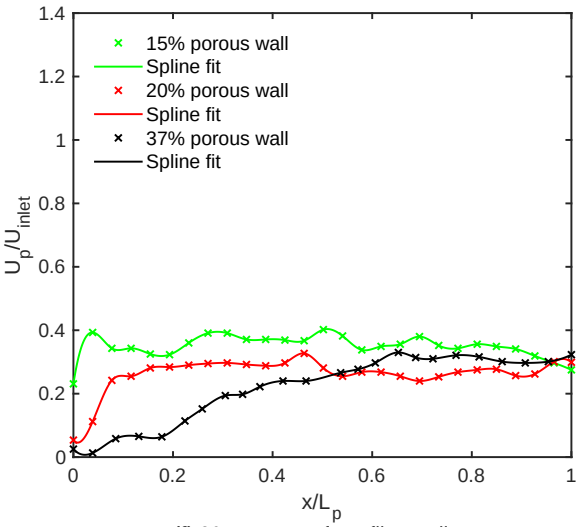

(f) 80 mm, away from filter wall

Figure 4.7: Non-dimensional velocity exit profiles through the three porous filters, at $m_f = 20\,g/s$

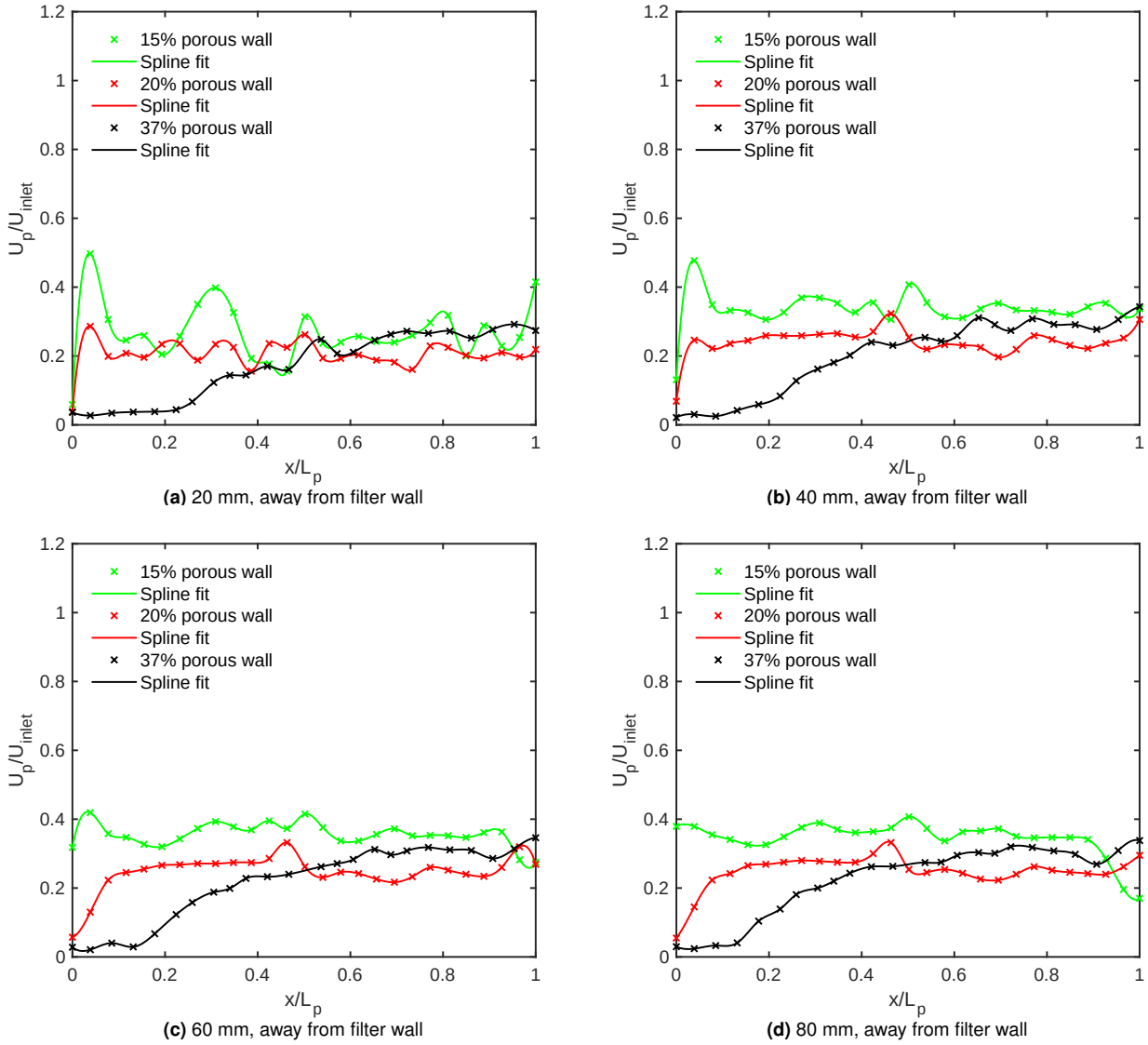

(a) 20 mm, away from filter wall

(b) 40 mm, away from filter wall

(c) 60 mm, away from filter wall

(d) 80 mm, away from filter wall

Figure 4.8: Non-dimensional velocity exit profiles through the three porous filters, at $m_f = 30\,g/s$

As a sanity remark, the spline fit in the plots are the cubic interpolation used in MatLab.

When the probe is close to the porous side wall (5 *mm*, 10 *mm* and 20 *mm*), the hot wire probe picks up the jet formation, these are shown Figures 4.7a , 4.7b , and 4.7c. However, when the probe is further from the wall, (40 *mm*, 60 *mm* and 80 *mm*), the velocity profiles are smoother shown in Figures 4.7d , 4.7e , and 4.7f. This suggests that the jet flow is mixed properly at these regions.

Velocity profiles, start to smooth out when the probe is 60 *mm* from the wall.

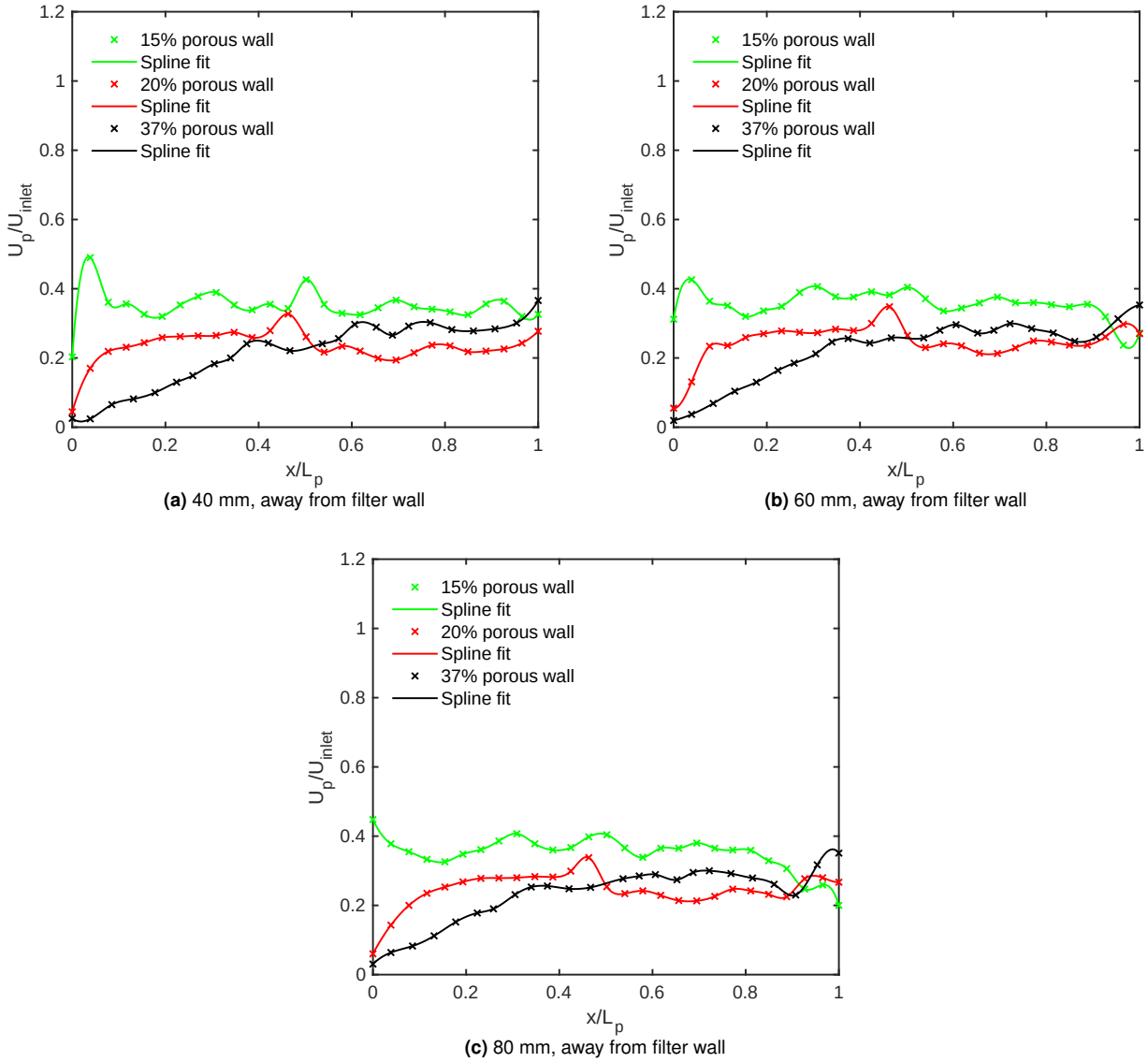

(a) 40 mm, away from filter wall

(b) 60 mm, away from filter wall

(c) 80 mm, away from filter wall

Figure 4.9: Non-dimensional velocity exit profiles through the three porous filters, at $m_f = 40\,g/s$

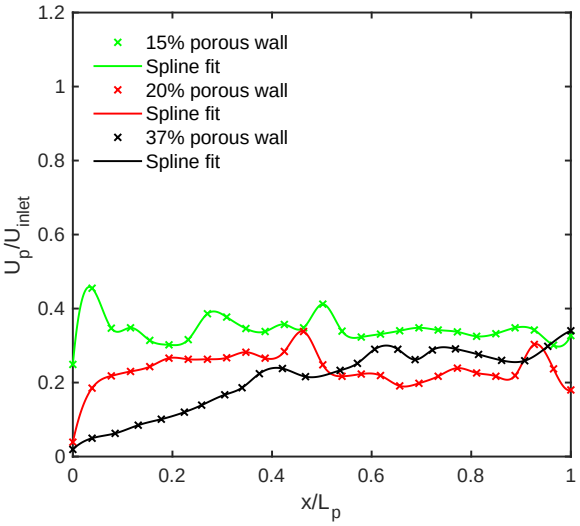

(a) 40 mm, away from filter wall

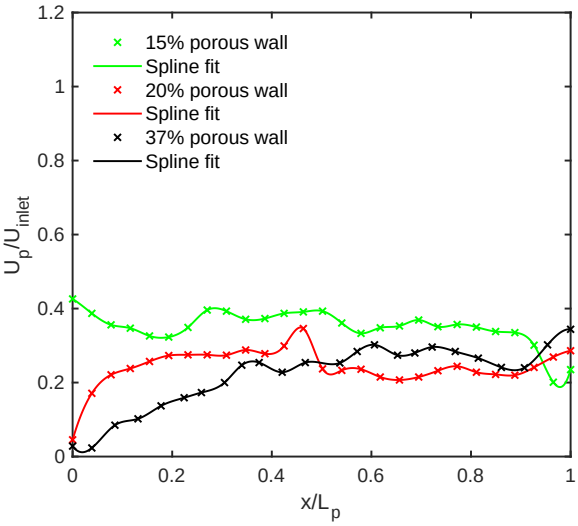

(b) 60 mm, away from filter wall

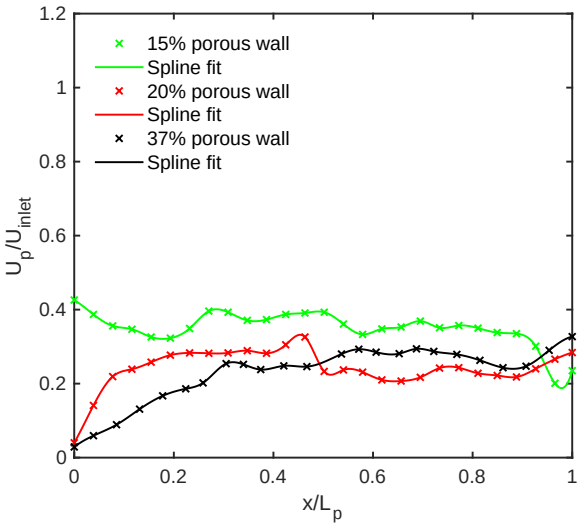

(c) 80 mm, away from filter wall

Figure 4.10: Non-dimensional velocity exit profiles through the three porous filters, at $m_f = 60\,g/s$

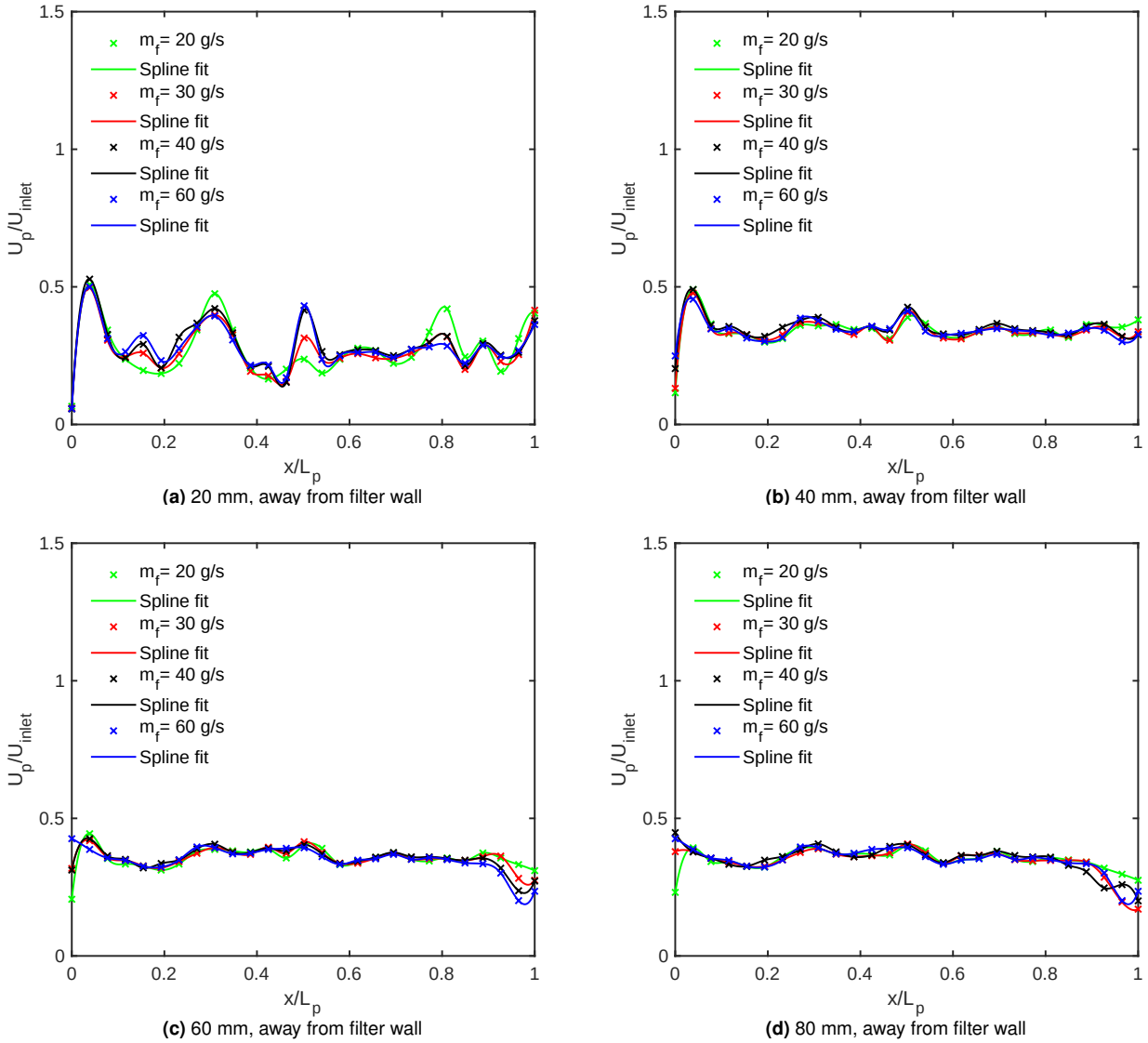

(a) 20 mm, away from filter wall

(b) 40 mm, away from filter wall

(c) 60 mm, away from filter wall

(d) 80 mm, away from filter wall

Figure 4.11: Non-dimensional velocity exit profiles through the 15% porous filter at different mass flow rates (m_f)

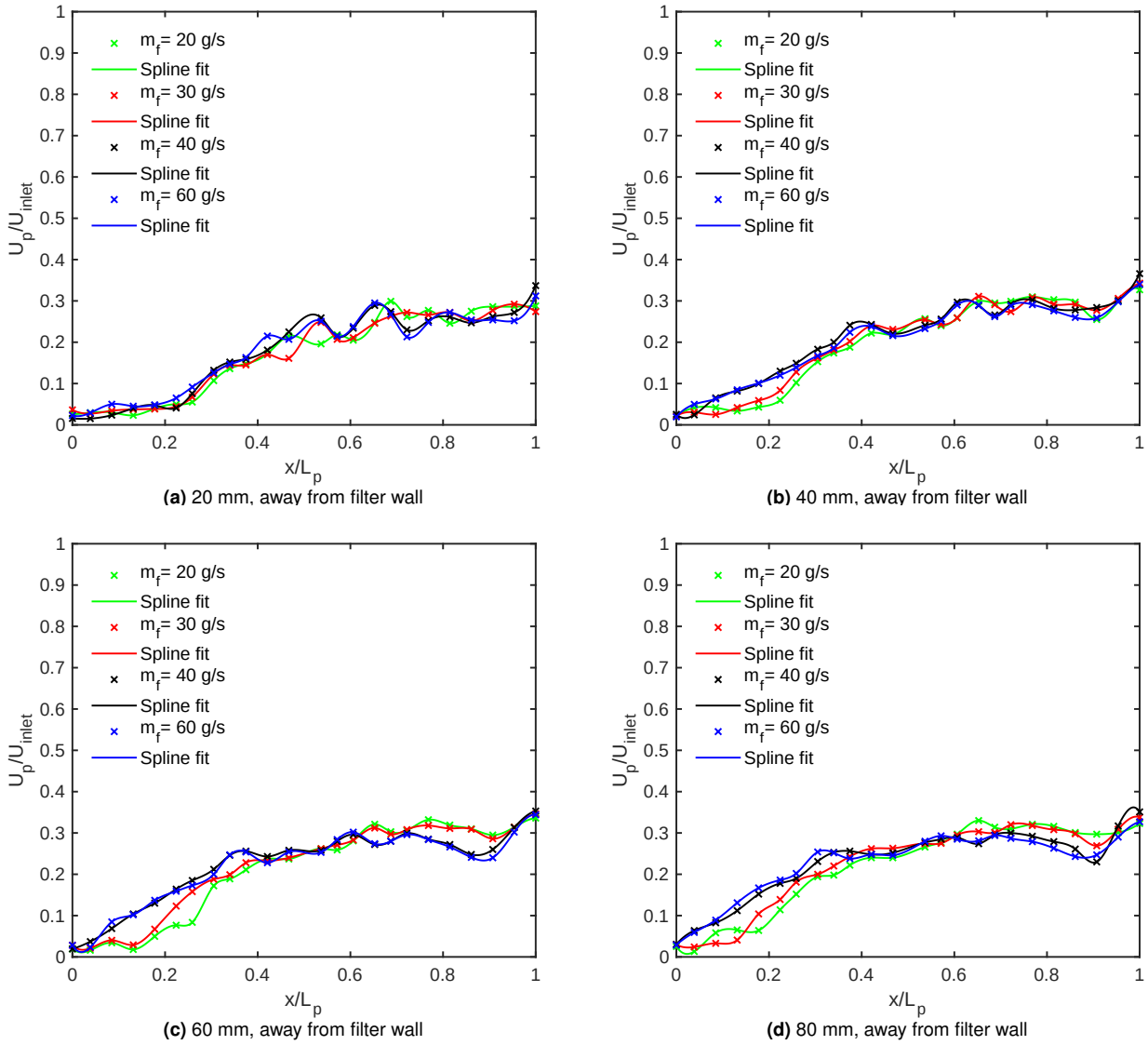

(a) 20 mm, away from filter wall

(b) 40 mm, away from filter wall

(c) 60 mm, away from filter wall

(d) 80 mm, away from filter wall

Figure 4.12: Non-dimensional velocity exit profiles through the 37% porous filter at different mass flow rates (m_f)

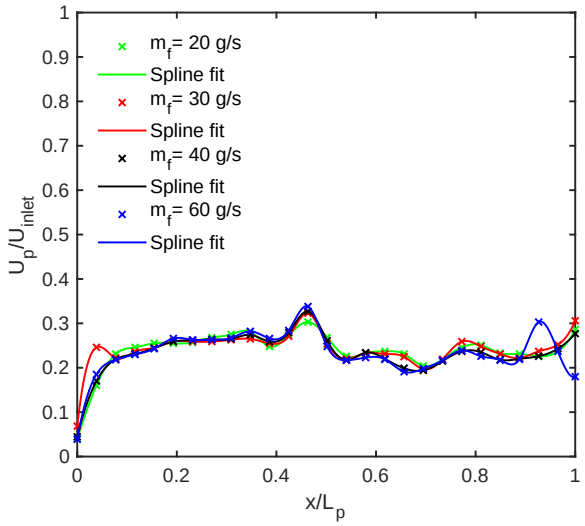

(a) 40 mm, away from filter wall

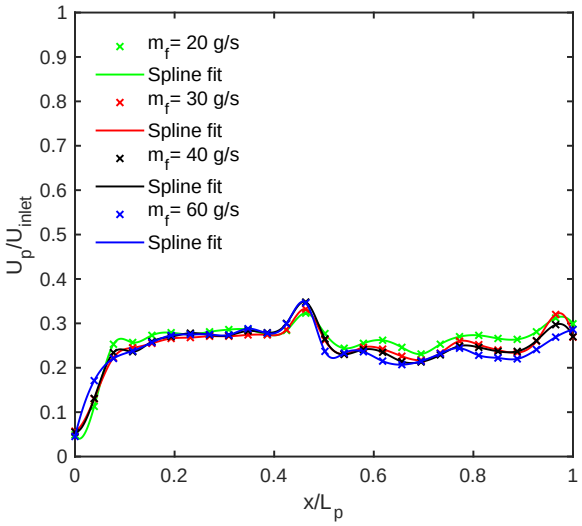

(b) 60 mm, away from filter wall

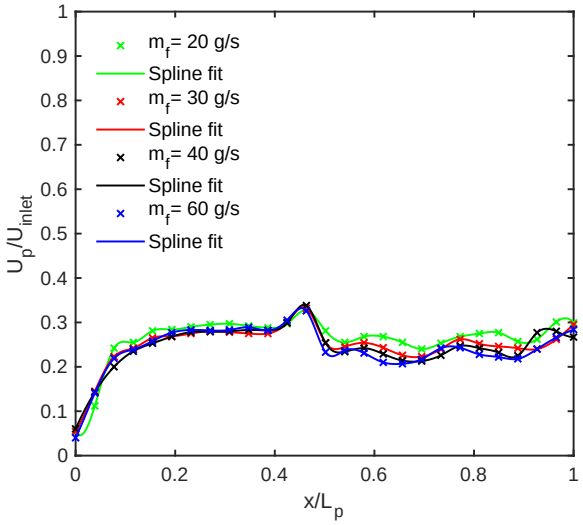

(c) 80 mm, away from filter wall

Figure 4.13: Non-dimensional velocity exit profiles through the 20% porous filter at different mass flow rates (m_f)

The Reynolds numbers through the pores of different porous walls are calculated (Equation 4.1), at different mass flow rates and quantified in a tabular form shown in Table 4.2:

$$Re_{avg\,min} = \frac{D_p U_{avg\,min}}{\nu}$$
$$Re_{avg\,max} = \frac{D_p U_{avg\,max}}{\nu} \tag{4.1}$$

Porous walls	Minimum Reynolds numbers, $Re_{avg\,min}$	Maximum Reynolds numbers, $Re_{avg\,max}$
15%	212	556
20%	159	383
37%	132	363

Table 4.2: Minimum and maximum averaged Reynolds numbers in the pores of different porous plates

4.5 Summary

Following the results, the points below are identified:

- When the probe is away from the wall at distances of 5 *mm*, 10 *mm* and 20 *mm* from the porous wall, the velocity profiles are highly non-uniform at mass flow rate of 20 g/s. That is due to the jets formed through the porous pores. This can be shown in Figures 4.7a , 4.7b , and 4.7c . That is observed with all wall porosities. The velocities are of low magnitude, which was expected from the literature (Chapter 2, section 2.5).

- When the probe is away by a distance greater than 20 *mm*, the velocity profiles becomes smoother at mass flow rate of 20 g/s. Which suggests that the jet flow is mixed properly at that region. This can be seen in Figures 4.7d , 4.7e , and 4.7f . The behaviour is similar for all side wall porosities.

- Velocity becomes smooth at distances of 60 *mm* and 80 *mm* away from the porous wall. The profiles in this region, are quite similar at different porosities, with different mass flow rates. The behaviour can be shown in Figures 4.12 (37% porosity wall) , 4.13 (20% porosity wall) and 4.11 (15% porosity wall).

- With porous wall of 15% porosity, at $\frac{x}{L_p} = 0.3$ that is 81 *mm* of the channel length shows a velocity peak. The peak can be seen in Figure 4.11d and exists with all mass flow rates.

- With porous filter of 20%, there is a velocity peak at a position $\frac{x}{L_p} = 0.45$ that is 121.5 *mm* of the channel length. The peak can be seen in Figure 4.13c. The peak exists with all mass flow rates.

- With porous filter of 37%, the velocity peak is at the end of the channel length. The peak can be seen in Figure 4.13c and exists with all mass flow rates.

Chapter 5

Conclusions

An experimental program has been presented to investigate the air flow in a scaled up single channel filter, and the effect of low porosity side walls on the flow field. The methodology is based on pressure and velocity measurements. Three porous walls were used for testing, specifically with 15%,20% and 37% porosity.

The test rig was characterised by analysing the velocity and turbulent intensity profiles across the contraction nozzle exit. The measurements were taken along the horizontal and vertical lines at the nozzle exit. The tests were carried out under four different mass flow rates (10 g/s, 16 g/s, 24 g/s, and 30 g/s). Initially it was assumed that the precence of the contraction nozzle would be sufficient to reduce the turbulence levels of the flow and increase its uniformity, however it was found that the honeycomb was required to improve the flow uniformity through the contraction exit, and reduce the flows turbulent intensity.

After validating the upstream section of the channel filter, the next step was to characterise the porous walls. The characterisation procedure was carried out for eight mass flow rates, 5 g/s, 10 g/s, 16 g/s, 20 g/s, 24 g/s, 28 g/s, 30 g/s, and 36 g/s. With the highest porosity level (37%), the pressure drop is low compared to the lower porosity levels (15% and 20%). Furthermore, the measured pressure drop for the 37% porosity wall was compared with an existing experiment performed by Masoudi et al. [15] on monolithic filter of 36% porosity. The comparison shows a very good agreement, with $<$ 2% deviation (rough estimation).

Once the porous walls have been characterised, the pressure drop along the channel filter was measured. The measurements were carried out for six mass flow rates, 10 g/s, 20 g/s, 30 g/s, 40 g/s, 50 g/s, and 60 g/s. The results have shown that the pressure increases linearly along

the channel with all porous walls, up to mass flow rate of 20 g/s. However, the pressure increases non-linearly along the channel, with 37% porosity filter at mass flow rates greater than 20 g/s. The non-linear behaviour is still observable with 37% porosity filter, when the mass flow rate is above 20 g/s. This is consistent with the 1-D model introduced by Konstandopolous et al. [14]. It seems that for lower porosities (15% and 20%), the flow is less biased towards the downstream end of the channel. This is due to the high resistance imposed by the low porosity side walls, so the flow has to distribute more evenly along the length of the channel filter. However that is different for the 37% porous side wall.

At last the velocity exit profiles downstream of the porous walls were measured for four mass flow rates (m_f), 20 g/s, 30 g/s, 40 g/s, and 60 g/s. The profiles at mass flow rate of 20 g/s were measured at six distances away from the wall (Z), 5 mm, 10 mm, 20 mm, 40 mm, 60 mm and 80 mm. It was found that at distances close to the wall (5 mm, 10 mm, and 20 mm), the individual jets from the pores can clearly be seen. At a distance of 40 mm, the probe is still in the mixing layer region (shear layer), where the velocities are still fluctuating a little. The velocities become smooth at distances of 60 mm and 80 mm away from the porous wall. Furthermore, it can be seen that at different mass flow rates, the profiles are similar for the two porous walls (15% and 20%). However, that is not quite the same with porous wall 37%. Also, it was found that with porous walls 15% and 20%, most of the flow exits before the end of the channel, which is due to high pressure build up caused by the high resistive property of the porous walls.

The present work, contributed to the investigation of the pressure distribution along the channel, and the effect of different mass flow rates and porosities has on the distribution. Furthermore, lower porosities (15%, 20%, and 37%) were used to fill in the gap in the literature, as its effect on the flow field in the particulate filter system was rarely investigated. Also, the scaled up test rig configuration, provides access to investigate the velocities exiting the porous wall of the single channel. Such results would be beneficial for many scholars, to compare and further develop the approach.

For future work, it would be beneficial to perform PIV measurements and compare the results with the present experiment. Also, perform further investigation with higher porosity levels. It would also be useful to perform numerical studies with many turbulence models, and assess their predicting capability.

5.1 Future work

Future implementations can be made for further investigations and development, these are summarized as the following:

1. The test section can be made out of a transparent material (for example: perspex or glass). Therefore, it would be beneficial to perform PIV measurements and compare the results with the present experiment.

2. The test rig allows to test different porous wall geometries. Therefore, it is possible to provide further investigations with higher porosity walls.

3. It would also be useful to perform numerical studies with many turbulence models, and assess their predicting capability. The 1-D model introduced by Konstandopolous et al. [14] can be used for comparison with the present work.

4. The scaled up rig can be used for other important studies. Such studies can include the implementation of multiple channels and investigate the contraction and expansion losses.

Chapter 6

Appendices

6.1 Appendix A

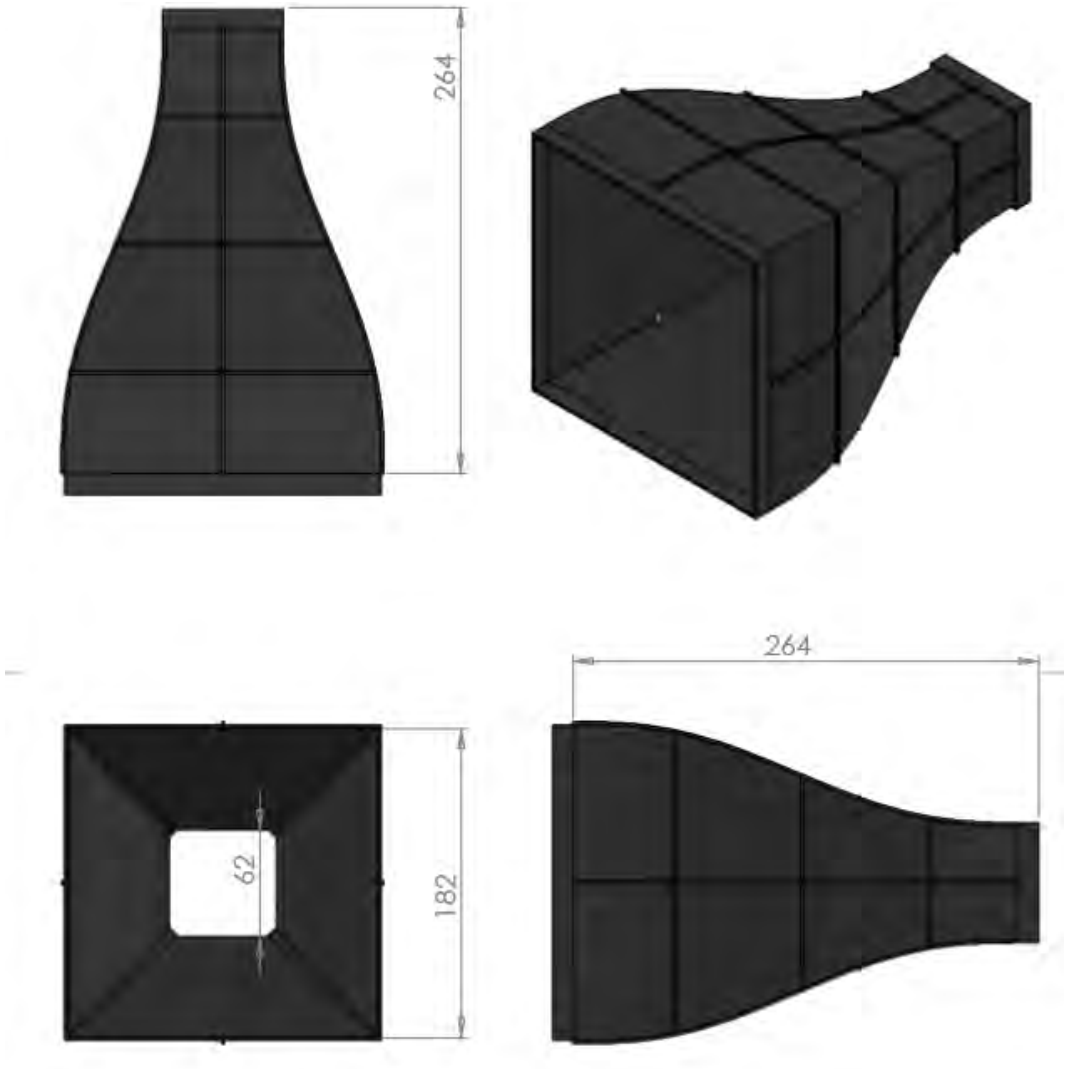

Figure 6.1: Contraction nozzle design

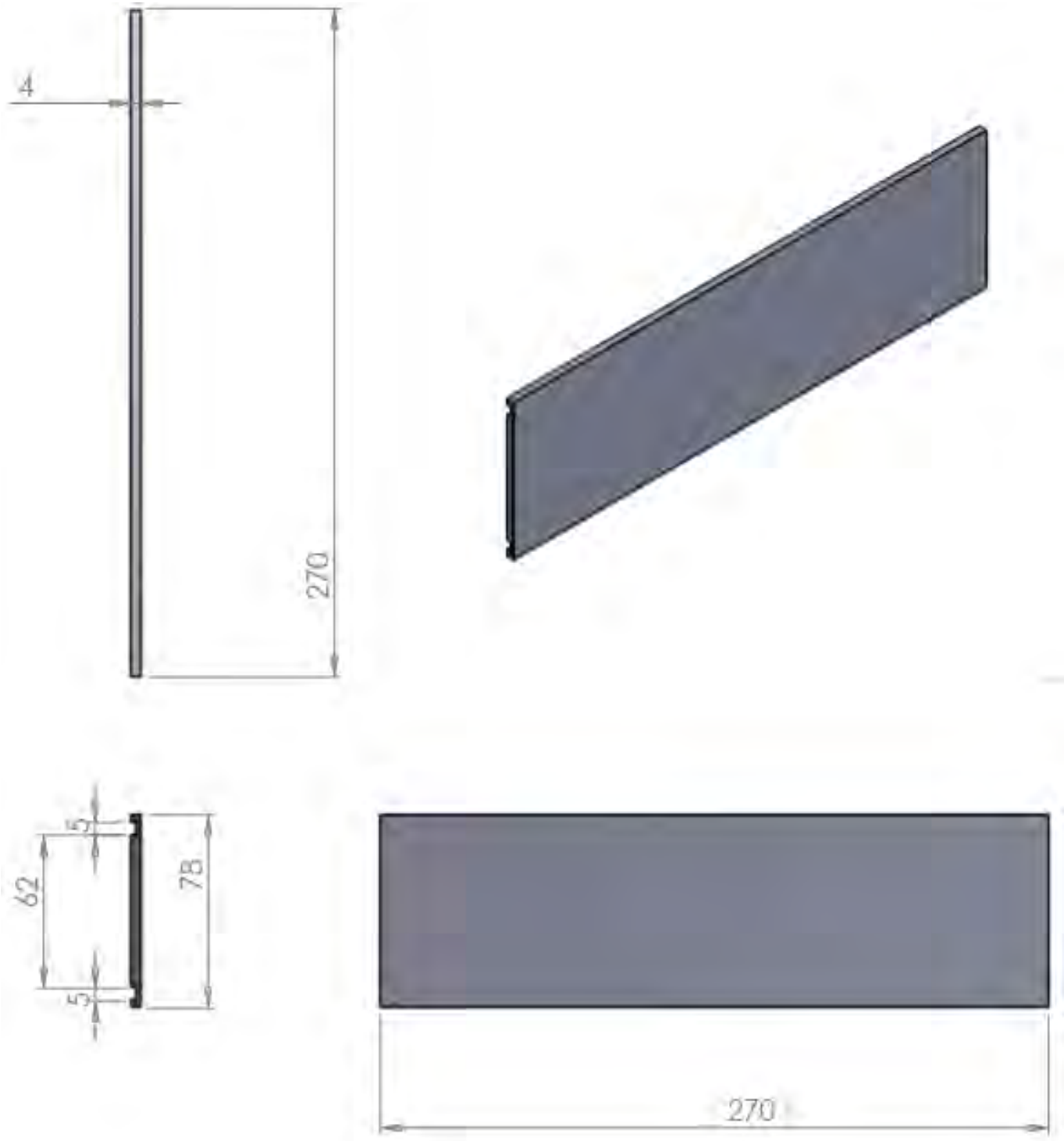

Figure 6.2: Aluminium plate design

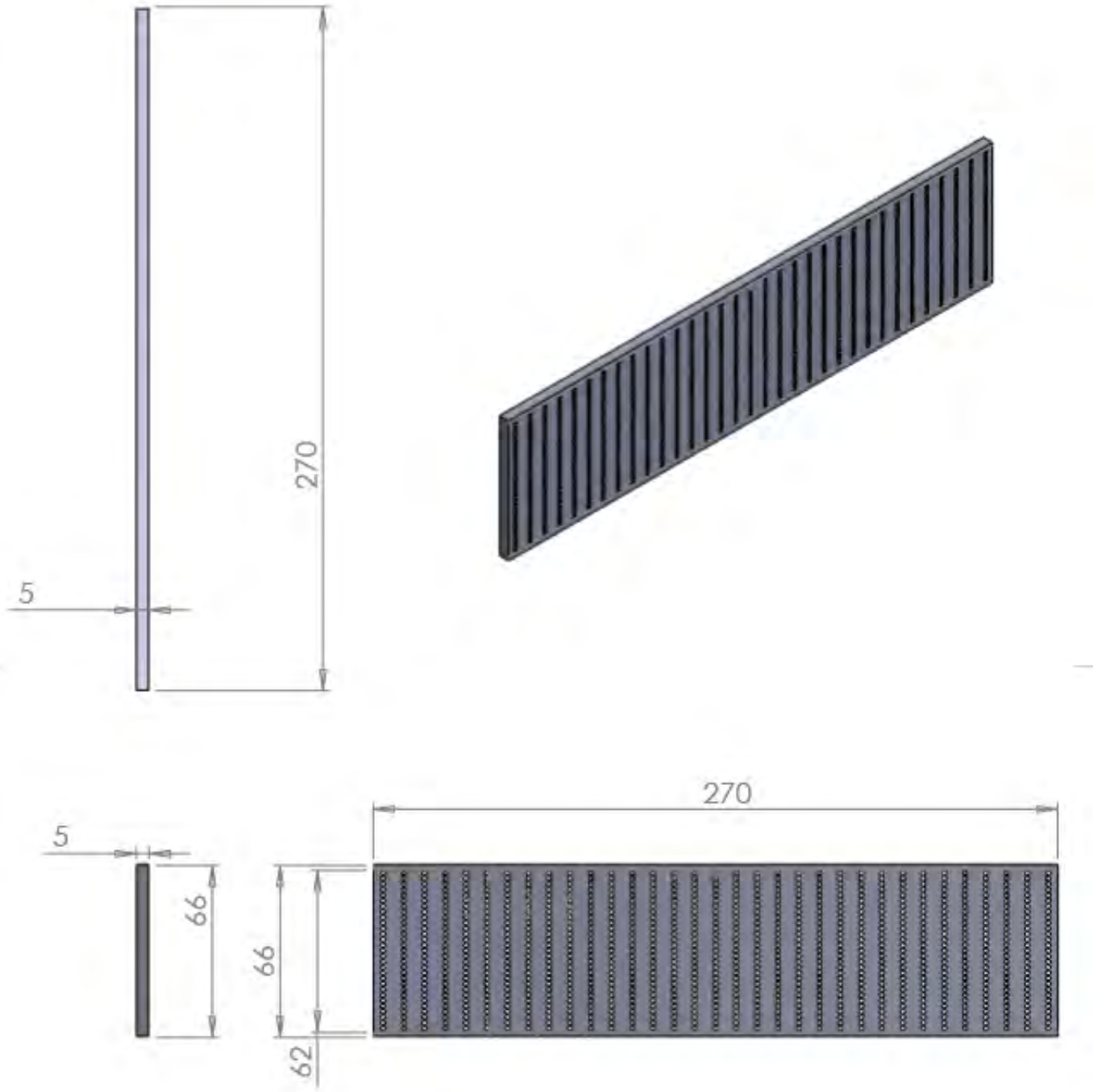

Figure 6.3: Porous wall design, showing the 15%

6.2 Appendix B

Some materials have been removed due to 3rd party copyright. The unabridged version can be viewed in Lancester Library - Coventry University.

Figure 6.4

Some materials have been removed due to 3rd party copyright. The unabridged version can be viewed in Lancester Library - Coventry University.

Figure 6.5

6.3 Appendix C

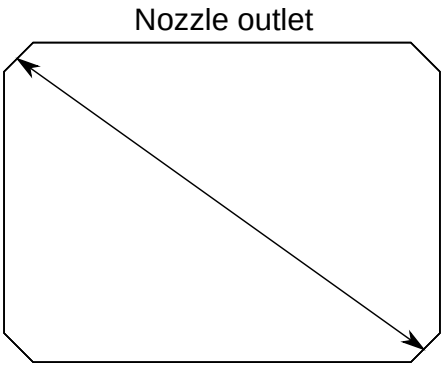

Figure 6.6: Measurement orientation

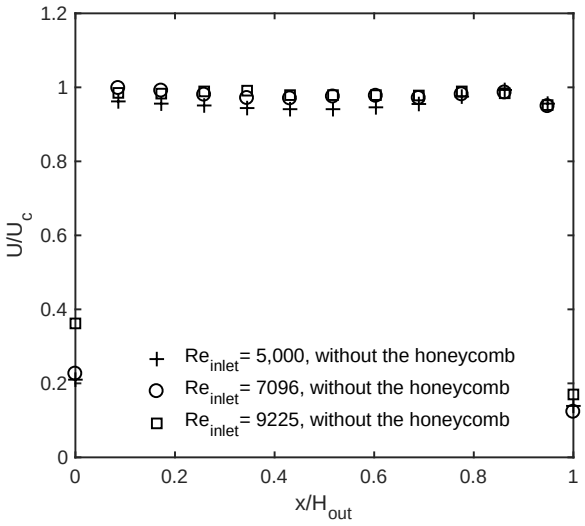

Figure 6.7: Non-dimensional velocity profiles, without the honeycomb

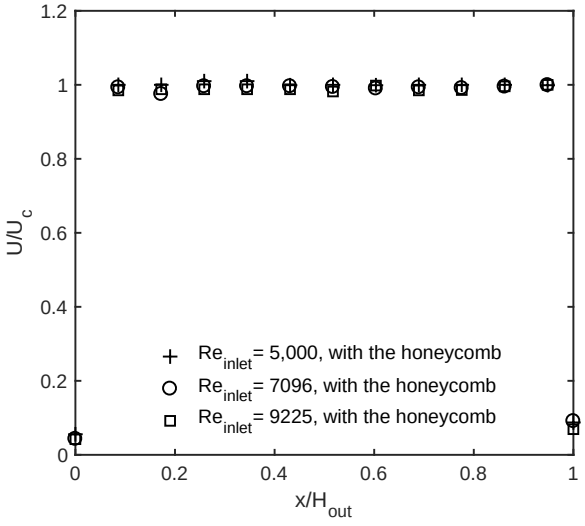

Figure 6.8: Non-dimensional velocity profiles, with the honeycomb

6.4 Appendix D

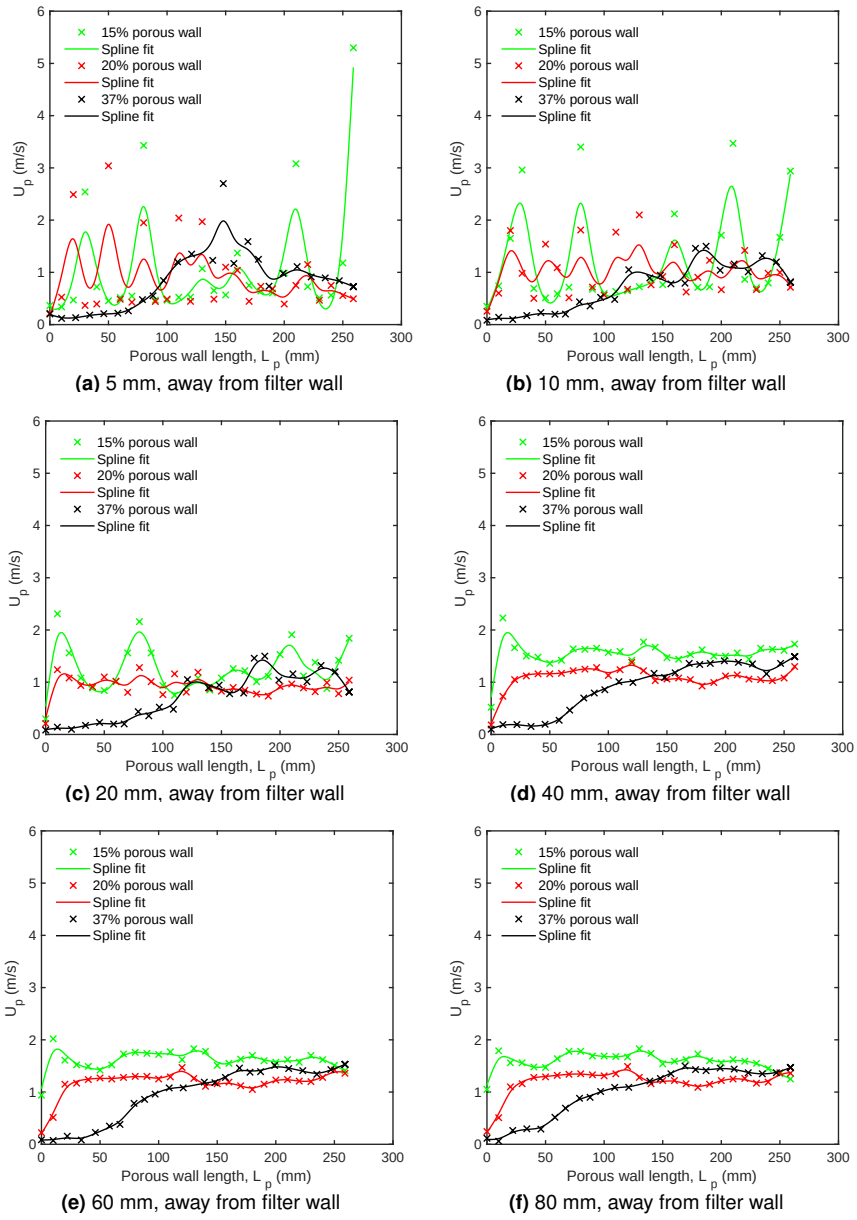

(a) 5 mm, away from filter wall

(b) 10 mm, away from filter wall

(c) 20 mm, away from filter wall

(d) 40 mm, away from filter wall

(e) 60 mm, away from filter wall

(f) 80 mm, away from filter wall

Figure 6.9: Velocity profiles across the porous wall, at $m_f = 20\,g/s$

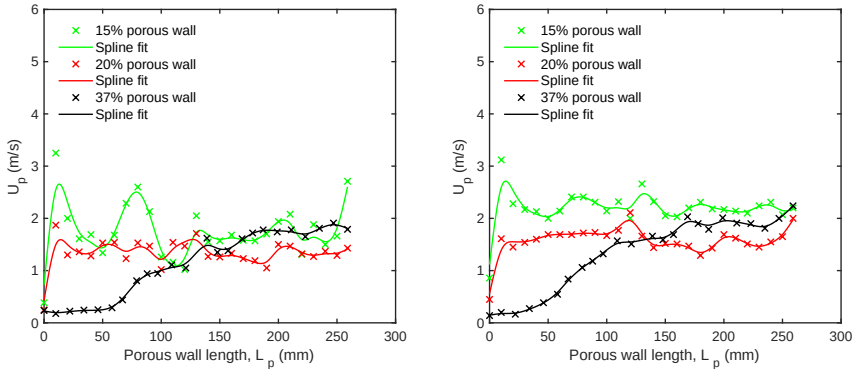

(a) 20 mm, away from filter wall

(b) 40 mm, away from filter wall

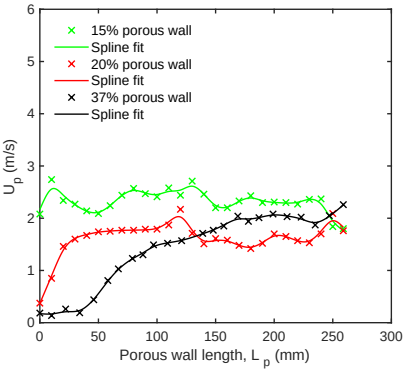

(c) 60 mm, away from filter wall

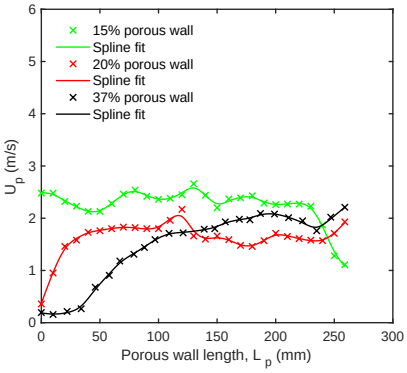

(d) 80 mm, away from filter wall

Figure 6.10: Velocity profiles across the porous wall, at $m_f = 30\,g/s$

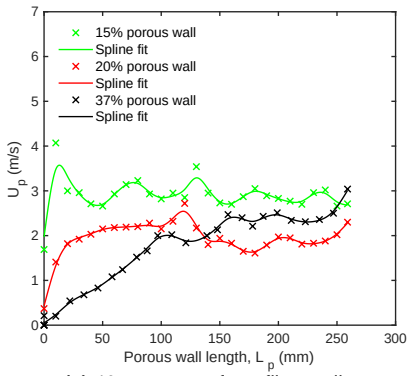

(a) 40 mm, away from filter wall

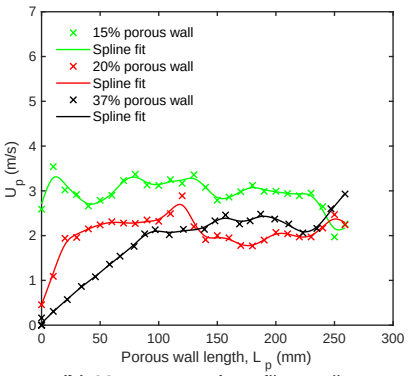

(b) 60 mm, away from filter wall

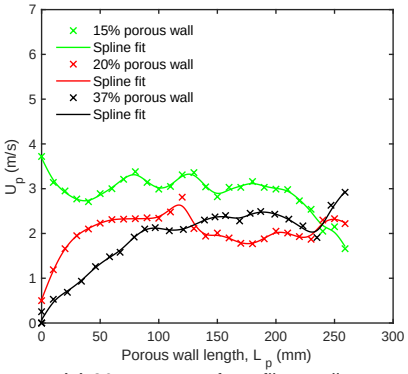

(c) 80 mm, away from filter wall

Figure 6.11: Velocity profiles across the porous wall, at $m_f = 40\,g/s$

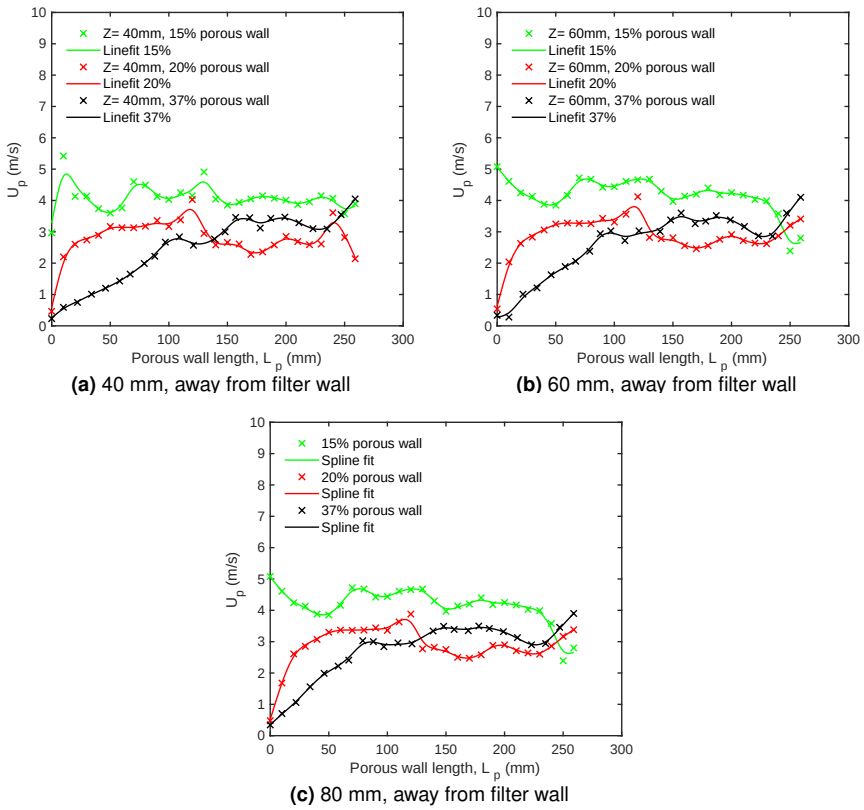

(a) 40 mm, away from filter wall

(b) 60 mm, away from filter wall

(c) 80 mm, away from filter wall

Figure 6.12: Velocity profiles across the porous wall, at $m_f = 60\,g/s$

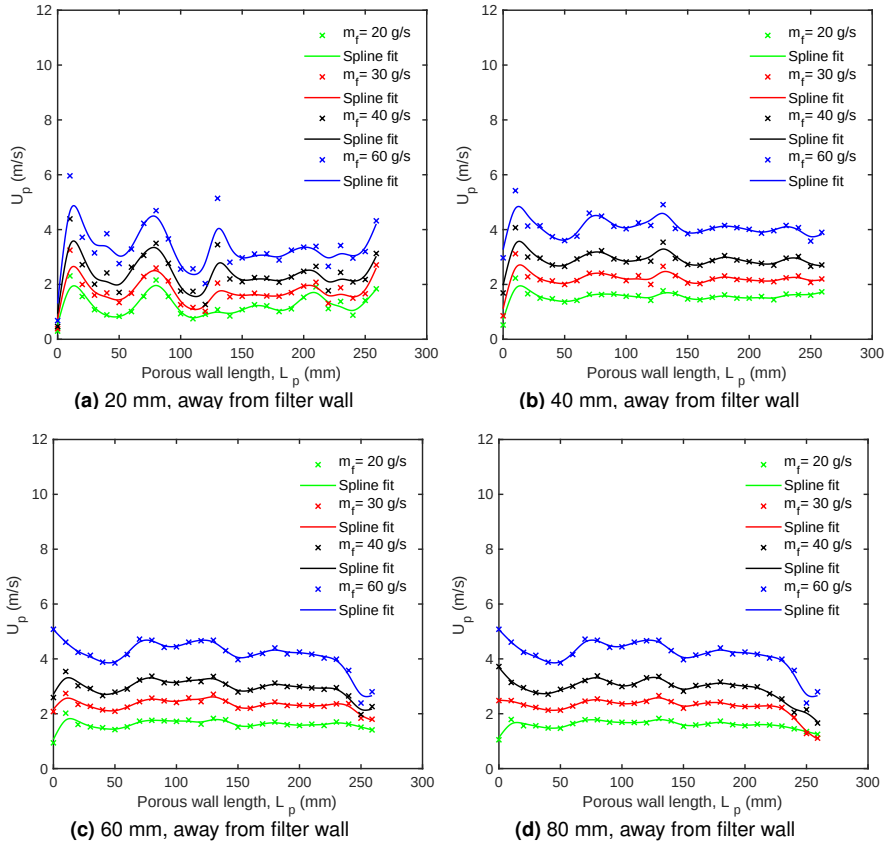

(a) 20 mm, away from filter wall

(b) 40 mm, away from filter wall

(c) 60 mm, away from filter wall

(d) 80 mm, away from filter wall

Figure 6.13: Velocity profiles of 15% porous filter at different mass flow rates (m_f)

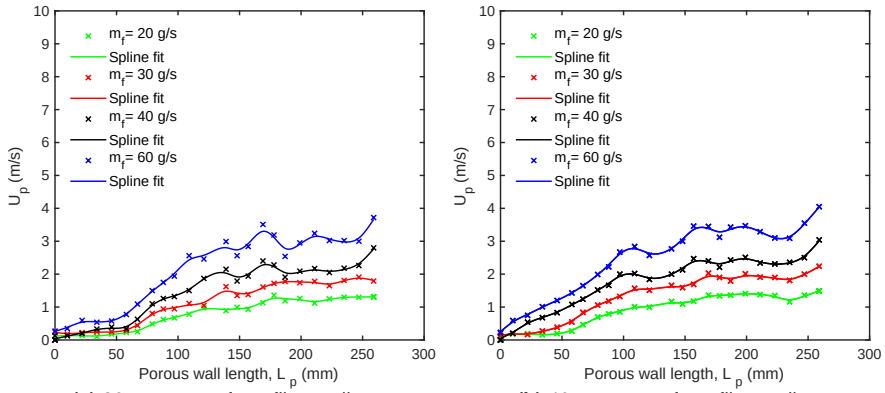

(a) 20 mm, away from filter wall **(b)** 40 mm, away from filter wall

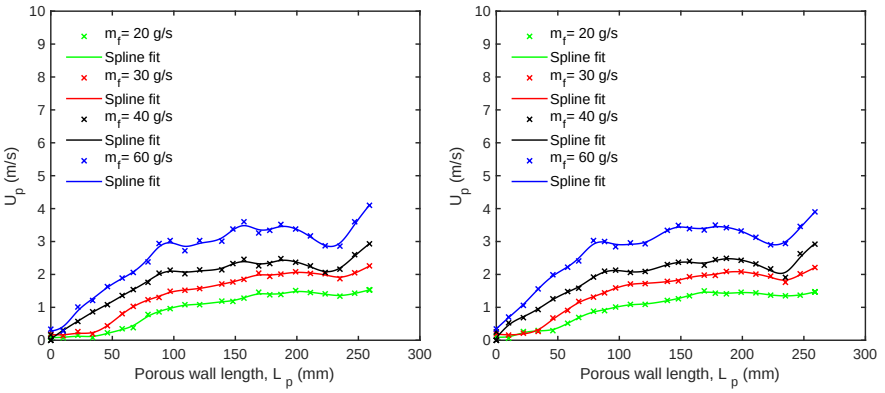

(c) 60 mm, away from filter wall **(d)** 80 mm, away from filter wall

Figure 6.14: Velocity profiles of 37% porous filter at different mass flow rates (m_f)

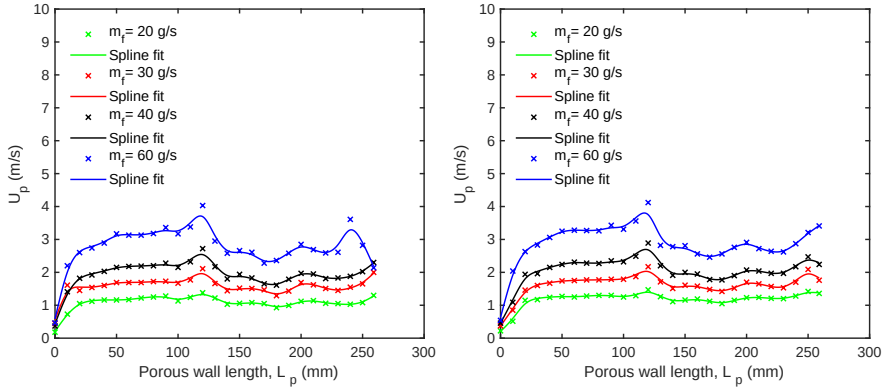

(a) 40 mm, away from filter wall **(b)** 60 mm, away from filter wall

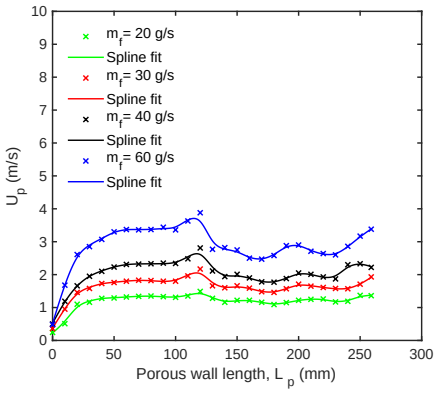

(c) 80 mm, away from filter wall

Figure 6.15: Velocity profiles of 20% porous filter at different mass flow rates (m_f)

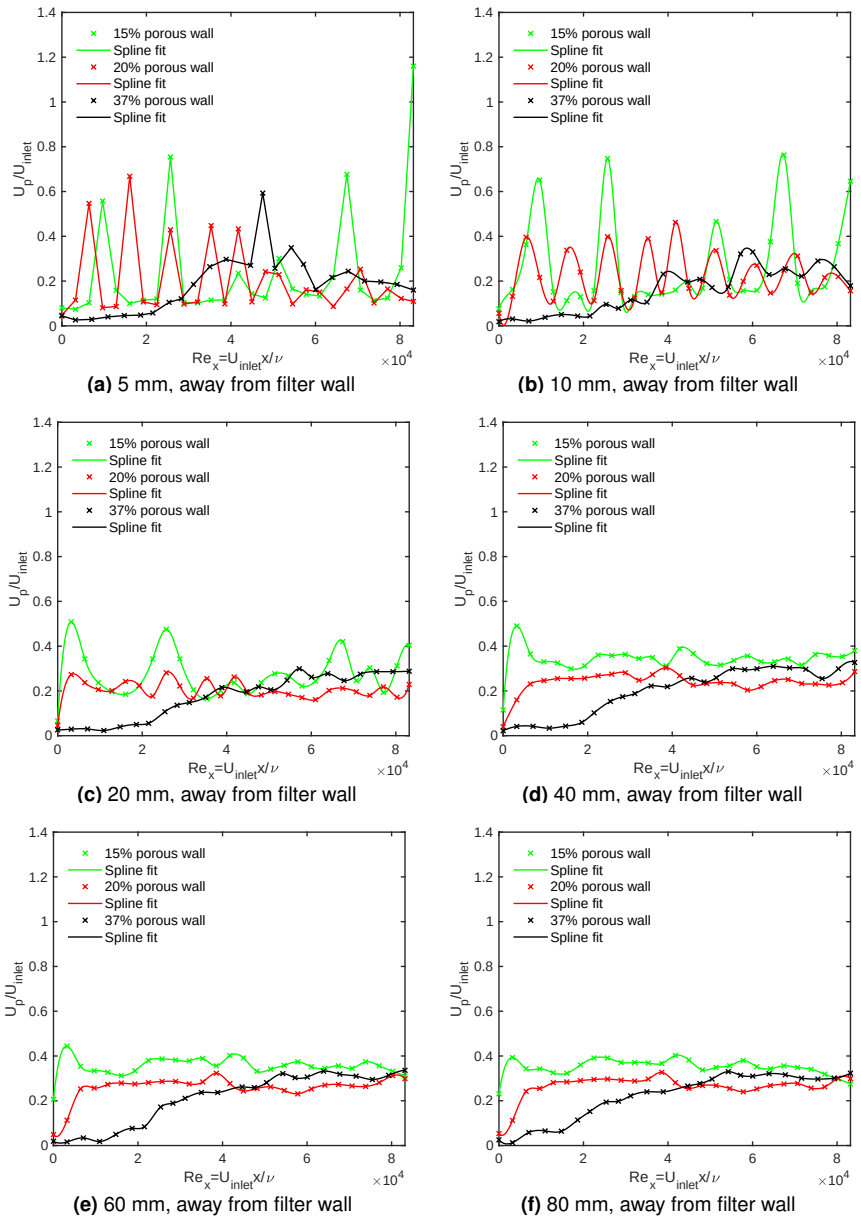

(a) 5 mm, away from filter wall

(b) 10 mm, away from filter wall

(c) 20 mm, away from filter wall

(d) 40 mm, away from filter wall

(e) 60 mm, away from filter wall

(f) 80 mm, away from filter wall

Figure 6.16: Reynold number distribution along the channel with 15% 20% *and* 37% porous filter, at $m_f = 20\,g/s$

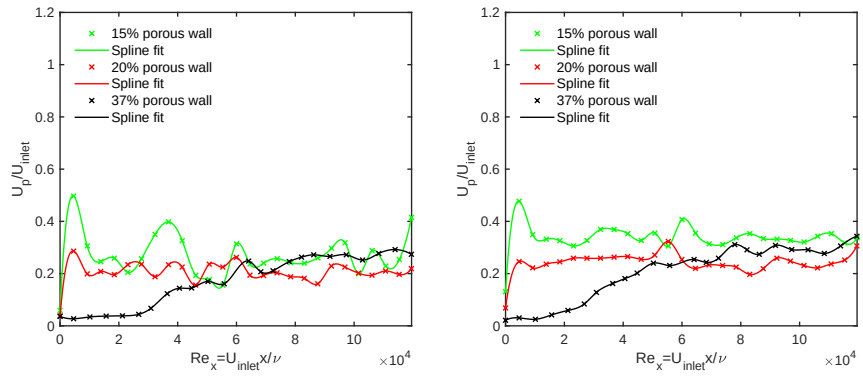

(a) 20 mm, away from filter wall

(b) 40 mm, away from filter wall

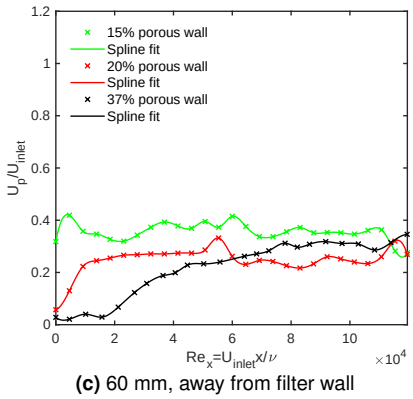

(c) 60 mm, away from filter wall

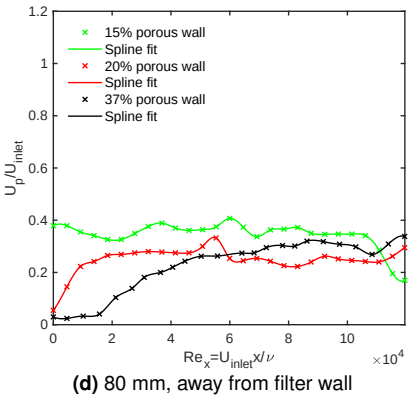

(d) 80 mm, away from filter wall

Figure 6.17: Reynold number distribution along the channel with 15% 20% *and* 37% porous filter, at $m_f = 30\,g/s$

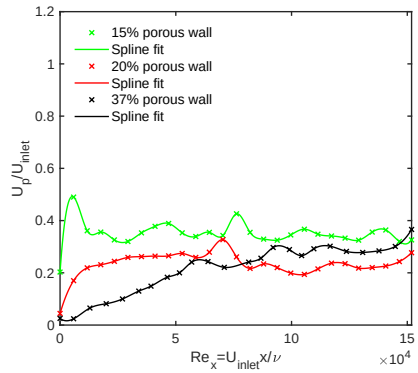

(a) 40 mm, away from filter wall

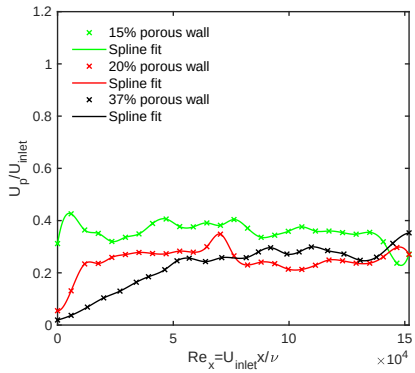

(b) 60 mm, away from filter wall

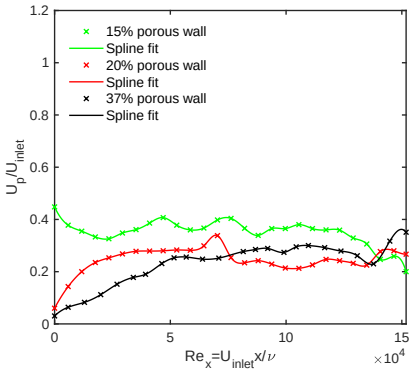

(c) 80 mm, away from filter wall

Figure 6.18: Reynold number distribution along the channel with 15% 20% *and* 37% porous filter, at $m_f = 40\,g/s$

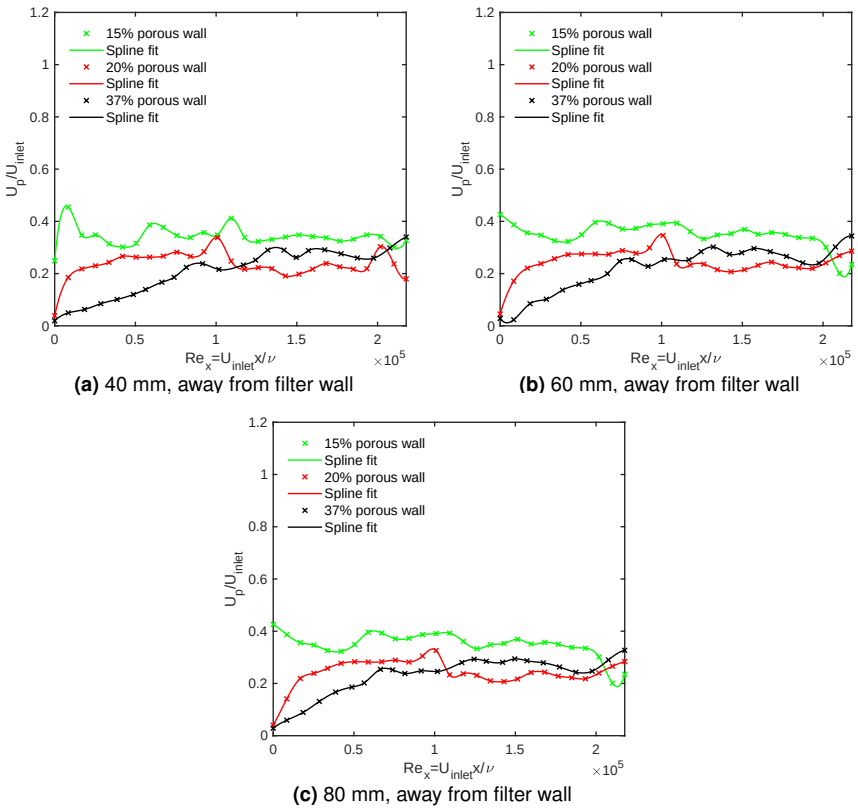

(a) 40 mm, away from filter wall

(b) 60 mm, away from filter wall

(c) 80 mm, away from filter wall

Figure 6.19: Reynold number distribution along the channel with 15% 20% *and* 37% porous filter, at $m_f = 60\,g/s$

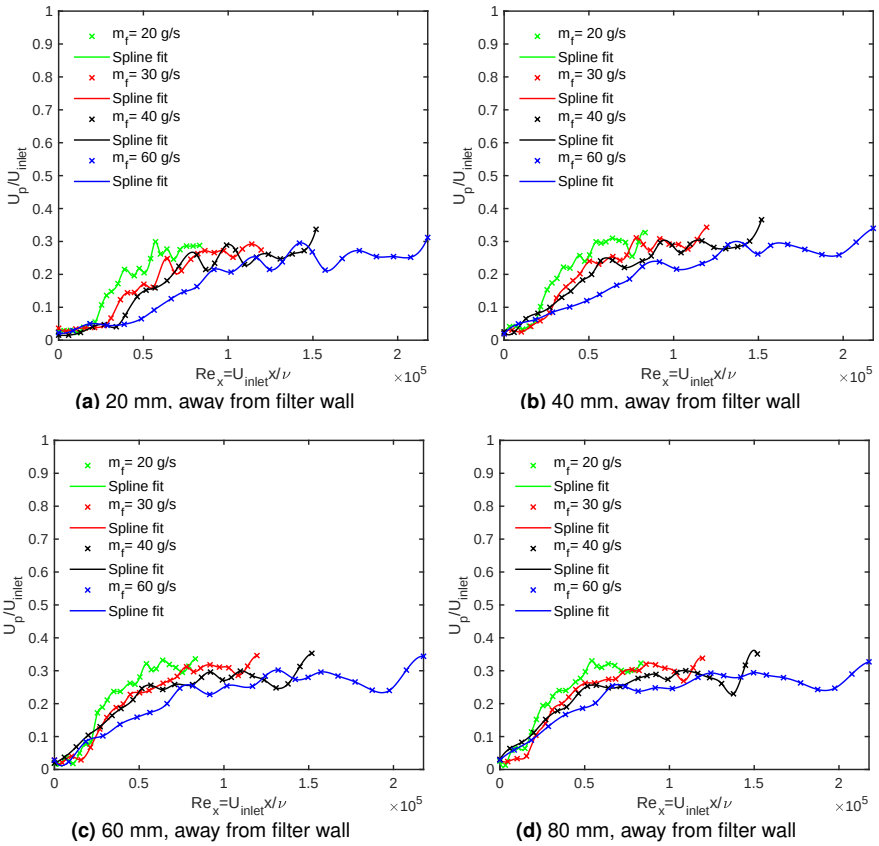

(a) 20 mm, away from filter wall

(b) 40 mm, away from filter wall

(c) 60 mm, away from filter wall

(d) 80 mm, away from filter wall

Figure 6.20: Reynold number distribution along the channel with 37% porous filter at different mass flow rates (m_f)

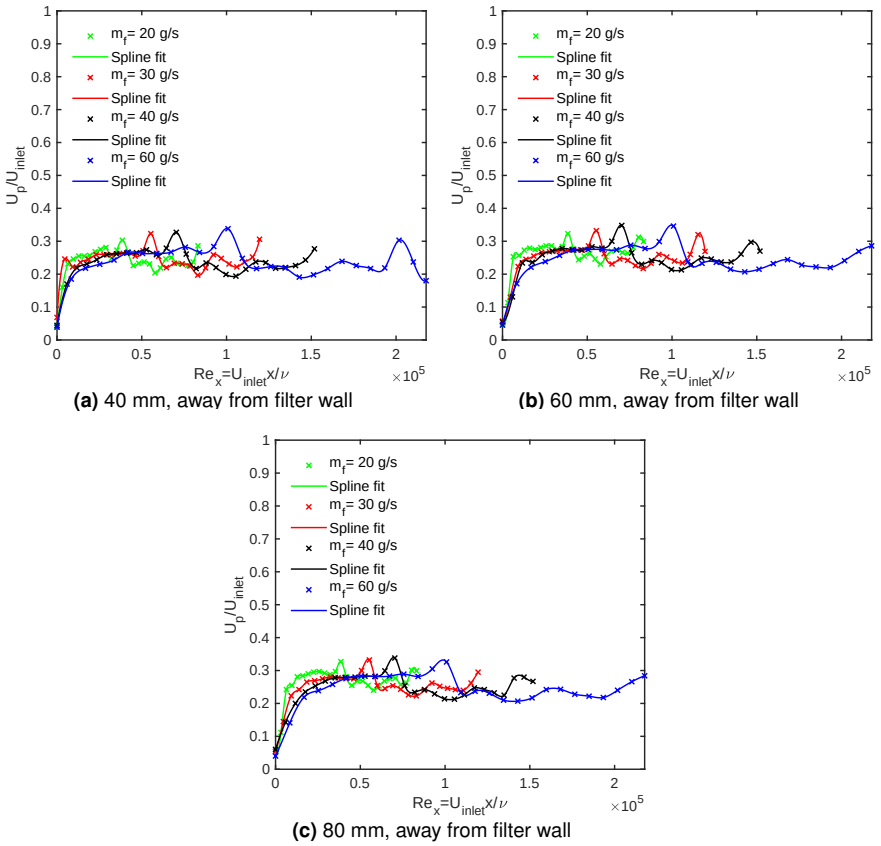

(a) 40 mm, away from filter wall

(b) 60 mm, away from filter wall

(c) 80 mm, away from filter wall

Figure 6.21: Reynold number distribution along the channel with 20% porous filter at different mass flow rates (m_f)

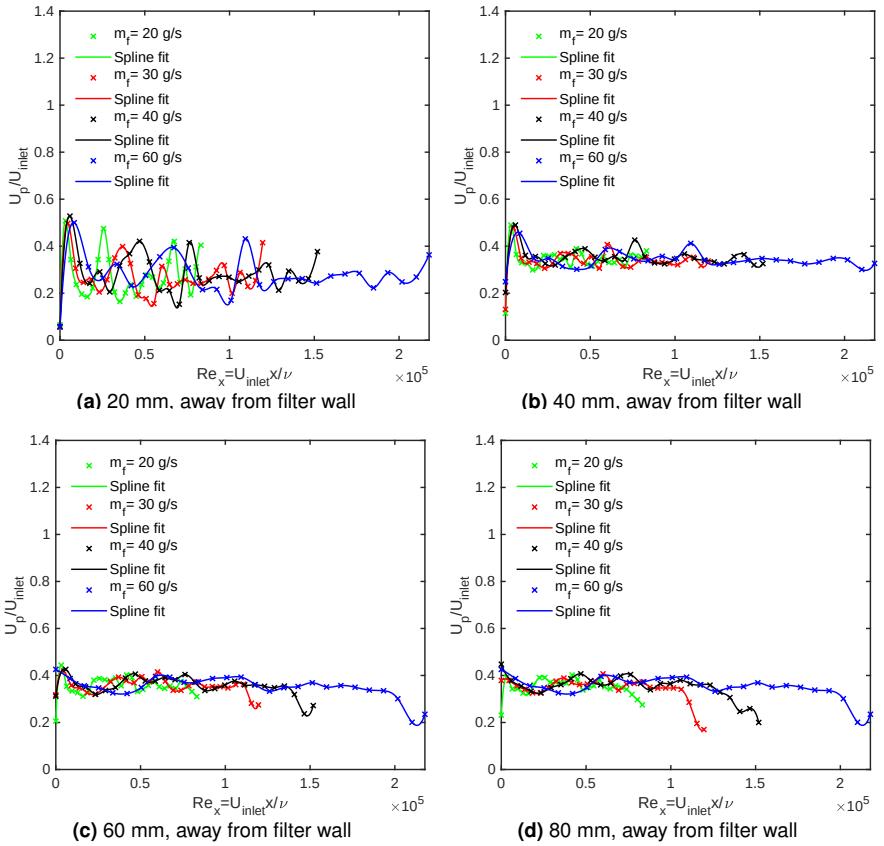

(a) 20 mm, away from filter wall

(b) 40 mm, away from filter wall

(c) 60 mm, away from filter wall

(d) 80 mm, away from filter wall

Figure 6.22: Reynold number distribution along the channel with 15% porous filter at different mass flow rates (m_f)

6.5 Appendix E

As it can be seen in Figure 6.23, the *entrance region* is where the inviscid flow from the upstream converges into the tube. The viscous boundary layers start growing downstream, slowing the axial flow ($u(r, x)$) at the wall, and therefore the centre-core accelerates to maintain the incompressible continuity obligation;

$$Q = \int u\, dA = constant \tag{6.1}$$

Where Q is the volume flow rate, u flow velocity and A is the cross-sectional area. At a certain distance from the entrance (L_e), the boundary layers merge, and the inviscid core vanishes. At $x = L_e$ the axial velocity no longer changes with x, and thereby the flow is said to be *fully developed*, $u \approx u(r)$. The velocity profile, and wall shear are constant downstream $x = L_e$, whereby the pressure drops linearly with x. These characteristics are for either laminar or turbulent flow.

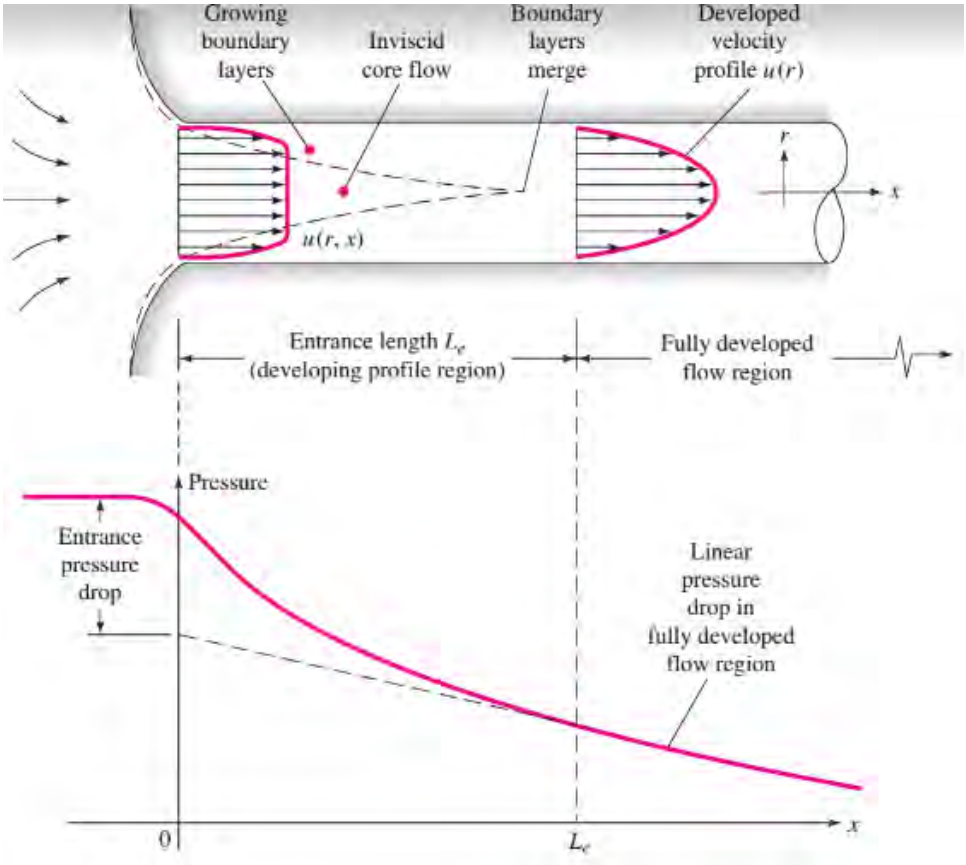

Figure 6.23: Velocity profiles development and pressure changes at the entrance of the duct [9]

Dimensional analysis indicates that the only parameter affecting the entrance length (L_e), is Reynolds number (Re). Therefore, if ;

$$L_e = f(d,\ V,\ \rho,\ \mu) \quad V = \frac{Q}{A} \tag{6.2}$$

Then;

$$\frac{L_e}{d} = g\left(\frac{\rho V d}{\mu}\right) = g(Re) \tag{6.3}$$

Schlichting et al [65] and Frank et al. [9] states that for laminar flow, the accepted correlation is;

$$\frac{L_e}{d} \approx 0.06 Re \tag{6.4}$$

Furthermore, the longest development length possible is at $Re_c = 2300$ (where Re_c is the critical Reynolds number), where the maximum laminar entrance length is $L_e = 138d$. However when the flow is turbulent, the boundary layers grow quickly, and hence the entrance length is shorter, according to the approximation of smooth walls [9, 65];

$$\frac{L_e}{d} = 4.4(Re)^{1/6} \tag{6.5}$$

6.5.0.1 Flow through a circular and non-circular duct

When applying formulas into a practical case, it is empirical to use control volume analysis. Taking a classical problem that includes the flow in a full pipe (as shown in Figure 6.24). Considering incompressible steady flow between section 1 and 2, of an inclined pipe with constant cross-sectional area A. The continuity equation ends up to be;

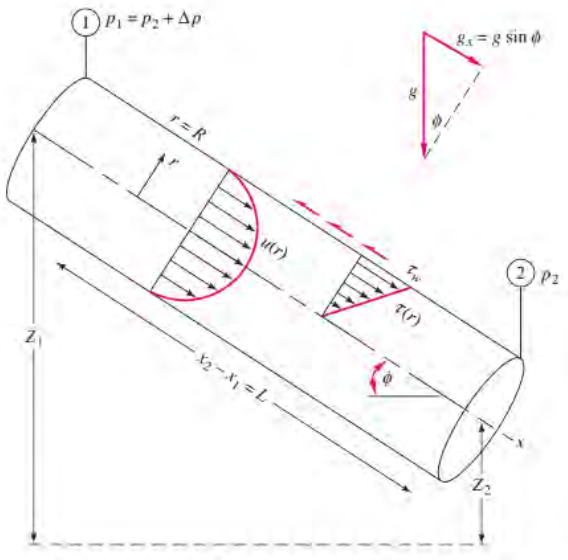

Figure 6.24: Control volume schematic of steady fully developed pipe flow [9]

$$Q_1 = Q_2 = constant \tag{6.6}$$

where Q is the volume flow rate. The volume flow rate is $Q = VA$ (V is the fluids velocity and A is the cross-sectional area). Since the pipe is of a constant area A, hence;

$$V_1 = \frac{Q_1}{A_1} = V_2 = \frac{Q_2}{A_2} \rightarrow V_1 = V_2 = V \tag{6.7}$$

Since there are no shaft-work(pump, turbine for example) or heat-transfer effects, the steady-flow energy equation reduces to;

$$\frac{P_1}{\rho g} + 0.5\frac{V_1^2}{g} + z_1 = \frac{P_2}{\rho g} + 0.5\frac{V_2^2}{g} + z_2 + h_f \tag{6.8}$$

Assuming that the flow is fully developed, then the velocity profiles through the pipe are constant, therefore equation 6.8 reduces to;

$$h_f = \Delta z + \frac{\Delta P}{\rho g} \tag{6.9}$$

The pipe head loss h_f equals to the change of pressure. Conservation of momentum states that all forces acting on the fluid entering and leaving the system are equal. By applying control volume theorem, the general conservation momentum equation ends up to be;

$$\sum F = \frac{d}{dt}\Big(\int_{CV} V\rho\, dV\Big) + \sum(m_f V)_{outlet} - \sum(m_f V)_{inlet} \tag{6.10}$$

Applying all the forces accounting due to pressure, gravity and shear in Figure 6.24 into equation 6.10;

$$\Delta P\pi R^2 + \rho g(\pi R^2)\Delta L sin\phi - \tau_w(2\pi R)\Delta L = m_f(V_1 - V_2) = 0 \tag{6.11}$$

As it can be seen, h_f can be related to shear stress;

$$\Delta z + \frac{\Delta P}{\rho g} = h_f = \frac{2\tau_w}{\rho g}\frac{\Delta L}{R} \tag{6.12}$$

Schlichting et al. [65] and Frank et al. [9] denoted that the shear wall stress τ_w is a function of the fluid flow density ρ, velocity V, dynamic viscosity μ, and the pipe's diameter d and wall-roughness ϵ_w;

$$\tau_w = F(\rho,\ V,\ \mu,\ d,\ \epsilon_w) \tag{6.13}$$

Thereby, the dimensional analysis results in the following relation;

$$\frac{8\tau_w}{\rho V^2} = f = F\Big(Re, \frac{\epsilon_w}{d}\Big) \tag{6.14}$$

f is an important parameter in determining the pressure loss in a pipe, it is known as the Darcy friction factor. It is a better approach in determining the pipe's head loss h_f by combining equa-

tions 6.12 and6.14;

$$h_f = f\frac{L}{d}\frac{V^2}{2g} \tag{6.15}$$

Equation 6.15 is known as Darcy-Weisbach equation. Schlichting [65] and Frank et al. [9] highlighted, that equation 6.15 is valid for duct flows of any cross-section, and for flows that are laminar and turbulent. However, the friction factor f is determined differently for laminar and turbulent flows.

For laminar case an exact theory for laminar Darcy friction factor, in a circular pipe is;

$$f_{laminar} = \frac{64}{Re} \tag{6.16}$$

The laminar head loss $h_{f,laminar}$ is proportional to the fluids velocity V, as this can be seen by equating equation 6.16 into equation 6.15;

$$h_{f,laminar} = \frac{64}{Re}\frac{L}{d}\frac{V^2}{2g} = \frac{64\mu}{\rho V d}\frac{L}{d}\frac{V^2}{2g} = \frac{32\mu LV}{\rho d^2 g} \tag{6.17}$$

However, for the turbulent case it is quite different. Prandtl derived an equation in 1935 for turbulent flow through a smooth-walled pipe, then adjusted it to fit the friction data;

$$\begin{aligned} \frac{1}{\sqrt{f}} &\approx 1.99 log(Re\sqrt{f}) - 1.02 \\ \frac{1}{\sqrt{f}} &= 2log(Re\sqrt{f}) - 0.8 \end{aligned} \tag{6.18}$$

There are various approximations in the literature [9, 65, 66] to determine f explicitly from Re;

$$f_{turbulent,\ fully\ smooth\ wall} = \begin{cases} 0.316Re^{-1/4} & 4000 < Re < 10^5 \\ \left(1.8log\frac{Re}{6.9}\right)^{-2} \end{cases} \tag{6.19}$$

Turbulent flow through a rough wall pipe, takes a different measure when determining f, as the wall-roughness ϵ_w plays a role. Colebrook [66] presented an equation using a clever interpolation, to come with the following relation;

$$\frac{1}{\sqrt{f_{turbulent}}} = -2.0\ log\left(\frac{\epsilon_w/d}{3.7} + \frac{2.51}{Re\sqrt{f_{turbulent}}}\right) \tag{6.20}$$

This is an accepted design formula for turbulent friction (Equation 6.20). Furthermore, Haaland [67] developed an alternative approach in determining $f_{turbulent}$ when Re is known. An alternative

explicit formula given by Haaland [67] which varies from Equation 6.20 by 2%;

$$\frac{1}{\sqrt{f_{turbulent}}} \approx -1.8\, log\left(\left(\frac{\epsilon_w/d}{3.7}\right)^{1.11} + \frac{6.9}{Re}\right) \tag{6.21}$$

Moody [10] developed a chart (Figure 6.25)which is probably the most famous and useful figure in Fluid mechanics, and accurate to $\pm$15% for design calculations over the full range. The chart can be used for circular and non-circular duct flow. The shaded area shown in Figure 6.25 is where the transition state occur, and there are no reliable friction factors in that range ($2000 < Re < 4000$). Recommended roughness (ϵ_w) for commercial ducts are shown in Figure 6.26.

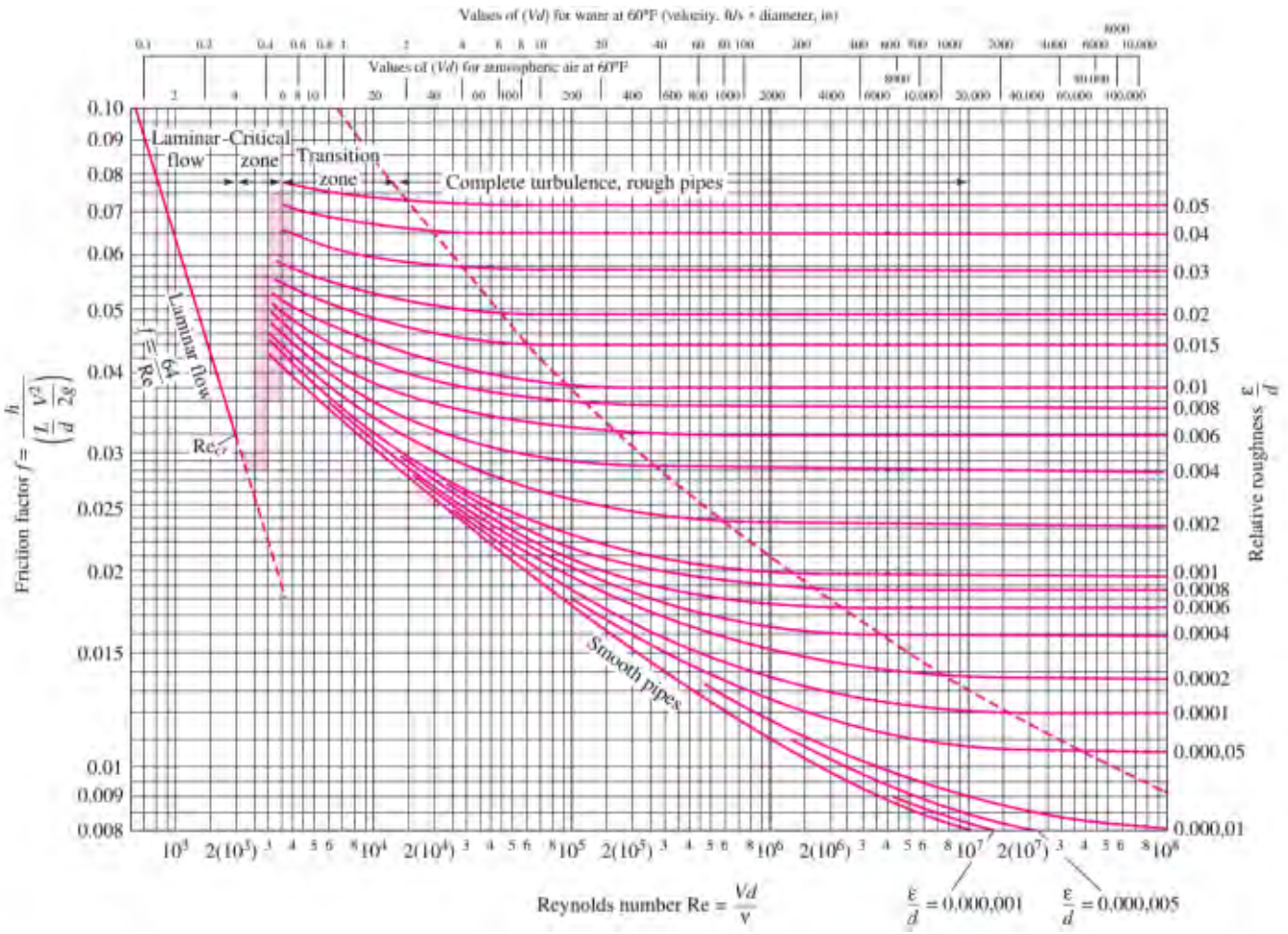

Figure 6.25: Moody chart for pipe friction in laminar, transition and turbulent flow with smooth and rough walls. [10]

		ϵ		
Material	Condition	ft	mm	Uncertainty, %
Steel	Sheet metal, new	0.00016	0.05	±60
	Stainless, new	0.000007	0.002	±50
	Commercial, new	0.00015	0.046	±30
	Riveted	0.01	3.0	±70
	Rusted	0.007	2.0	±50
Iron	Cast, new	0.00085	0.26	±50
	Wrought, new	0.00015	0.046	±20
	Galvanized, new	0.0005	0.15	±40
	Asphalted cast	0.0004	0.12	±50
Brass	Drawn, new	0.000007	0.002	±50
Plastic	Drawn tubing	0.000005	0.0015	±60
Glass	—	Smooth	Smooth	
Concrete	Smoothed	0.00013	0.04	±60
	Rough	0.007	2.0	±50
Rubber	Smoothed	0.000033	0.01	±60
Wood	Stave	0.0016	0.5	±40

Figure 6.26: From tests of commercial ducts, recommended values of average roughness ϵ_w. [9]

If the duct is non-circular, the analysis of fully developed flow follows that of the circular pipe but is more complicated algebraically. For laminar flow, the equations of continuity and momentum can be solved directly. However, when the flow is turbulent, the logarithm law velocity profile can be used, or simply the hydraulic diameter is an excellent approximation. For a non-circular duct, the cross-sectional area A does not equal πR^2 and the cross-sectional perimeter wetted by the shear stress is not equal to $2\pi R$ (following the schematic in Figure 6.23). Therefore the momentum equation 6.11 for non-circular duct flow refines to be;

$$\Delta PA + \rho g(A)\Delta L sin\phi - \tau_w(P_{perimeter})\Delta L = 0 \tag{6.22}$$

The hydraulic diameter is given in the following form;

$$D_h = \frac{4x\ Area}{WettedPerimeter} = 4R_h \tag{6.23}$$

Therefore, the equation 6.15 breaks down to be;

$$h_f = f\frac{L}{D_h}\frac{V^2}{2g} \tag{6.24}$$

6.6 Appendix F

6.6.0.1 Theory: Darcy-Forchheimer and Ergun Equation

Flow through porous medium is generally represented either by Darcy-Forchheimer regime or Ergun regime. The microstructure of the porous medium is characterized by its pore size (cell size), pore shape, and porosity ($\frac{Volume_{cell}}{Volume_{total}} x100$). A simple schematic of a case where airflow drives through a porous medium, shown below in Figure 6.27. Several assumptions are to be made:

- Flow is steady and fully developed.
- Porous medium is isotropic and homogeneous.
- Air is a perfect gas, and the flow condition is incompressible.
- Flow through the porous medium is isothermal ($\Delta T = 0$).

Ergun Equation Regime

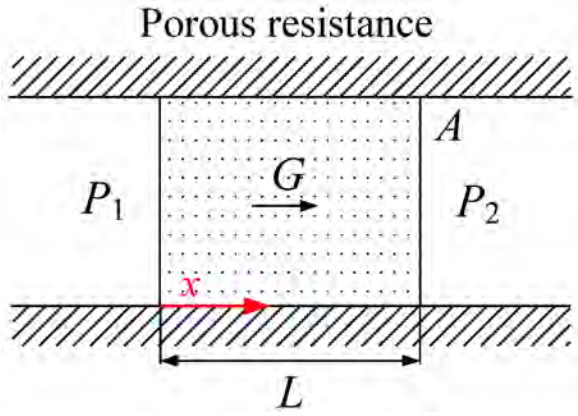

Figure 6.27: 1-D Schematic of airflow through porous medium

Mean flow velocity (V) changes with the air density (ρ) along the total length or cross-sectional area (A) of the filter/porous medium, and it is written in terms of mass flow rate (G) as follows [58];

$$V = \frac{G}{\rho A} \tag{6.25}$$

Assuming air is a perfect gas,

$$\rho = \frac{P}{RT} \tag{6.26}$$

Where P is the pressure, R is the gas constant, and T is the temperature.

Ergun [47] described an empirical relation of the pressure drop through the porous medium, based on two parameters, the porosity and geometrical length scale. The empirical relation is written as;

$$-\frac{dP}{dx} = \alpha\frac{(1-\epsilon_p)^2\mu}{\epsilon_p^3\varphi^2 D_{cell}^2}V + \beta\frac{(1-\epsilon_p)\rho}{\epsilon_p^3\varphi D_{cell}}V^2 \tag{6.27}$$

Where α is a factor for the viscous drag part of the pressure drop, β is the factor for the form drag portion, ϵ_p is the porosity and D_{cell} is the cell diameter. Furthermore, φ is a coefficient of sphericity, that is employed in the equation to correct the pressure losses. Dukhan *et al.* [59] experimentally describes that the Ergun relation was based on modelling the space between the packed beds of spheres as parallel microscopic tubes or capillaries. Where the first term of the equation accounts for the viscous effects and the other term for the kinetic effects. The multipliers α and β are considered to be as the correction factors that account for the geometrical differences between the flow trajectories through the packed spheres and parallel capillaries.

Substituting equations 6.25 and 6.26 into equation 6.27, to provide an Ergun equation, when the case is incompressible flow;

$$\rho\frac{\Delta P}{L} = \frac{\alpha(1-\epsilon_p)^2\mu}{\epsilon_p^3 A\varphi^2 D_{cell}^2}G + \frac{\beta(1-\epsilon_p)}{\epsilon_p^3\varphi D_{cell}A^2}G^2 \tag{6.28}$$

The Reynolds number based on porosity (Re_{ϵ_p}) and cell diameter D_{cell}, can be written in the following form;

$$Re_{\epsilon_p} = \frac{\rho V\varphi D_{cell}}{\mu(1-\epsilon_p)} \tag{6.29}$$

The dimensionless friction factor is defined as[47];

$$f_{\epsilon_p} = \frac{dP}{dx}\frac{\varphi D_{cell}}{\rho V^2}\left(\frac{\epsilon_p^3}{1-\epsilon_p}\right) \tag{6.30}$$

By substituting equations 6.29 and 6.30 into equation 6.27, will result in the following correlation

of the friction factor as a function of the Reynolds number based on porosity;

$$f_{\epsilon_p} = \frac{\alpha}{Re_{\epsilon_p}} + \beta \tag{6.31}$$

Traditionally the coefficients values of α and β are 150 and 1.75, respectively.

Darcy-Forchheimer Equation Regime

Based on previous work done by Konstandopoulos *et al.* [11–16] which were more numerical than experimental, validates that expressing the flow through porous medium by its pressure loss, can be very accurately described by summing up the individual pressure drop across the numerical domain or the experimental domain. A simple illustration can be shown in Figure 6.28;

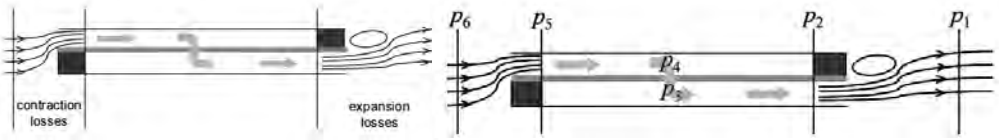

(a) Schematic view of the flow into a DPF [11–16] **(b)** Local individual pressure locations [11–16]

Figure 6.28: Diesel Particulate Filter (DPF) schematic view [11–16]

Each contribution of the pressure losses require the specification of one or more parameters. Starting with the thin porous wall, where the pressure drop is described by Darcy-Forchheimer Equation Regime, that is the sum of the Darcy term and Forchheimer term [11–14];

$$\Delta P_p = \frac{\mu}{k} V_p w_p + \beta_F \rho V_p^2 w_p \tag{6.32}$$

Two parameters in Equation 6.32, which are the Forchheimer coefficient β_F and Darcy permeability k, need to be specified to make estimations of the pressure drop (ΔP). The permeability dimensions denoted as the length squared and the square root of it refers to the pore level scale $\sqrt{k}$, which represents the characteristic of the porous medium. Whereas the Forchheimer coefficient dimensions is denoted as the inverse length, and β_F^{-1}, represents the length scale, which is the characteristic of the pore roughness. Both parameters depend on the pore size and the porosity of the porous medium, Konstandopoulos *et al.* [14] related the two parameters in the following form;

$$\beta_F = \frac{constant}{\epsilon_p^{1.5}\sqrt{k}} \tag{6.33}$$

From Ergun's correlation [68], the constant value in Equation 6.33 is 0.143. However, based on new compilation, it can also be 0.134 and 0.298, for smooth and rough cells of packed beds, respectively. Based on known structural characterization of the available porous medium [11–14], it has been noted that the Forchheimer term in equation 6.32 (third term), can be considered negligible when;

- Porosity is in the order of 50%.
- Pore size in the range of $10 - 30\mu m$

However, this can not be the case if the porosity is significantly higher than extruded wall-flow filters and when the operating condition is at high flow rates. Such cases can be referenced as fibrous textile or foam structured filters.

Further pressure drop occurs in the porous medium, would be due to the frictional losses of the flow along the square channel. This type of pressure loss is linear dependence on the velocity through the channel for laminar flow. It can be written as;

$$\Delta P_{channel\ friction} = \frac{\mu VL}{a^2} 2C_f Re\xi \tag{6.34}$$

Where $C_f Re$ of a cross-sectional square section has a constant value of 14.227, when the flow is fully developed laminar. The factor ξ is a correction factor that accounts for the effect of suction or injection on the term $C_f Re$. For typical applications, ξ can be taken as 1 since the velocity at the wall are small enough to keep the Reynolds number at the wall less than 2.

Finally the last contribution of the pressure drop in Figure 6.28 , would be the inertial losses caused by the contraction and expansion of the flow as it enters and exists the channels. This component increases with the inlet axial velocity squared, and can be denoted as;

$$\Delta P_{contraction\ and\ expansion} = \zeta \frac{\rho V^2}{2} \tag{6.35}$$

Where, ζ is known as the contraction/expansion coefficient, that depends on the filter frictional open cross-sectional flow area and Reynolds number [14].

References

[1] John Kim, Parviz Moin, and Robert Moser. Turbulence statistics in fully developed channel flow at low reynolds number. *Journal of fluid mechanics*, 177:133–166, 1987.

[2] JGM Eggels, F Unger, MH Weiss, J Westerweel, RJ Adrian, R Friedrich, and FTM Nieuwstadt. Fully developed turbulent pipe flow: a comparison between direct numerical simulation and experiment. *Journal of Fluid Mechanics*, 268:175–210, 1994.

[3] K Suga, Y Matsumura, Y Ashitaka, S Tominaga, and M Kaneda. Effects of wall permeability on turbulence. *International Journal of Heat and Fluid Flow*, 31(6):974–984, 2010.

[4] WP Breugem, BJ Boersma, and RE Uittenbogaard. The influence of wall permeability on turbulent channel flow. *Journal of Fluid Mechanics*, 562:35–72, 2006.

[5] Athanasios G Konstandopoulos. Flow resistance descriptors for diesel particulate filters: definitions, measurements and testing. Technical report, SAE Technical Paper, 2003.

[6] James H Bell and Rabindra D Mehta. Contraction design for small low-speed wind tunnels. 1988.

[7] Rabindra D Mehta and Peter Bradshaw. Design rules for small low speed wind tunnels. *The Aeronautical Journal (1968)*, 83(827):443–453, 1979.

[8] Mansour Masoudi. Pressure drop of segmented diesel particulate filters. Technical report, SAE Technical Paper, 2005.

[9] Frank White. Viscous fluid flow. mcgraw-hill series in mechanical engineering. 2006.

[10] L. F. Moody. Friction factors for pipe flows. *ASME Trans.*, 66:671–684, 1944.

[11] Athanasios G Konstandopoulos and John H Johnson. Wall-flow diesel particulate filter-sâĂŤtheir pressure drop and collection efficiency. Technical report, SAE Technical Paper, 1989.

[12] Athanasios G Konstandopoulos, Evangelos Skaperdas, James Warren, and Ronny Allansson. Optimized filter design and selection criteria for continuously regenerating diesel particulate traps. Technical report, SAE Technical Paper, 1999.

[13] Athanasios G Konstandopoulos, Margaritis Kostoglou, Evangelos Skaperdas, Eleni Papaioannou, Dimitrios Zarvalis, and Evdoxia Kladopoulou. Fundamental studies of diesel particulate filters: transient loading, regeneration and aging. Technical report, SAE Technical Paper, 2000.

[14] Athanasios G Konstandopoulos, Evangelos Skaperdas, and Mansour Masoudi. Inertial contributions to the pressure drop of diesel particulate filters. Technical report, SAE Technical Paper, 2001.

[15] Mansour Masoudi, Athanasios G Konstandopoulos, Michail S Nikitidis, Evangelos Skaperdas, Dimitrios Zarvalis, Evdoxia Kladopoulou, and Christodoulos Altiparmakis. Validation of a model and development of a simulator for predicting the pressure drop of diesel particulate filters. Technical report, SAE Technical Paper, 2001.

[16] E Skaperdas and AG Konstandopoulos. Prediction of diesel particulate filter loading behavior for system control applications. *CD AUTO*, 1(3), 2001.

[17] Grigorios C Koltsakis and Anastasios M Stamatelos. Modes of catalytic regeneration in diesel particulate filters. *Industrial & engineering chemistry research*, 36(10):4155–4165, 1997.

[18] SC Sorenson, Jakob W Høj, and Per Stobbe. Flow characteristics of sic diesel particulate filter materials. Technical report, SAE Technical Paper, 1994.

[19] GA Stratakis, DL Psarianos, and AM Stamatelos. Experimental investigation of the pressure drop in porous ceramic diesel particulate filters. *Proceedings of the Institution of Mechanical Engineers, Part D: Journal of Automobile Engineering*, 216(9):773–784, 2002.

[20] OA Haralampous, IP Kandylas, GC Koltsakis, and ZC Samaras. Diesel particulate filter pressure drop part 1: Modelling and experimental validation. *International Journal of Engine Research*, 5(2):149–162, 2004.

[21] Nicholas P Ramskill, Andrew PE York, Andrew J Sederman, and Lynn F Gladden. Magnetic resonance velocity imaging of gas flow in a diesel particulate filter. *Chemical Engineering Science*, 158:490–499, 2017.

[22] F Payri, A Broatch, JR Serrano, and P Piqueras. Experimental–theoretical methodology for determination of inertial pressure drop distribution and pore structure properties in wall-flow diesel particulate filters (dpfs). *Energy*, 36(12):6731–6744, 2011.

[23] F Payri, A Broatch, JR Serrano, and P Piqueras. Experimental–theoretical methodology for determination of inertial pressure drop distribution and pore structure properties in wall-flow diesel particulate filters (dpfs). *Energy*, 36(12):6731–6744, 2011.

[24] OA Haralampous, IP Kandylas, GC Koltsakis, and ZC Samaras. Diesel particulate filter pressure drop part 1: Modelling and experimental validation. *International Journal of Engine Research*, 5(2):149–162, 2004.

[25] SF Benjamin and CA Roberts. Methodology for modelling a combined dpf and scr catalyst with the porous medium approach in cfd. *SAE International Journal of Engines*, 7(2014-01-2819):1997–2011, 2014.

[26] SF Benjamin, Z Liu, and CA Roberts. Automotive catalyst design for uniform conversion efficiency. *Applied Mathematical Modelling*, 28(6):559–572, 2004.

[27] Michiel T Kreutzer, Freek Kapteijn, Jacob A Moulijn, and Johan J Heiszwolf. Multiphase monolith reactors: chemical reaction engineering of segmented flow in microchannels. *Chemical Engineering Science*, 60(22):5895–5916, 2005.

[28] Todd Jacobs, Sougato Chatterjee, Ray Conway, Andy Walker, Jan Kramer, and Klaus Mueller-Haas. Development of partial filter technology for hdd retrofit. Technical report, SAE Technical Paper, 2006.

[29] O Salvat, Patrice Marez, and Gérard Belot. Passenger car serial application of a particulate filter system on a common rail direct injection diesel engine. Technical report, SAE Technical Paper, 2000.

[30] Walter Knecht. Diesel engine development in view of reduced emission standards. *Energy*, 33(2):264–271, 2008.

[31] AJ Torregrosa, A Broatch, R Novella, and LF Mónico. Suitability analysis of advanced diesel combustion concepts for emissions and noise control. *Energy*, 36(2):825–838, 2011.

[32] A Sarvi and R Zevenhoven. Large-scale diesel engine emission control parameters. *Energy*, 35(2):1139–1145, 2010.

[33] Vicente Bermúdez, José M Lujan, Benjamín Pla, and Waldemar G Linares. Effects of low pressure exhaust gas recirculation on regulated and unregulated gaseous emissions during nedc in a light-duty diesel engine. *Energy*, 36(9):5655–5665, 2011.

[34] Efthimios Zervas, Stavros Poulopoulos, and Constantinos Philippopoulos. Co 2 emissions change from the introduction of diesel passenger cars: case of greece. *Energy*, 31(14):2915–2925, 2006.

[35] AG Konstandopoulos. Update on simulation of diesel particulate emission control systems. In *Ulysses–modelling and simulation workshop. The future propulsion as One System*, 2009.

[36] Edward J Bissett. Mathematical model of the thermal regeneration of a wall-flow monolith diesel particulate filter. *Chemical Engineering Science*, 39(7-8):1233–1244, 1984.

[37] Herman Weltens, Harald Bressler, Frank Terres, Hubert Neumaier, and Detlev Rammoser. Optimisation of catalytic converter gas flow distribution by cfd prediction. Technical report, SAE Technical Paper, 1993.

[38] N Zuckerman and N Lior. Jet impingement heat transfer: physics, correlations, and numerical modeling. *Advances in heat transfer*, 39:565–631, 2006.

[39] JMM Barata, DFG Durao, and MV Heitor. Velocity characteristics of multiple impinging jets through a crossflow. *Journal of fluids engineering*, 114(2):231–239, 1992.

[40] A Melling and JH Whitelaw. Turbulent flow in a rectangular duct. *Journal of Fluid Mechanics*, 78(02):289–315, 1976.

[41] Shabeer Ahmed and E Brundrett. Turbulent flow in non-circular ducts. part 1: Mean flow properties in the developing region of a square duct. *International Journal of Heat and Mass Transfer*, 14(3):365–375, 1971.

[42] S Gavrilakis. Numerical simulation of low-reynolds-number turbulent flow through a straight square duct. *Journal of Fluid Mechanics*, 244:101–129, 1992.

[43] JL Lage, BV Antohe, and DA Nield. Two types of nonlinear pressure-drop versus flow-rate relation observed for saturated porous media. *Journal of Fluids engineering*, 119(3):700–706, 1997.

[44] K Boomsma and D Poulikakos. The effects of compression and pore size variations on the liquid flow characteristics in metal foams. *Journal of fluids engineering*, 124(1):263–272, 2002.

[45] JS Andrade Jr, UMS Costa, MP Almeida, HA Makse, and HE Stanley. Inertial effects on fluid flow through disordered porous media. *Physical Review Letters*, 82(26):5249, 1999.

[46] Mamoun Medraj, Eric Baril, Virendra Loya, and Louis-Philippe Lefebvre. The effect of microstructure on the permeability of metallic foams. *Journal of materials science*, 42(12):4372–4383, 2007.

[47] Sabri Ergun. Fluid flow through packed columns. *Chem. Eng. Prog.*, 48:89–94, 1952.

[48] IF Macdonald, MS El-Sayed, K Mow, and FAL Dullien. Flow through porous media-the ergun equation revisited. *Industrial & Engineering Chemistry Fundamentals*, 18(3):199–208, 1979.

[49] Gordon S Beavers and Ephraim M Sparrow. Non-darcy flow through fibrous porous media. *Journal of Applied Mechanics*, 36(4):711–714, 1969.

[50] GS Beavers, EM Sparrow, and DE Rodenz. Influence of bed size on the flow characteristics and porosity of randomly packed beds of spheres. *Journal of Applied Mechanics*, 40(3):655–660, 1973.

[51] BV Antohe, JL Lage, DC Price, and RM Weber. Experimental determination of permeability and inertia coefficients of mechanically compressed aluminum porous matrices. *Journal of fluids engineering*, 119(2):404–412, 1997.

[52] Nihad Dukhan and Carel A Minjeur II. A two-permeability approach for assessing flow properties in metal foam. *Journal of Porous Materials*, 18(4):417–424, 2011.

[53] Nihad Dukhan and Krunal P Patel. Entrance and exit effects for fluid flow in metal foam. In *POROUS MEDIA AND ITS APPLICATIONS IN SCIENCE, ENGINEERING, AND INDUSTRY: 3rd International Conference*, volume 1254, pages 299–304. AIP Publishing, 2010.

[54] Nihad Dukhan and Krunal Patel. Effect of sampleâĂŹs length on flow properties of open-cell metal foam and pressure-drop correlations. *Journal of Porous Materials*, 18(6):655–665, 2011.

[55] Nihad Dukhan and Mohamed Ali. Effect of confining wall on properties of gas flow through metal foam: an experimental study. *Transport in porous media*, 91(1):225–237, 2012.

[56] Nahid Dukhan. Correlations for the pressure drop for flow through metal foam. *Experiments in fluids*, 41(4):665–672, 2006.

[57] J Prieur Du Plessis. Analytical quantification of coefficients in the ergun equation for fluid friction in a packed bed. *Transport in porous media*, 16(2):189–207, 1994.

[58] Guido Belforte, Terenziano Raparelli, V Viktorov, and A Trivella. Metal woven wire cloth feeding system for gas bearings. *Tribology International*, 42(4):600–608, 2009.

[59] Nihad Dukhan, Özer Bağcı, and Mustafa Özdemir. Experimental flow in various porous media and reconciliation of forchheimer and ergun relations. *Experimental Thermal and Fluid Science*, 57:425–433, 2014.

[60] Tongbeum Kim and Tian Jian Lu. Pressure drop through anisotropic porous mediumlike cylinder bundles in turbulent flow regime. *Journal of Fluids Engineering*, 130(10):104501, 2008.

[61] Li wen Jin and Kai Choong Leong. Pressure drop and friction factor of steady and oscillating flows in open-cell porous media. *Transport in Porous Media*, 72(1):37–52, 2008.

[62] Simone Mancin, Claudio Zilio, Alberto Cavallini, and Luisa Rossetto. Pressure drop during air flow in aluminum foams. *International Journal of Heat and Mass Transfer*, 53(15):3121–3130, 2010.

[63] Wei Zhong, Xin Li, Guoliang Tao, and Toshiharu Kagawa. Measurement and determination of friction characteristic of air flow through porous media. *Metals*, 5(1):336–349, 2015.

[64] John R. Taylon. *An introduction to error analysis: the study of uncertainties in physical measurments, 2d Edition*.

[65] Herrmann Schlichting and Klaus Gersten. *Boundary-layer theory*. Springer Science & Business Media, 2003.

[66] C. F. Colebrook. Turbulent flow in pipes, with particular reference to the transition between the smooth and rough pipe laws. *J. Inst. Civ. Eng. Lond*, 11:133–156, 1938–1939.

[67] S. E. Haaland. Simple and explicit formulas for the friction factor in turbulent pipe flow. *J. Fluids Eng.*, pages 89–90, 1983.

[68] Francis AL Dullien. *Porous media: fluid transport and pore structure*. Academic press, 2012.